UNIVERSITY OF SOUTHAMPTON
FACULTY OF ENGINEERING, SCIENCE & MATHEMATICS
Optoelectronics Research Center

Investigation into Mid-Infrared Pulse Shaping Using an Optical Parametric Oscillator

by
Naveed A Naz

Thesis for the degree of Doctor of Philosophy

26th March 2008

26th March 2008

Declaration of Authorship

I, Naveed A Naz, declare that this thesis titled, 'Investigation into Mid-Infrared Pulse Shaping Using an Optical Parametric Oscillator' and the work presented in it are my own. I confirm that:

- This work was done wholly or mainly while in candidature for a research degree at this University
- Where any part of this thesis has previously been submitted for a degree or any other qualification at this University or any other institution, this has been clearly stated
- Where I have consulted the published work of others, this is always clearly attributed
- Where I have quoted from the work of others, the source is always given. With the exception of such quotations, this thesis is entirely my own work
- I have acknowledged all main sources of help
- Where the thesis is based on work done by myself jointly with others, I have made clear exactly what was done by others and what I have contributed myself

Signed: _____

Date: _____

"It is only after we have lost everything, that we are free to do anything."

$\sim$ Tyler Durden, Fight Club

UNIVERSITY OF SOUTHAMPTON

Abstract

Optoelectronics Research Center
Faculty of Engineering, Science & Mathematics

Doctor of Philosophy

by Naveed A Naz

This thesis reports experimental indirect spectral transfer of shaped pulses from the near to mid-infrared via the use of an optical parametric oscillator. It was shown that good spectral fidelity of transfer can be achieved by making suitable adjustments to the OPO. The issues affecting the transfer process are discussed and experimental results are compared with existing theory. The shaping of the near-infrared pulses was performed using a zero dispersion pulse shaper and a computer controlled spatial light modulator. A suitable search algorithm was written and, with the use of appropriate computer hardware, allowed a closed-feedback loop to be implemented. The computer controlled hardware was demonstrated to be able to autonomously optimise simple experiments in the mid-infrared and optimise the threshold of an optical parametric oscillator.

Acknowledgements

I have left this section till last. It is not because I have no one to acknowledge, rather I feel there are so many. Throughout my course there have been many people who have helped me both academically and personally. Traditionally academic acknowledgements go before personal, but without both I don't think I would have finished my PhD.

The first person I must thank is my current supervisor, Dave Shepherd. I have heard many scare stories of bad supervisors. But you will never find a bad word said about Professor Dave Shepherd, and I, and everyone, who has ever worked with him will testify to that. Dave's been a constant source of encouragement, and his patience with me has been legendary. Sometimes I think I would have given up on me, any lesser supervisor would have, and who could have blamed them? But Dave didn't. I want to thank you for all the times I've bugged you to read my thesis; I appreciate it more than you imagine.

I'd also like to thank my former supervisor Dave Hanna, whose enthusiasm for photonics got me onto this course. If it weren't for Dave Hanna I would have stayed in London to do a PhD. But that would have been a mistake. I have learnt more about myself moving to Southampton, than in all the years I have lived in the capital, and I was born there. It feels ironic that the time I feel most able to do a PhD is when I've just finished one. But I guess that's part of the learning process. The other person who helped me academically is my former postdoc Martin O'Connor. Martin was a major source of encouragement, and whose enthusiasm alone could make experiments work! I wish someday I can be as enthusiastic and elegantly spoke as Martin, I'm sure that's all a man needs to get far in life.

I'd like to thank all the past and present members of the OPO group. Paul Lloydd, who was there when I started my course and whose terrible jokes broke many a monotonous days. Hazel Hung ("the new student"), for helping me with the autocorrelation work and listening to me whiter on about how to align stuff and lab stuff – sometimes explaining it to someone concentrates my mind. I hope you got something out of the process, because sometimes I feel I might have

confused you more than I helped. And I'd like to thank Jerry Prawiharjo, whose computational simulations made sense of my work.

Of course none of this would be possible without the "glue" which holds the school together; I am of course talking about the technicians and admin staff. I've had interactions with virtually all the technicians, but I'd like to particularly thank Simon Butler, Tim McIntyre, and Chris Nash (who was my former landlord, and the best I have ever known). I have also received much help from the admin staff, and the network administrators, who lent me a laptop while I wrote up my thesis. But I'd like to pay special homage to Eve Smith, the student coordinator for the ORC. If the technicians and admin staff are the glue that holds the department together, than Eve Smith is the blood that keeps the student's alive, she has gone beyond the call of duty to keep the student population running smoothly. Eve is the first person we rush to when something goes wrong, be it university related, housing, thesis projects, travel issues, or anything underneath the sun. She has been both agony aunt and wise sage to me. If I could clone one person for the good humanity, it would be Eve Smith. Eve helped me get settle when I first moved to Southampton and has been checking up on me ever since, it's reassuring to know that someone cares for your well being.

In my personal life I have meet so many people during my time in Southampton. For my first year in Southampton I'm indebted to the friendship of so many people who have made me feel welcomed. I'd especially like to thank Andrew Weld, Michael Roelsen, Anika Vogel, Nick Chaffey, Rowan Wilson, and Martin. Its sad how as time goes on friendships slowly change and before you know it, they fade and move into memory, but new friends are made and the cycle continues. For the last few years at Southampton I spent much of my time with the "Mexicans": the twins Adrian and Rodrigo Amezcua Correa, Simos Ashmakhs (technically Greek, but considered an honouree Mexican), and Andrew Brearley (from Newcastle, but Mexican in nature). I miss our DVD nights, where Andy, Simos, and I would huddle on Simos's bed to watch a move on Simos tiny computer monitor, and smoke a nargileh. I looked forward to DVD night; it was the one day in the week where I could truly relax.

I want to pay special acknowledge to Adrian Amezcua Correa. Adrian motivated me to finish off my thesis. We formed a study group where we would meet up at his house to write up our thesis. But I slacked off, so Adrian took upon the task of motivating me, which consisted of taking a £100 deposit from me, and keeping

£10 for every day that I didn't turn up. I think it was more the embarrassment of loosing money over something as trivial as waking up before 8 am everyday that kept me turning up at his house on time. Adrian's one of the smartest people I know and I'm sure he knew the psychological implementations of his concept. But how many people are willing to go to such extent to help a friend? I consider myself lucky that I have had such good friends. I'll remember your help, dear friend.

Contents

List of Figures

Chapter 1

Introduction

1.1 Thesis Motivation

The field of laser chemistry involves the manipulation of molecules and chemical reactions using temporally shapable laser pulses. As will be discussed later, many interesting organic vibrational modes occur in the mid-infrared, in order to excite these vibrational modes a highly tunable laser source is required. However, a source which is both wavelength tunable and temporally shapable is hard to come by. In this thesis a unique method for producing temporally shaped pulses in the mid-infrared is demonstrated.

The research presented in this thesis was conducted as a member of the OPO group; as a result some of the experimental and theoretical work was conducted jointly with several members of the group, including M.V.O'Connor who provided help with the theoretical calculations for the optical parametric oscillator, H.S.S.Hung who constructed the mid-infrared interferometric autocorrelator, D.C.Hanna and D.P.Shepherd for providing assistance in technical and theoretical matters and J.Prawiharjo for conducting computer simulations which has allowed a better comparison between the experimental work I have performed with theory. Where appropriate, instances where I specifically played a more subsidiary role in the work are acknowledged in the chapters themselves.

1.2 Background

Laser systems have been in existence for over four decades [1]. Much of the work with pulsed lasers has been dedicated to producing higher peak-powers, shorter pulses, and better beam quality. However, there is another aspect of laser light that for the most part has attracted less attention – the spectral profile of the pulse.

The spectral profile of a laser pulse can have a significant importance in many applications. Altering the phase and amplitude of the pulse's spectrum will alter its temporal characteristics. Most laser systems utilise pulses that have a flat phase profile across their spectrum, resulting in the shortest pulse duration for the given spectral bandwidth. These pulses are called Fourier-transform-limited-pulses, or more commonly bandwidth-limited pulses. However, sometimes a bandwidth-limited pulse will not always give the best performance for a given application. Examples of this include propagation through a dispersive bulk medium [2] or long lengths of fibre [3, 4]; optimising the coherent emission of high-harmonic x-rays in a gas-filled capillary waveguide [5]; code division multiplexing of optical signals [6]; controlling the wavefunction of atomic states [7] and "laser chemistry" [8–10].

1.2.1 Laser Chemistry

Laser chemistry has been a dream for over 30 years [9]. In this concept, chemical reactions can be manipulated using laser pulses. As a simple example, let us suppose we would like to break the strong bond in a particular molecule while leaving the weaker bonds intact. Simply heating the molecule will not work. However, if we could use a laser pulse tuned to the absorption frequency of the strong bond then we could achieve our goal.

Since the 1960's attempts at laser chemistry were performed using a multitude of tunable lasers [10, 11]. Unfortunately, this approach, as well as being expensive and cumbersome, was not effective. At first glance it may seem trivial to break a specific bond with a laser; but due to practical considerations this is quite difficult. Even for a single polyatomic molecule excluded from other molecules and external perturbations, the intermolecular dynamics are very complex, and this is before the introduction of a large pulse of light. Broadly speaking the

dynamics can be separated into electronic, vibrational, and rotational degrees of freedom (with overlap between the categories). Felker and Zewail [12] note that the greatest understanding of molecular dynamics is in the form of the electronic states, primarily because it is easy in comparison to the next hurdle: understanding vibrational dynamics, where the understanding is not so complete. Felker and Zewail write: "The relative lack of knowledge of vibrational effects compared to the knowledge of electronic states on intramolecular dynamics is due primarily to the larger number of relevant states (often millions of states per cm^{-1}), less precise knowledge of relevant couplings, and experimental difficulties in measuring vibrational state-specific rates" [12]. Vibrational dynamics have a significant effect on the behaviour of the molecule; they affect the chemical bonds between atoms via intramolecular vibrational-energy redistribution (IVR). This is the process where localised energy in a particular vibrational mode is redistributed into other modes.The use of sub-picosecond pulses can help offset these problems. This is because electronic transitions within a molecule happen almost instantly, while the vibrational relaxation time [of nuclei] is of the order of 10^{-12} seconds [13]. Therefore, sub-picosecond pulses act on a molecule faster than the dephasing time due to IVR. Even allowing for IVR there is a host of other effects that can affect the performance of a mode selective laser system. Such effects include the existence of a multitude of energy pathways from the initial to the desired state, intermolecular dynamics resulting from effects such as photon exchange between molecules, molecular collisions, perturbations in the energy configuration and statistical noise constantly changing energy pathways. Due to these effects (and many more) an analytical solution can not be determined and a numerical approach via a control loop is often needed to search for the best solution [14].

1.2.2 Optical Parametric Oscillators

Laser chemistry can be performed with different wavelengths of light, from ultraviolet [15] to the far infrared [16]. For organic molecules a particularly interesting range for experimentation is in the 2 to 10 μm region, since within this region there are numerous vibrational absorption maxima [17]. Figure 1.1 shows common organic molecular bonds and the absorption regions of typical vibrational modes. The vibrational modes depicted in the figure are due to a number of different effects these include stretching of the bond, changes in the angle between

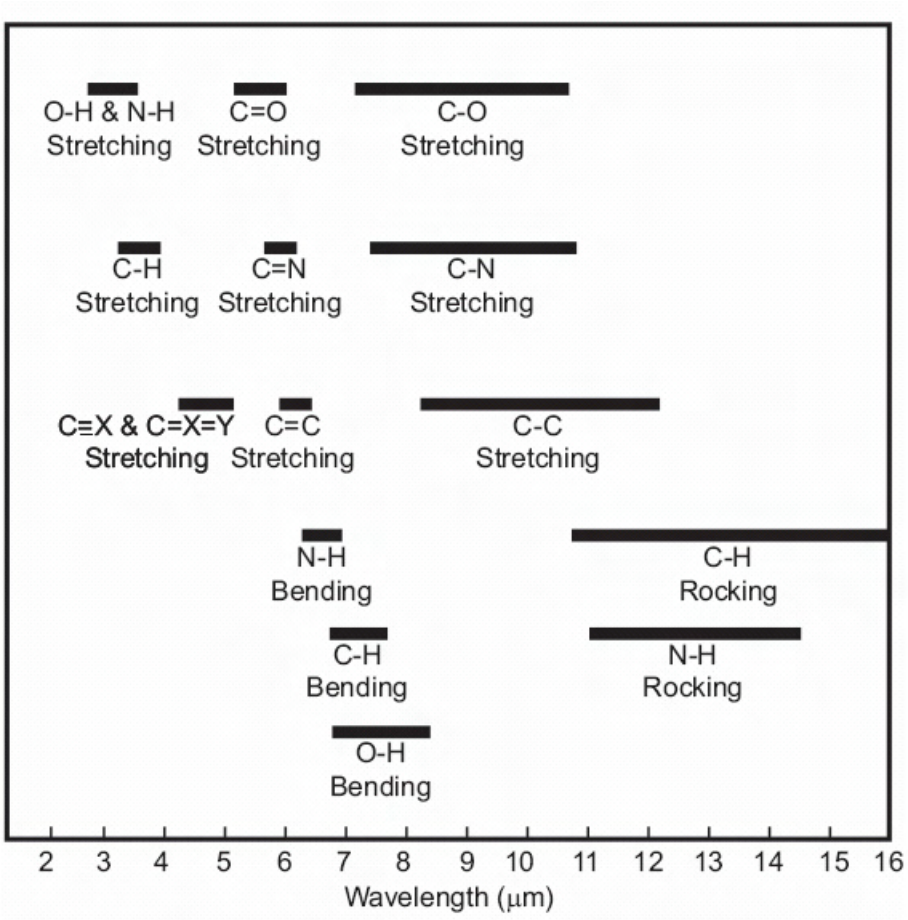

FIGURE 1.1: Diagram showing common organic bonds and typical regions of absorption for various vibrational modes. Retrieved from [18] on 29-Sept-2007

two bonds, called bending, and a change in the angle between groups of atoms, which is called rocking.

It is clear that in order to excite different vibrational modes and avoid the effects of IVR a widely tunable, femtosecond laser is required. The generation of femtosecond pulses inherently requires a large spectral bandwidth. As an example, in order to generate a 100 femtosecond pulse with a Gaussian temporal profile, approximately $4 \times 10^{12}\,Hz$ of spectral bandwidth is required. In terms of spectral wavelength, this corresponds to a bandwidth of $15\,nm$ for an optical pulse centred around $1\,\mu m$. The generation of short pulses and wide spectral tunability in the mid-infrared can readily be achieved with an optical parametric oscillator (OPO).

The first optical parametric oscillator was demonstrated in 1965 [19]. An optical parametric oscillator consists of a nonlinear crystal within a resonator. A pump photon entering the nonlinear crystal is split into two longer wavelength photons;

these photons are called the signal and idler photon, with the signal having a shorter wavelength than the idler. We shall discuss the physics of the nonlinear process in Chapter 2. For now, it is sufficient to note that the process discussed must obey the traditional physical principles of energy and momentum conservation. With energy conservation dictating the total energy of the two new photons be the same as the incoming pump photon.

The cavity surrounding the nonlinear crystal can be designed to reflect any combination of the three beams. The two most common beam combinations are ones in which the OPO only resonates one beam (usually the signal) and is called a singularly resonant oscillator (SRO); and a cavity that is designed to reflect the signal and idler beams, called a doubly resonant oscillator (DRO). The threshold power required to reach oscillation decreases by many orders of magnitude with the increased number of resonating beams [20]. For a continuous wave OPO with a 1% roundtrip loss for both waves the threshold required to reach oscillation is some 200 times lower for a DRO, compared to an SRO [21]. It is because of the low threshold that DRO were prevalent in the early days of laser physics.

However, despite their low threshold, DROs have the disadvantage of suffering from amplitude and spectral instability, which is caused by a single resonator cavity having to simultaneously satisfy the resonating conditions of beams of different wavelengths, while simultaneously satisfying conservation of energy and momentum in the parametric process as discussed later. Singularly resonant oscillators do not suffer from these problems since they only resonate one beam, but their high threshold value was historically an obstacle for wide spread acceptance. It was advances in pulsed laser sources that allowed lower average powered lasers to be used to pump SRO OPO.

Pulsed lasers have the advantage of producing high peak powers, compared to continuous wave lasers operating with the same average powers. Since the nonlinear process is dependent on peak power for conversion efficiency, a pulsed laser allows for a very convenient pumping source. Another advantage of high peak power pulses is that the low average power reduces the possibility of optical damage to the crystal caused by linear light absorption.

The pulse duration of the laser source has a large effect on the type of resonator cavity used for the OPO. For picosecond and sub-picosecond pulses, synchronous pumping of the OPO is normally required [22]. Synchronous pumping involves

choosing a cavity length such that the round trip time of the resonating signal corresponds to the repetition rate of the pump laser source. In this way, the incoming pump pulses are in synchronism with the resonating signal pulse and both pulses enter the nonlinear crystal at the same time.

Achievements in crystal fabrication have also helped in the development of synchronously pumped OPOs (SPOPOs). As discussed in chapter two, non-linear processes require phasematching for efficient frequency conversion. In the early days, OPOs relied on birefringent crystals to perform this. However, not all highly non-linear materials possess birefringence (or have very little, or sometimes far too much). Byer writes that: "One study discovered that of 22,000 crystals surveyed, fewer than 100 had adequate birefringence for phasematching. Of these, only a handful could be grown and prepared for characterisation of their nonlinear optical properties" [21].

Fortunately in 1962 Armstrong et. al. [23] devised a theoretical technique to overcome this limitation. Their approach is now referred to as quasi-phasematching (QPM) [21]. QPM can allow nonlinear materials that do not possess sufficient birefringence to be used as OPO crystals. The technique of QPM relies on periodically reversing the crystal orientation along the length of the material. This results in a periodic change in the sign of the nonlinear coefficient, which is used to achieve the required phasematching, as discussed in chapter 2. The earliest method of achieving quasi-phasematching was by stacking orientated plates [24]. During the following decades several new methods were devised for achieving QPM, some of these include: chemical indiffusion [25], modulation of the crystals growth process [26], electron beam writing [27] and electric field poling [28]. Each method had its advantages as well as disadvantages. The crystals used in this research were quasi-phasematched using the electric-field method. Electric-field poling involves applying a large external electric field periodically along the length of a ferroelectic material. The electric field has to be strong enough to allow for domain inversion of the nonlinear material, and for a material such as lithium niobate this is usually in the many kilovolts per millimeter range.

The technique of electric field poling revived interest in frequency conversion, especially in lithium niobate ($LiNbO_3$). Even before the introduction of poling, $LiNbO_3$ had been a favourite for practitioners of OPO devices. This was in part because it met all the requirements for a good nonlinear crystal; it possessed birefringence, a high damage threshold, wide optical transparency, and high nonlinear

coefficients. However, the introduction of poling would lead to a 20 fold increase in the usable nonlinearity of $LiNbO_3$ and interest in the material soared. Periodically poled lithium niobate (PPLN) was the material used for frequency conversion in this research.

1.2.3 Pulse Shaping

At the same time as progress was being made in nonlinear materials interest was developing in the area of pulse shaping. Pulse shaping involves changing the temporal profile of a pulse. Laser pulse shaping is almost as old as the field of laser physics itself. Much of the early interest in pulsed laser physics centred on achieving systems of higher peak power with short pulse widths and good stability. In 1968 Treacy [29] discovered that the pulses from his Nd:glass laser were chirped. This meant that not all the spectral components of the pulse were in phase, rather there was a delay between them. From theory the full width at half maximum (FWHM) temporal duration of the pulse Δt multiplied by the FWHM of the spectral intensity $\Delta\nu$ of the pulse, gives a value called the time-bandwidth product. The minimum value of this product is dependent on the shape of the frequency spectrum. As an example, for a pulse with a Gaussian spectrum the minimum time-bandwidth product is 0.44. A pulse that has a minimum time-bandwidth product is said to be bandwidth-limited, or transform-limited [30]. Treacy found the pulses from his laser were not bandwidth-limited, but by using a pair of diffraction gratings he was able to achieve the minimum pulse duration allowed by the time-bandwidth product. The theoretical study was published the following year [31]. The discovery was important, as it became clear that in order to achieve the minimum pulse duration (bandwidth-limited) the spectral phase of the pulse must be considered. This started the interest in temporal pulse shaping.

Early work in pulse shaping concentrated on simple pulse compression but later interest in arbitrary pulse shaping started to grow. Some of the early work involved directly shaping the pulse in time using a Pockel's cell [32]. However sub-picosecond pulses (ultrashort pulses) are too fast for direct modulation. The fastest electro-optical devices, such as Pockel's cells [33] and electro-optic Kerr cells [34] operate in the tens of picoseconds regime. Achieving direct modulation below this time-scale is problematic.

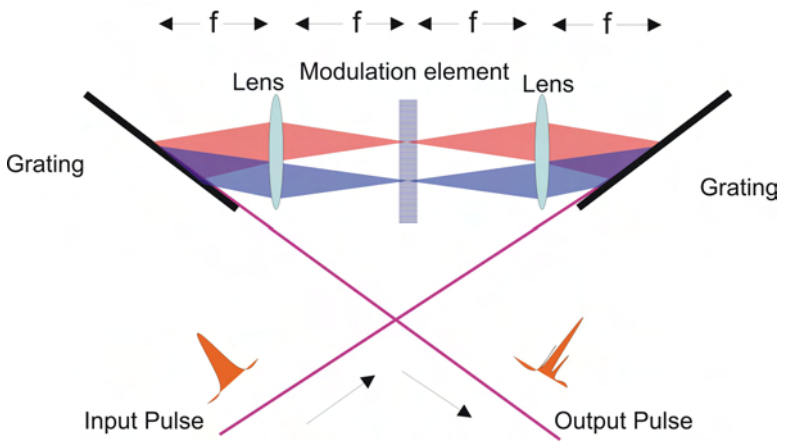

FIGURE 1.2: Experimental setup of a zero-dispersion pulse shaper. The left side of the modulation element is mirror image of the right, that is to say the focal length of the lenses are the same, as are the dispersion characteristics of the gratings and the separation of the optical elements is identical.

To overcome this problem it was necessary to abandon attempts at direct time modulation, and instead concentrate on indirect manipulation. There are various methods to achieve this. In 1983 Froehley et. al. [35] wrote a review of the subject. In their paper, they describe various methods to achieve indirect time modulation. Some of the methods include two-pulse interference [35], transmission through time independent optical pupils [35], time independent response of Young's slits [35], and time impulse response of a periodic grating [35]. The most successful class of methods involved Fourier-based pulse-shaping techniques, which relied on shaping the spectrum in some form and hence allowing control over the temporal pulse shape.

The most common setup for a Fourier based technique was described by Froehley et. al. in their review article. It is still the setup of choice for most experiments and saw huge interest in the late 1980's when it was popularised by Weiner et. al. for femtosecond pulse shaping [36–41]. It has the aesthetic advantage of directly shaping the phase/amplitude of the spectrum. Other techniques in comparison relied on shaping a complicated and often abstract function; making it difficult to intuitively determine the effect on an incoming pulse. The basic setup of Froehley's pulse shaper is shown in Figure 1.2. The spectrum of the incoming beam is first angularly dispersed by the diffraction grating according to its wavelength. A lens is placed one focal length away from the first grating, and in the back focal plane of this lens the far field image of the diffracted wavelengths can be observed. This focal plane is often called the Fourier plane and it is here that the spectrum of

the pulse can be seen. At this location, a device for modulating the phase and/or amplitude of the pulse is placed. The other half of the setup is a mirror image of the first half and is responsible for spatially recombining the pulse. There is no universally recognised name for this experimental layout; it is sometimes referred to as a "zero-dispersion delay line", "zero-dispersion stretcher", or "zero-dispersion pulse shaper". For the duration of this thesis we shall simply refer to it as the "pulse shaper" or "shaper". The setup is familiar to users of chirped pulse amplifiers as it is sometimes used to compress a pulse after is has been amplified. This is achieved by changing the length of the shaper so that it is no longer zero dispersive [42].

A variety of optics can be used to manipulate the spectrum at the Fourier plane. In early experiments these consisted of thin optical plates (masks), which either had an amplitude pattern shaded upon them, or a pattern that varied the optical path length of light, therefore allowing phase modulation. The technique was flexible, but it meant that each time the user required a different pulse a new mask had to be fabricated. This led to interest in computer programmable optical modulators. These devices allowed immense flexibility as different masking patterns could be generated on demand. The first occurrence of this was in 1988 using a liquid crystal spatial light modulator (LC SLM) [43, 44]. LC SLMs are still a popular choice for temporal pulse shaping and is the technology used in this research (the operation of the LC SLM is described in subsequent chapters).

However, LC SLMs are by no means the only type of modulators available. Six years after Weiner et. al. demonstrated their feasibility, Hillegas et. al. showed the successful use of a acousto-optic modulator (AOM) for pulse shaping [45]. For the purposes of pulse shaping AOMs can be used in place of a LC SLM within a 4f setup, with the minor modification of placing the AOM at the Bragg angle to the incoming light (see Figure 1.3). The AOM used within a pulse shaper is better described as a deflector, than a modulator, this will be become apparent shortly. AOMs work on a different principle to LC SLM, but can achieve the same phase and amplitude modulation effect. In a AOM, acoustic waves are generated across a crystal using a transducer. These sound waves cause density (refractive index) variations along the length of the material, which act like a diffraction grating and they diffract light passing transversely to the crystal.

The AOMs use of travelling sound waves puts a limit on the repetition rate of the laser that can be used with this sort of pulse shaping arrangement. This is because the time between successive laser pulses must be longer than the time

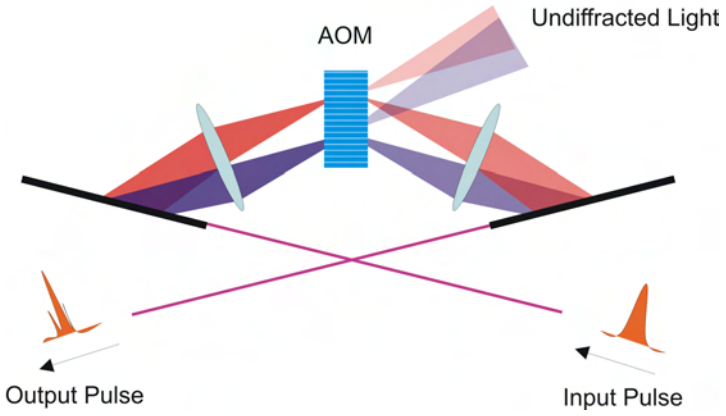

FIGURE 1.3: 4f pulse shaper arrangement with an AOM used as the modulation element

it takes for one refractive index profile (generated by the transducer) to travel along the length of the crystal. If this condition is not met then it is not possible to modulate a train of incoming pulses with the same profile. As an example, a common accousto-optic material such as TeO_2 has sound propagating through it at $4.2\,mm/\mu s$ [45]; therefore, a $12\,mm$ crystal can be operated with a laser with a maximum repetition rate of $390\,kHz$. This is also the maximum refresh rate of the device, which is substantially higher than a LC SLM. Furthermore, unlike the LC SLM, which is a pixelated device, the AOM can apply a continuously varying modulation pattern. However, AOMs have certain disadvantages, which make them unsuitable for certain applications. Firstly, only about 50% of the light passing through the AOM can be diffracted [45], and secondly the device can not operate with high-repetition-rate pulse sources, such as ours.

Advancement in AOM technology has allowed a new device to be fabricated, called an acousto-optic programmable dispersive filter (AOPDF), or Dazzler [46, 47]. This device is able to achieve pulse shaping without the use of a 4f pulse shaper. Figure 1.4 shows a schematic diagram of the device (diagram taken from reference [47]). The Dazzler uses a birefringent accousto-optical crystal to achieve pulse shaping, and the components used in the device are very similar to the more traditional AOM. The device uses a transducer to propagate sound waves through the length of the crystal. However, unlike the traditional AOM where light enters the crystal transversely to the propagating sound waves, the light in the Dazzler is launched collinearly to the sound waves, and with its polarisation aligned to

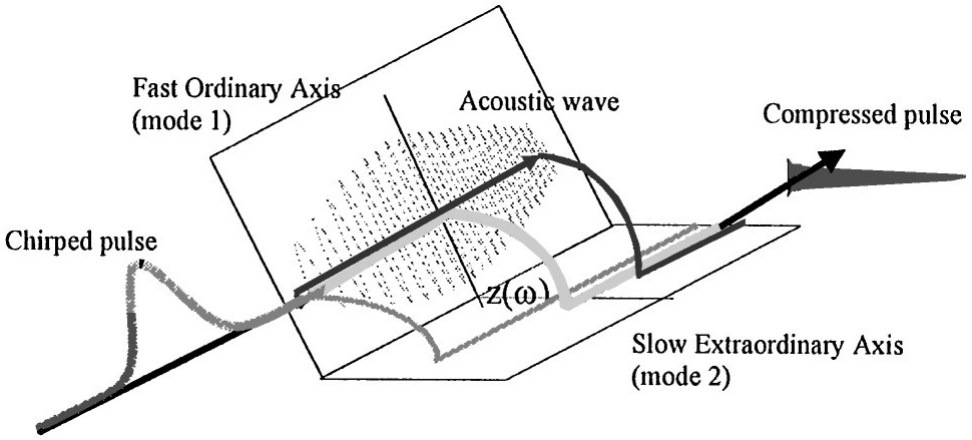

FIGURE 1.4: Schematic diagram showing the operation of the Dazzler

the materials fast optical axis (axis with the lower refractive index). The Dazzler performs phase modulation by altering the distance along the propagation axis where different frequency components of light change polarisation from the fast to slow axis. Light which changes polarisation early on travels through the slow axis for longer, and is retarded more than light that changed polarisation later on. The Dazzler has many advantages over the LC SLM pulse shaper, chiefly the lack of 4f pulse shaping arrangement makes the Dazzler more compact and easier to setup. However the Dazzler, like the traditional AOM can not be used with high repetition rate lasers.

1.2.4 Control Algorithms

The use of programmable devices opened up the area of adaptive computer control, which was an important milestone as it allowed previously unattainable experiments to come into fruition. As hinted at the beginning of this chapter the real world is often far from ideal with many unknown factors. In the past, it was the duty of the experimentalist to try to anticipate these effects and adjust the experiment to account for them, which often led to the process of trial and improvement. However, the use of a computer can help automate this procedure. A computer can monitor the experiment using a suitable parameter, or set of parameters, such as the signal from a photodiode, and based on this it can change the pulses entering the experiment. The computer can be programmed to find a solution to a problem where little is known about the nature of the best solution, and no method for calculating the solution is known before hand. The field of

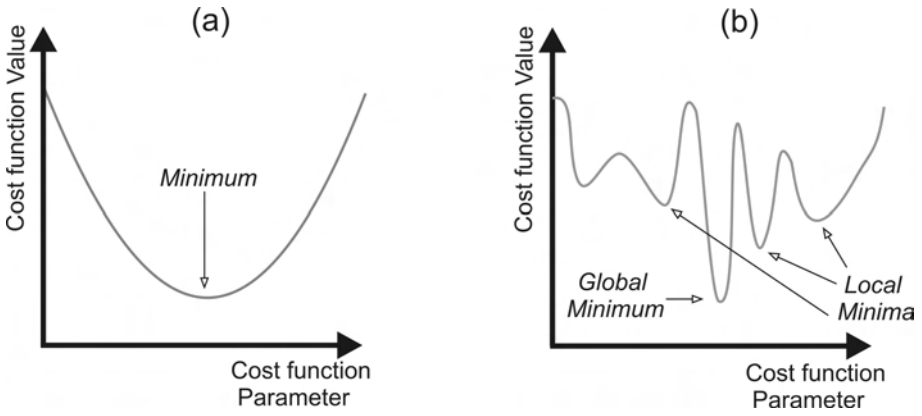

FIGURE 1.5: Schematic diagram showing the difference between a) parabolic search space with only one minimum value, b) search space with more than one minimum, the absolute lowest value is called the global minimum whereas the other minima are called local minima. It is important for any good search algorithm to converge at the global minimum, and not get trapped in any of the local minima.

computational analysis, which deals with difficult problems of this type, is called metaheuristics. Metaheuristics deals with global optimisation routines, as opposed to local optimisation. Before explaining the difference between these two routines, we shall first define some terms that are used in metaheuristics. It is customary to define the region where the algorithm can look for possible solutions as the search space, with a particular point in the search space being referred to as a state. It is also traditional to talk in terms of the search algorithm minimising an objective or cost function, this function represents the problem being solved and gives the algorithm feedback on how well it is doing. The difference between a global and local optimisation routine can be explained by a diagram, which shows a plot of a fictitious search space in one dimension (fig 1.5).

A typical search algorithm usually starts at one, or a set, of random states in the search space and will try to find the lowest value in as few computer cycles as possible. A local search algorithm is ideal if we are looking for a solution in a smooth parabolic search space, fig 1.5(a). In some situations this will not be true, e.g. see fig 1.5(b) where there are many minima the algorithm could converge to. These sorts of problems are dealt with using global optimisation routines. A good routine is able to find the global minimum, and not be trapped in the local minima.

Local optimisation routines have been in existence before the invention of the

computer. Some of this work can be traced back to the sixteenth century [48], such as Sir Isaac Newton's iterative method for solving polynomials [49]. This particular method was adapted for computer automation and is now known as the Newton-Raphson method. In comparison, global optimisation can often not be performed without the use of powerful computers. The field of metaheuristics is advancing rapidly since global optimisation was first investigated with many methods now available. Two of the most popular methods that we investigate here are Genetic/Evolutionary Algorithms and Simulated Annealing.

Evolutionary algorithms have an interesting history with many simultaneous schools of thought. The first evolutionary algorithm dates back to the 1950's, but the topic was popularised in the 1970's by John Holland [50] with the introduction of his particular procedure called genetic algorithms (GA). Genetic algorithms (like all evolutionary algorithms) get their inspiration from the process of natural selection. The basic procedure for a GA is to start with a random population of states (called genomes in the language of GAs). The cost function (often called fitness by GA practitioners) of each member in the population is evaluated. The genomes are stochastically selected from the population to undergo mutation into new genomes and/or crossover between multiple genomes occurs to produce new states (the biological equivalent of "mating"). The new population of states (called a generation) is evaluated for fitness and based on this some genomes are replaced. The process repeats itself until either the maximum number of generations is reached or a sufficiently good level of fitness is obtained.

The mutation, crossover, genome representation, and fitness function are traditional defined by the end user and called by the algorithm. Great care must be taken in choosing these functions as the convergence efficiency depends heavily upon them. They should be chosen in such a way as to reduce the search space, while simultaneously adjusting the search space to simplify it and give the algorithm useful feedback. Furthermore, there are often many parameters internal to the GAs code that the end user can adjust to improve performance. Some of these include the selection methods for choosing a genome from the population; whether the "children" from a crossover should automatically replace their parents (this scheme is called a simple GA). The alternative is called the steady state GA in which the children can replace the worst/best/random/most-similar member in the population based on either fitness or a stochastic probability. Finally, the user

can change how the genomes rank for fitness. It is important to choose the parameters such that the GA does not become stuck in a local minimum. This is often caused when there is not enough genetic variation within the population. It is also the reason why, in the interest of variation, the algorithm might be engineered to take the counter-intuitive step of periodically replacing the best genomes with ones of a lesser fitness. This process may seem drastic and it may appear to do more harm than good. But this is not necessarily the case, it can be noted that for a sufficiently large population there will always be some genomes similar to the replaced genomes. Therefore, these close-to-best genomes will preserve much of the "genetic information" of the replaced genomes.

The other class of search algorithm that has been investigated is called simulated annealing (SA). Once again it gets its inspiration from naturally occurring phenomena, in this case cooling of hot metal liquids into solids.

It has been observed that when a hot liquid (such as molten iron) slowly cools into a solid, the result is a solid crystalline mass in which the atomic bonds are often in their lowest energy configuration. The key to this process is that the atoms first start with a very high temperature. This allows them a great deal of mobility, the structure is very fluid and the atoms can move in and out of a multitude of different configurations. It is important that the temperature is reduced very slowly (annealing) or cooled in small steps. At each temperature step the atoms should be allowed to reach equilibrium. The reduced temperature reduces their mobility, and the atoms tend to reach the lowest energy configuration; for a metal this is often a crystalline state showing long term ordering of the atoms. If the atoms are cooled quickly (quenching) the resultant structure is usually amorphous or polycrystalline and therefore not in its lowest atomic configuration.

Simulated annealing tries to mimic the above process. It was first introduced by Kirkpatrick et. al. [51] in 1983, using work pioneered by Metropolis et. al. in the 1950's [52]. Like genetic algorithms, it remains a popular choice for solving complex problems. It is easy to program and has the added advantage of a large volume of mathematical proofs which guarantee a SA algorithm to converge given certain constraints [53].

1.3 Research Aim and Overview: An Intelligent Mid-Infrared Pulse Generator

The overall goal of this research is to experimentally investigate the development of a highly versatile computer-controlled instrument for the generation of femtosecond mid-infrared temporally-shaped pulses. It is hoped that this research will lay the foundations for constructing a device with possible applications in coherent control and mid-infrared research.

This thesis shows experimental results that demonstrate to the best of our knowledge the world's first instance of adaptive control of mid-infrared pulses using an optical parametric oscillator [54]. Furthermore, experimental results show high spectral fidelity of pulse transfer from the near- to mid-infrared via an optical parametric oscillator. Again, this is believed to be the first known instance of this type of procedure being applied to an optical parametric oscillator.

Figure 1.6 shows a diagram of the basic setup used throughout the research. The setup consists of three main sections, the pump source, the pulse shaper, and the optical parametric oscillator. The main pump laser consists of a Nd:YLF source in a master oscillator power amplifier (MOPA) configuration. In order to achieve a large spectrum the pulses from this laser are broadened via self-phase modulation using an optical fibre. The pulses out of the fibre are temporally modified using a zero dispersion pulse shaper, these pulses are used to pump an optical parametric oscillator. The pulse shaper is computer controlled, and with the use of suitable search algorithm the pulse shaper is able to optimise the OPO, or an experiment in the mid-infrared.

1.4 Thesis overview

The thesis discusses existing theory used to describe the shaping of pulses using a 4f pulse shaper [55, 56], and the transfer of pulses from the near to mid-infrared [57, 58]. The thesis also corrobates experimental results with theoretical literature [58].

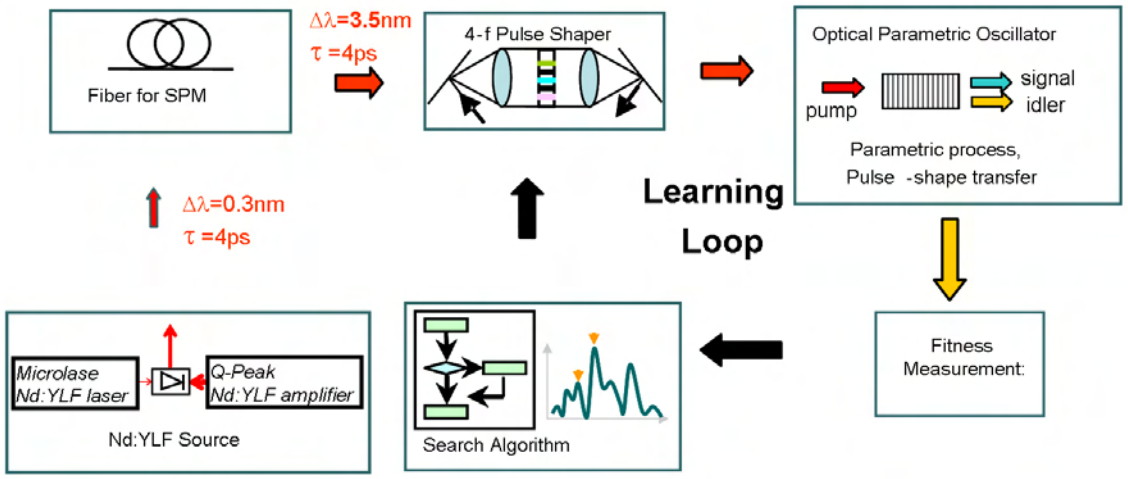

FIGURE 1.6: Schematic diagram showing the basic components used in the majority of experiments. Pulses are first formed using a Nd:YLF laser system, these are then spectrally broadened using a short length of fiber. The pulse is then temporally shaped where it subsequently enters an optical parametric oscillator (OPO). The output from the OPO enters an experiment, the experiment is observed using sensors that relay information to a computer. The computer is equipped with a search algorithm and based on the sensor readings it can alter the temporal shape of the pulse entering the OPO by controlling the pulse shaping setup.

Chapter 2 concentrates on the theoretical understanding of the OPO and existing theories regarding transfer of pulses from the near to mid-infrared via difference frequency generation.

Chapter 3 discusses the pulse-shaping apparatus. This includes design considerations and the effects of the pulse shaper on an incoming pulse. The pulse-shaper can use a number of devices in order to perform the modulation of the pulse's spectrum. We have chosen to use a liquid-crystal spatial-light-modulator. The advantages and operation of this device are discussed in this chapter. Finally, general considerations regarding the search algorithm are mentioned.

Chapter 4 contains details of the various parts of the experimental apparatus. This section contains experimental results that demonstrate the operation of these parts. The chapter is divided into sections, with each section describing and evaluating different parts of the overall setup. The sections include: the laser source used throughout the research; diagnostic instruments in the mid-infrared, such as the monochromator and a home-built mid-infrared interferometric autocorrelator;

experimental setup and performance of the OPO; the spatial light modulator and its use with the computer algorithm; the experimental setup of the pulse-shaper and preliminary results; and finally details of the search algorithms used.

Chapter 5 discusses experiments that demonstrate adaptive control of the OPO. This chapter demonstrates the ability to optimise experiments in the mid-infrared, and experiments to minimise the threshold of the OPO by allowing the search algorithm to alter the temporal pulse shapes entering the OPO.

Chapter 6 demonstrates high fidelity of spectral transfer from the near to mid-infrared and investigates the factors which effect the transfer process.

Finally, chapter 7 presents a summary of significant results from the preceding chapters, together with potential future directions. The thesis closes with a list of publications arising from this work, including full-text articles where appropriate.

1.5 References

[1] T. H. Maiman, "Stimulated Optical Radiation in Ruby," Nature **187**(4736), 493–494 (1960).

[2] J. C. Delagnes, A. Monmayrant, P. Zahariev, A. Arbouet, B. Chatel, B. Girard, and M. A. Bouchene, "Compensation of resonant atomic dispersion using a pulse shaper," Applied Physics B-Lasers and Optics **86**(4), 573–578 (2007).

[3] F. G. Omenetto, J. W. Nicholson, B. P. Luce, D. Yarotski, and A. J. Taylor, "Shaping, propagation and characterization of ultrafast pulses in optical fibers," Appl. Phys. B **70**, S143–S148 (2000).

[4] S. H. Lee, A. L. Cavalieri, D. M. Fritz, M. Myaing, and D. A. Reis, "Adaptive dispersion compensation for remote fiber delivery of near-infrared femtosecond pulses," Optics Letters **29**(22), 2602–2604 (2004).

[5] R. Bartels, S. Backus, E. Zeek, L. Misoguti, G. Vdovin, I. P. Christov, M. M. Murnane, and H. C. Kapteyn, "Shaped-pulse optimization of coherent emission of high-harmonic soft X-rays," Nature **406**(6792), 164–166 (2000).

[6] C. C. Chang, H. P. Sardesai, and A. M. Weiner, "Code-division multiple-access encoding and decoding of femtosecond optical pulses over a 2.5-km fiber link," IEEE Photonics Technology Letters **10**(1), 171–173 (1998).

[7] T. C. Weinacht, J. Ahn, and P. H. Bucksbaum, "Controlling the shape of a quantum wavefunction," Nature **397**(6716), 233–235 (1999).

[8] T. Baumert, J. Helbing, G. Gerber, L. Woste, A. H. Zewail, J. Troe, J. Manz, T. Kobayashi, V. S. Letokhov, U. Even, M. Chergui, D. M. Neumark, and S. A. Rice, "Coherent control with femtosecond laser pulses," Chemical Reactions and Their Control on the Femtosecond Time Scale Xxth Solvay Conference on Chemistry **101**, 47–82 (1997).

[9] W. S. Warren, H. Rabitz, and M. Dahleh, "Coherent Control of Quantum Dynamics - the Dream Is Alive," Science **259**(5101), 1581–1589 (1993).

[10] R. N. Zare, "Laser control of chemical reactions," Science **279**(5358), 1875–1879 (1998).

[11] P. M. Felker and A. H. Zewail, "Photo-Dissociation of Partially Solvated Molecules in Beams by the Picosecond-Jet Technique - Hydrogen-Bond Breakage," Journal of Chemical Physics **78**(8), 5266–5268 (1983).

[12] P. M. Felker and A. H. Zewail, "Picosecond Time-Resolved Dynamics of Vibrational-Energy Redistribution and Coherence in Beam-Isolated Molecules," Adv. Chem. Phys. **70**, 265–364 (1988).

[13] A. H. Zewail, "Laser Selective Chemistry - Is It Possible," Physics Today **33**(11), 27–33 (1980).

[14] R. S. Judson and H. Rabitz, "Teaching Lasers to Control Molecules," Physical Review Letters **68**(10), 1500–1503 (1992).

[15] D. Ascenzi, P. M. Regan, and A. J. Orr-Ewing, "The ultraviolet photodissociation of DCl: H/D isotope effects on the Cl(2P) atom spin-orbit branching," Chemical Physics Letters **310**(5-6), 477–484 (1999).

[16] J. A. Horsley, P. Rabinowitz, A. Stein, D. M. Cox, R. O. Brickman, and A. Kaldor, "Laser Chemistry Experiments with Uf6," IEEE Journal of Quantum Electronics **16**(4), 412–419 (1980).

[17] R. D. Braun, *Introduction to Instrumental Analysis* (McGraw-Hill Book Co., New York, 1987).

[18] *http://www.wag.caltech.edu/home/jang/genchem/infrared.htm* (2007).

[19] J. A. Giordmanie and R. C. Miller, "Tunable Coherent Parametric Oscillation in LiNbO3 at Optical Frequencies," Phys. Rev. Lett. **14**(24), 973–976 (1965).

[20] R. Byer, *Parametric Oscillators and Nonlinear Materials, in Nonlinear Optics, P.G. Harper and B.S. Wherrett, Editors* (Academic Press, San Francisco, CA, 1977).

[21] R. L. Byer, "Quasi-Phasematched Nonlinear Interactions and Devices," Journal of Nonlinear Optical Physics and Materials **6**, 549–592 (1997).

[22] K. Burneika, M. Ignatavicius, V. Kabelka, A. Piskarskas, and A. Stabinis, "Parametric light amplification and oscillation in KDP with mode-locked pump," IEEE J. Quantum Electron. **8**(6), 574 (1972).

[23] J. A. Armstrong, N. Bloembergen, J. Ducuing, and P. S. Pershan, "Interactions between Light Waves in a Nonlinear Dielectric," Phys. Rev. **127**(6), 1918–1939 (1962).

[24] J. D. McMullen, "Optical Parametric Interactions in Isotropic Materials Using a Phase-Corrected Stack of Nonlinear Dielectric Plates," J. Appl. Phys. **46**(7), 3076–3081 (1975).

[25] E. J. Lim, M. M. Fejer, and R. L. Byer, "2Nd-Harmonic Generation of Green Light in Periodically Poled Planar Lithium-Niobate Wave-Guide," Electron. Lett. **25**(3), 174–175 (1989).

[26] A. Feisst and P. Koidl, "Current Induced Periodic Ferroelectric Domain-Structures in Linbo3 Applied for Efficient Nonlinear Optical Frequency Mixing," Appl. Phys. Lett. **47**(11), 1125–1127 (1985).

[27] M. Fujimura, K. Kintaka, T. Suhara, and H. Nishihara, "Linbo3 Wave-Guide Quasi-Phase-Matching 2Nd-Harmonic Generation Devices with Ferroelectric-Domain-Inverted Gratings Formed by Electron-Beam Scanning," Journal of Lightwave Technology **11**(8), 1360–1368 (1993).

[28] M. Yamada, N. Nada, M. Saitoh, and K. Watanabe, "1St-Order Quasi-Phase Matched Linbo3 Wave-Guide Periodically Poled by Applying an External-Field for Efficient Blue 2Nd-Harmonic Generation," Appl. Phys. Lett. **62**(5), 435–436 (1993).

[29] E. B. Treacy, "Compression of picosecond light pulses," Phys. Lett. A **28**(1), 34–35 (1968).

[30] O. Svelto and D. C. Hanna, *Principles of lasers*, 4th ed. (Plenum Press, New York, 1998).

[31] E. B. Treacy, "Optical Pulse Compression With Diffraction Gratings," IEEE J. Quantum Electron. **QE-5**(9), 454 (1969).

[32] W. E. Martin, B. C. Johnson, and K. R. Guinn, "Pulse Shaping for Laser Fusion," IEEE J. Quantum Electron. **13**(9), D53–D53 (1977).

[33] J. Agostinelli, G. Mourou, and C. W. Gabel, "Active Pulse Shaping in the Picosecond Domain," Applied Physics Letters **35**(10), 731–733 (1979).

[34] M. Stavola, J. A. Agostinelli, and M. G. Sceats, "Ultrafast Pulse Shaping with a Traveling Wave Kerr Cell and Picosecond Rise Time Electrical Pulses," Applied Optics **18**(24), 4101–4105 (1979).

[35] C. Froehly, B. Colombeau, and M. Vampouille, "Shaping and Analysis of Picosecond Light-Pulses," Prog. Optics. **20**, 65–153 (1983).

[36] P. W. Smith and A. M. Weiner, "Ultrashort Light-Pulses," IEEE Circuit. Devic. **4**(3), 3–7 (1988).

[37] A. M. Weiner, J. P. Heritage, and E. M. Kirschner, "High-Resolution Femtosecond Pulse Shaping," J. Opt. Soc. Am. B: Opt. Phys. **5**(8), 1563–1572 (1988).

[38] W. J. Tomlinson, R. J. Hawkins, A. M. Weiner, J. P. Heritage, and R. N. Thurston, "Dark Optical Solitons with Finite-Width Background Pulses," J. Opt. Soc. Am. B: Opt. Phys. **6**(3), 329–334 (1989).

[39] A. M. Weiner, R. N. Thurston, W. J. Tomlinson, J. P. Heritage, D. E. Leaird, E. M. Kirschner, and R. J. Hawkins, "Temporal and Spectral Self-Shifts of Dark Optical Solitons," Opt. Lett. **14**(16), 868–870 (1989).

[40] A. M. Weiner, Y. Silberberg, H. Fouckhardt, D. E. Leaird, M. A. Saifi, M. J. Andrejco, and P. W. Smith, "Use of Femtosecond Square Pulses to Avoid Pulse Breakup in All-Optical Switching," IEEE J. Quantum Electron. **25**(12), 2648–2655 (1989).

[41] A. M. Weiner, D. E. Leaird, G. P. Wiederrecht, and K. A. Nelson, "Femtosecond Pulse Sequences Used for Optical Manipulation of Molecular-Motion," Science **247**(4948), 1317–1319 (1990).

[42] O. E. Martinez, "3000 Times Grating Compressor with Positive Group-Velocity Dispersion - Application to Fiber Compensation in 1.3-1.6 Mu-M Region," IEEE J. Quantum Electron. **23**(1), 59–64 (1987).

[43] A. M. Weiner, J. P. Heritage, R. J. Hawkins, R. N. Thurston, E. M. Kirschner, D. E. Leaird, and W. J. Tomlinson, "Experimental-Observation of the Fundamental Dark Soliton in Optical Fibers," Phys. Rev. Lett. **61**(21), 2445–2448 (1988).

[44] A. M. Weiner, J. P. Heritage, and J. A. Salehi, "Encoding and Decoding of Femtosecond Pulses," Opt. Lett. **13**(4), 300–302 (1988).

[45] C. W. Hillegas, J. X. Tull, D. Goswami, D. Strickland, and W. S. Warren, "Femtosecond Laser-Pulse Shaping by Use of Microsecond Radiofrequency Pulses," Opt. Lett. **19**(10), 737–739 (1994).

[46] P. Tournois, "Acousto-optic programmable dispersive filter for adaptive compensation of group delay time dispersion in laser systems," Optics Communications **140**(4-6), 245–249 (1997).

[47] F. Verluise, V. Laude, Z. Cheng, C. Spielmann, and P. Tournois, "Amplitude and phase control of ultrashort pulses by use of an acousto-optic programmable dispersive filter: pulse compression and shaping," Optics Letters **25**(8), 575–577 (2000).

[48] H. H. Goldstine, *A history of numerical analysis from the 16th through the 19th century*, Studies in the history of mathematics and physical sciences (Springer-Verlag, New York, 1977).

[49] I. Newton, *Philosophiae naturalis principia mathematica* (Jussu Societatis Regiae ac Typis Josephi Streater, 1687).

[50] J. H. Holland, *Adaptation in natural and artificial systems: an introductory analysis with applications to biology, control, and artificial intelligence* (University of Michigan Press, Ann Arbor, 1975).

[51] S. Kirkpatrick, C. D. Gelatt, and M. P. Vecchi, "Optimization by Simulated Annealing," Science **220**(4598), 671–680 (1983).

[52] N. Metropolis, A. W. Rosenbluth, M. N. Rosenbluth, A. H. Teller, and E. Teller, "Equation of State Calculations by Fast Computing Machines," J. Chem. Phys. **21**(6), 1087–1092 (1953).

[53] L. Ingber, "Simulated Annealing - Practice Versus Theory," Mathematical and Computer Modelling **18**(11), 29–57 (1993).

[54] N. A. Naz, H. S. S. Hung, M. V. O'Connor, D. C. Hanna, and D. P. Shepherd, "Adaptively shaped mid-infrared pulses from a synchronously pumped optical parametric oscillator," Opt. Express **13**(21), 8400–8405 (2005).

[55] A. M. Weiner, "Femtosecond Optical Pulse Shaping and Processing," Prog. Quant. Electron. **19**(3), 161–237 (1995).

[56] M. M. Wefers and K. A. Nelson, "Analysis of Programmable Ultrashort Waveform Generation Using Liquid-Crystal Spatial Light Modulators," J. Opt. Soc. Am. B: Opt. Phys. **12**(7), 1343–1362 (1995).

[57] G. Imeshev, M. M. Fejer, A. Galvanauskas, and D. Harter, "Pulse shaping by difference-frequency mixing with quasi-phase-matching gratings," J. Opt. Soc. Am. B: Opt. Phys. **18**(4), 534–539 (2001).

[58] J. Prawiharjo, H. S. S. Hung, D. C. Hanna, and D. P. Shepherd, "Theoretical and numerical investigations of parametric transfer via difference-frequency generation for indirect mid-infrared pulse shaping," J. Opt. Soc. Am. B: Opt. Phys. **24**(4), 895–905 (2007).

Chapter 2

Optical Parametric Oscillators and Near to Mid-Infrared Pulse Transfer

2.1 Motivation for Chapter

The purpose of this chapter is to outline the basic theoretical considerations in choosing the experimental setup for the research, and to give a brief mathematical outline of the processes involved in pulse transfer. There is much literature regarding parametric processes dating back to the 1960's; the purpose of this research (and this chapter) is not to present new concepts or ideas, but to present existing knowledge within the context of pulse shaping. For the sake of brevity, many of the intermediate steps in the calculations are omitted since much of the work can be found in existing literature.

An introduction to optical parametric oscillators naturally leads to an understanding of how they can be used for transferring shaped pulses from the near- to mid-infrared. Since a crucial element of the OPO and the pulse transfer process is the phasematching crystal, this is discussed immediately afterwards. The crystal used in the research, as mentioned in the introduction, is periodically poled lithium niobate (PPLN), which is used with pico- to femto-second pulses in a synchronously pumped optical parametric oscillator. Any potential shortcoming in using this crystal and the parametric setup are also discussed.

2.2 Parametric interaction and Optical Parametric Oscillators

In 1961 Franken et. al. [1] demonstrated second harmonic generation of the output from a ruby laser in a quartz crystal. This was the first recorded instance of a nonlinear process being performed at optical wavelengths. Nonlinear optics differs from linear optics in the same way as all nonlinear phenomena do. That is to say, the response of the material (or system) is not linearly proportional to the influence upon it. In comparison, a linear system responds to varying degrees of influences proportionately, and multiple influences acting on the medium are the equivalent of each influence acting alone.

It was no coincidence that nonlinear optics was first observed soon after the invention of the laser, as it relies on optical pulses with electric field strengths comparable to those binding electrons to an atom. The Lorentz model of atoms in a dielectric medium is often used as a basis to understand and visualise the processes occurring in nonlinear optics. The model has been used to crudely predict the nonlinear susceptibility of materials, and this has added to its validity for use as a simple tool.

In this model the dielectric medium consists of an electron bound to an infinitely heavy nucleus. The electron is affected by external electric fields and this causes it to be displaced. The binding force between the nucleus and electron then causes the electron to be restored to its original position. For small displacements the result is analogous to simple harmonic oscillation of a spring, and like a spring, if the electron is displaced far from its equilibrium position, say by using an intense field, it undergoes anharmonic oscillations. The electron is a charged particle and the result of its anharmonic motion is to generate electromagnetic frequency components that differ from the driving frequency [2].

The response of a material to the total electric field ($\mathbf{E}$) can be described by the polarisation field ($\mathbf{P}$) in the time domain. The jth Cartesian component of the $\mathbf{P}$

field [3] can be written in an expanded series as:

$$\begin{aligned}\mathbf{P_j}(\mathrm{t}) &= \varepsilon_0\{\int_{-\infty}^{+\infty}\chi^{(1)}_{jk}(t-\tau)\mathbf{E_k}(\tau)d\tau \\ &+\int_{-\infty}^{+\infty}\chi^{(2)}_{jkl}(t-\tau_1,t-\tau_2)\mathbf{E_k}(\tau_1)\mathbf{E_l}(\tau_2)d\tau_1 d\tau_2 \\ &+\int_{-\infty}^{+\infty}\chi^{(3)}_{jklm}(t-\tau_1,t-\tau_2,t-\tau_3)\mathbf{E_k}(\tau_1)\mathbf{E_l}(\tau_2)\mathbf{E_m}(\tau_3)d\tau_1 d\tau_2 d\tau_3\}\end{aligned} \tag{2.1}$$

where $\chi^{(n)}$ is tensor of order $(n+1)$ and is called the nonlinear susceptibility, ε_0 is the electric permittivity of free space, and the subscript on the vectors is used to denote a component of the field and summation convention over repeated indices is implied. The integrals are required because matter does not respond instantaneously to light, and the delay is represented by a convolution in the variable τ. Furthermore, due to causality it is required that $\chi(t-\tau)=0$ for $t-\tau<0$.

Equation 2.1 can be understood by noting that the first term in the expression is the linear response of the system and for isotropic systems, this is a scalar quantity [4]. The remaining terms are related to the non-linear response and generally their magnitudes decrease with progression. The even order susceptibility tensors are only non-zero for materials which lack a centre of inversion symmetry, such materials are called non-centrosymmetric. The susceptibility tensor is generally a complex quantity but is significant in describing the optical properties of the material. This can be seen by taking the real and imaginary part of $\chi^{(1)}$. The real part of $\chi^{(1)}$ corresponds to the refractive index of the material $n(\omega)$, and the relationship is given by $n(\omega)=\sqrt{1+\mathbf{Re}(\chi^{(1)})}$, whereas the imaginary part of $\chi^{(1)}$ gives the absorption of the material, $\alpha(\omega)=\omega\left[\mathbf{Im}(\chi^{(1)})/n(\omega)c\right]$. Although there are many terms in equation 2.1, it is the second term that is responsible for many observable nonlinear phenomena and this term is responsible for the process by which an OPO predominately generates new frequencies of light, namely parametric difference frequency generation (DFG). Hence, higher terms are ignored when discussing the mathematical treatment.

In parametric difference frequency generation the energy of one photon, called the pump photon (p), is effectively split into two lesser energy photons, called the signal (s) and idler (i), under the restriction of energy and momentum conservation. The process is called difference frequency generation because it involves a pump and signal photon entering the nonlinear medium, the difference in energy between

these photons results in an idler photon being created and because of energy conservation, a second signal photon is generated. There is one variation to this scheme and that is to replace the incoming signal photon with an idler photon and therefore the difference between the energy of the pump and idler results in a signal photon being generated, with a new idler photon for conservation. The work in this project relies on DFG of the former type. Schematically, the process of DFG can be shown as:

$$(\omega_p) + \omega_{s,i} \rightarrow (\omega_i + \omega_s) + \omega_{s,i} \tag{2.2}$$

The actual mechanism by which DFG is achieved is due to the generation of a polarisation field; this mechanism is discussed shortly. But before reaching that point, an omission in the above description of the DFG process in relation to an OPO has to be clarified. As stated earlier the OPO consists of a nonlinear crystal within a resonator cavity. A pump photon enters the device and two photons of lesser energy are produced, with the mirrors of the OPO designed to reflect one or more frequencies. So the question is where does the initial signal photon come from to initiate the process? The full answer lies in a detailed quantum mechanical explanation, which is beyond the scope of this thesis. The problem can be treated classically by thinking of the electromagnetic modes as having a zero-point energy, which can provide an effective input field; details of this explanation as well as experimental results to back up these claims can be found in pages 431 - 435 of reference [5].

Returning to the issue of DFG within an optical crystal, the interaction of the signal and pump photons produces a polarisation field within the crystal. This polarisation field provides a source to generate new photons under momentum and energy conservation.

Momentum conservation is examined later, for now energy is considered. Energy conservation requires that the energy of the generated signal and idler photon be equal to the pump photon:

$$\hbar\omega_p = \hbar\omega_s + \hbar\omega_i \tag{2.3}$$

where $\hbar$ is Planck's constant divided by 2π and $\omega_{p,s.i}$ are the angular frequencies of the interacting photons, where the signal is of higher energy than the idler.

Analysing momentum conservation requires some thought. In analogy to energy conservation, the momentum conservation condition requires:

$$\hbar k(\omega_p) = \hbar k(\omega_s) + \hbar k(\omega_i) \tag{2.4}$$

Where $k(\omega)$ is called the wavevector (or k-vector) and is given by $k(\omega) = \omega n(\omega)/c$. For most materials the value of $k(\omega)$ far from atomic resonance is different depending on the frequency of light. So in most parametric situations equation 2.4 is not automatically satisfied. Equation 2.4 can be re-expressed as:

$$\Delta k_0 = k_p - k_s - k_i \tag{2.5}$$

where a new variable, Δk_0, called the wavevector mismatch is defined. In order to achieve efficient parametric conversion it is required that the polarisation field at any given time has the same phase relation to the photons it is creating. Otherwise, the newly generated photons are out of phase with previously generated photons of the same frequency, and this can result in destructive interference between the photons. The situation for perfect phasematching requires $\Delta k_0 = 0$. For an unphasematched parametric interaction, the distance after which the polarisation field and the generated photons go out of phase by more than π is called the coherence length l_{coh} and is given as:

$$l_{coh} = \frac{\pi}{k_p - k_s - k_i} \tag{2.6}$$

One method used to satisfy equation 2.4 is to use a birefringent material [6]. Birefringent materials have the property whereby light generally experiences a different refractive index depending on its propagation direction and polarisation. For the discussion on birefringent phasematching (BPM) the analysis is restricted to linearly polarised light, and uniaxial birefringent materials, that is to say materials which have one axis (called the optical or crystal axis) whereby light polarised perpendicular to it experiences the same refractive index, independent of crystal rotation about this axis. This is the most common situation when dealing with birefringent phasematching. For further simplicity, the discussion on birefringent phasematching is restricted to second harmonic generation (SHG). SHG is a parametric process in which two pump photons combine to form a single photon. However the effects of BPM are applicable to any parametric process, be it SHG or DFG.

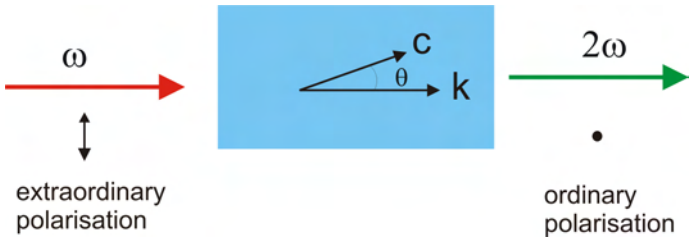

FIGURE 2.1: Schematic of birefringent phase matching for SHG in a negative uniaxial material. The red arrow represents the pump beam, while the green arrow is the second harmonic generated beam

In general, with birefringent phasematching the polarisation of the pump, signal, and idler can either be aligned with each other, or one or more beams can have a polarisation 90 degrees to the others. There are two ways to achieve birefringent phasematching, the first methods is called "noncritical phasematching". In this situation, the second harmonic and pump beam travel through the crystal in the same direction. The polarisation of the pump beam is aligned to either the fast (lowest refractive index) or slow (highest refractive index) axis of refraction, and the signal is aligned to the other refractive index axis. By adjusting the temperature of the material it is sometimes possible to achieve the same refractive index for both beams, and therefore the phase velocity of the beams is the same; and as a result, the polarisation field remain in-phase with the generated photons during the length of the crystal. The other method for achieving birefringent phasematching is called "critical phasematching", sometimes called angle phasematching. This type of phasematching is more difficult as it requires precise angular tuning. Critical phasematching is best explained using a diagram, see figure 2.1. From figure 2.1 the crystal axis is shown by the arrow labelled c. The refractive index experienced by light perpendicular to the crystal axis is called the "ordinary refractive index", $n_o(\omega)$, it is called this because it does not change with the direction of propagation (k). Likewise light which is polarised in the plane between the c-axis and the propagation direction experiences a component of the "extraordinary refractive index" $n_e(\theta, \omega)$, this refractive index depends on the angle θ, as shown in the figure. For a positive uniaxial material, as shown here, the extraordinary refractive index is always greater than $n_o(\omega)$, and for the case of a negative uniaxial materials, $n_e(\theta, \omega) < n_o(\omega)$ is always true. To achieve efficient SHG with a positive uniaxial material the pump light is polarised in the plane containing the crystal axis and the propagation axis, in the figure this is shown by the vertical bar with arrows at each end to represent polarisation in the vertical direction. The second harmonic

is polarised in the orthogonal direction, shown in the diagram by a single dot, which represents polarisation in the plane in-and-out of the page. By adjusting the angle θ, it is sometimes possible for both the pump and second harmonic beam to experience the same refractive index and therefore they propagate through the material with the same phase velocity and hence the polarisation field stays in phase with its generated photons. As indicated critical phasematching requires precise angular tuning, this condition necessarily requires incoming beams with less divergence compared to noncritical phasematching. Critical phasematching also suffers from a phenomenon called spatial walkoff. Spatial walkoff occurs when a beam experiences the extraordinary polarisation of the material and propagates at an angle to the optical axis. In this situation the beam's direction of energy flow (Poynting vector) does not correspond to the propagation direction of the beam, as defined by the k-vector, instead there is a small angular difference between them called the walkoff angle. A beam that experiences only the ordinary refractive index does not experience spatial walkoff. Because of this anisotropy in Poynting vectors, there is a limit on the crystal length over which two beams can remain spatially overlapped. So far BPM has been discussed for the case of SHG. Birefringent phasematching can also be used for difference frequency generation. However, the refractive index experienced by the various beams should not be the same (as in the case of SHG), rather they should obey the following formula (which is derived from 2.4)

$$\omega_p n(\omega_p) = \omega_i n(\omega_i) + \omega_s n(\omega_s) \tag{2.7}$$

where n is the refractive index; and can be determined for varying wavelengths using the Sellmeier equation with appropriate constants [7]. More information on BPM can be found in reference [8]. Birefringent phasematching naturally relies on finding materials that possess the right amount of anisotropy in their refractive index, and as stated in the introduction, this severely restricts the number of crystals available for use in parametric devices.

Quasi-phasematching [8] (QPM) is an alternative to birefringent phasematching. It allows efficient parametric conversion without requiring the wavevectors of the various photons to be the same, thus the restriction of birefringence is lifted from the set of possible nonlinear crystals. The material used for the research is QPM lithium niobate.

The principle behind QPM is that after one coherence length, an unphasematched parametric process has yielded its maximum intensity, from there on the reverse process is favoured. So by the end of a second coherence length the overall parametric gain has reached zero. QPM overcomes this problem by periodically reversing the sign of the nonlinear susceptibility coefficient. In the case of ferroelectric materials, such as a lithium niobate, this is achieved by reversing the domain structure every mth coherence length, where m is an odd integer. The most common value of m is one, and this corresponds to the case of reversing the sign of the nonlinear susceptibility coefficient every coherence length. When m is equal to one, the type of phasematching is called first-order phasematching.

The effect of periodically changing the sign of the nonlinear susceptibility coefficient is that it introduces a π phase change in the driving polarisation field; this compensates for a non-zero wavevector mismatch and effectively reset the polarisation field so that it is in phase with the generated photons. If the poling is done correctly this means that the generated intensity continues to grow in the second coherence length. Poling the material does not affect the phase velocities of the photons, so after the second coherence length the polarisation field is out of phase with the generated photons and the sign of the nonlinear coefficient must be switched again. Higher order phasematching, such as third-order phasematching is useful in some situations because it allows the period of the poling to be increased, which puts less strain on the fabrication process. It is particularly useful in cases where the coherence length is very short, such as when the pump light is in the ultraviolet. Figure 2.2 shows theoretical parametric growth with various poling orders and for the case of ideal phasematching and for no phasematching. It can be noted that poling can be achieved by modulating the linear susceptibility of the material, but this is difficult to achieve [9].

The periodic reversal of the nonlinear susceptibility coefficient can be expressed as an additional term on the right-hand side of the momentum equation 2.4, namely $k_G = \frac{2\pi}{\Lambda}m$ [9], where Λ is the period of poling and m represents the order of phasematching. Equation 2.5 can then be re-expressed as:

$$\Delta k_0 = k_p - k_s - k_i - k_G \tag{2.8}$$

Again, for efficient phasematching Δk_0 should be equal to zero. The use of poling allows great flexibility in generating new wavelengths. Several periodic patterns can be poled along side each other, thus by simply translating the crystal within

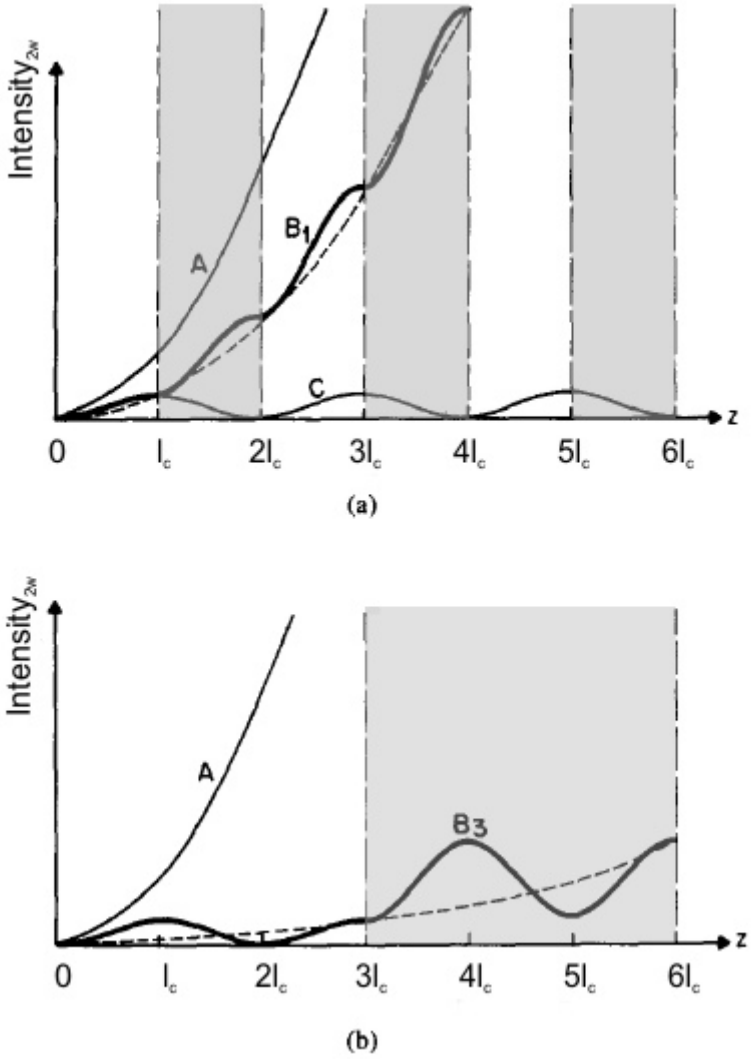

FIGURE 2.2: Graphs showing characteristic second-harmonic parametric intensity growth with distance along a nonlinear crystal, where l_c represents one coherence length. Figure (a): Ideal phasematching is shown in curve A, which also represents birefringent phase-matching, curve B1 represents first-order phasematching, curve C corresponds to the case of non-phasematched growth. Figure (b): graph B3 illustrates third-order phasematching, while graph A represent ideal phasematching. Reprinted from Ref [9] with minor modifications.

the setup, new frequency components can be generated with minimal fuss. Another advantage of not relying on birefringence phasematching is that it allows greater freedom in choosing the orientation of the crystal. This is important because the nonlinear susceptibility coefficient (as shown in equation 2.1) is usually not symmetric with orientation, and some tensor components have higher values than others do. Compared to birefringent phasematching, poling decouples the link between phasematching and the orientation of the crystal. Thus, one can pole the crystal such that the largest tensor component is used in the parametric process. For the case of lithium niobate, QPM is able to access the largest nonlinear coefficient (which is a measure of the nonlinearity and is given as half the value of the susceptibility coefficient, $d = \frac{1}{2}\chi^{(2)}$) of $34\,pm/V$ [9]. In comparison, the highest value available for birefringent phasematching is about $5.9\,pm/V$ [9]. However, as can be seen from Figure 2.2, with the nonlinear coefficients being equal, QPM does not increase the intensity as quickly as ideal phasematching. To take this into account one usually uses an effective nonlinear coefficient (d_{eff}). For ideal first order QPM the effective nonlinear coefficient is given by $d_{eff} = \frac{2}{\pi}d$. Sometimes d_{eff} is chosen to be a lower value in order to account for slight errors in the poling process. The most significant source of error is in the poling duty cycle [10]. This should be 50/50, but due to random and systematic errors this is not always the case. First-order periodic poled lithium niobate (PPLN) operating in the infrared has a typical random duty cycle error of 10%, and a typical systematic error of another 10% [10]. This reduces the gain to within 86% of its maximum value [10]. The culmination of all these factors is included in the effective nonlinear coefficient.

The quasi-phasematching grating is designed for a specific pump, signal, and idler wavelength. However, the nonlinear crystal used in this research is used with short pump pulses, which have an associated spectral bandwidth, care must be taken to ensure the nonlinear crystal can phasematch the whole of this bandwidth. It is intuitively expected that wavelengths close to the design wavelength (λ_0) are fairly well phasematched with the driving polarisation field. The issue with wavelengths far from the design wavelength is that they travel at a significantly different phase-velocity than λ_0. Over the length of a long crystal, this difference accumulates and results in these wavelengths being out of phase with the driving polarisation field, hence wavelengths far from λ_0 are not properly phasematched. The spectral bandwidth of the pump that a crystal can accept for phasematching a parametric process is called the acceptance bandwidth ($\delta\lambda_p$). The acceptance bandwidth is

determined by detuning the pump wavelength away from the design wavelength and observing the reduction in the parametric gain. The acceptance bandwidth is thus defined as the range of pump wavelengths by which the parametric gain falls by no less than half its maximum value. It was shown by Fejer et. al. [9] that the acceptance bandwidth can be described by the following equation:

$$\delta\lambda_p = \frac{5.57}{L}\left|\frac{\partial\Delta k_0}{\partial\lambda}\right|^{-1} \tag{2.9}$$

where L is the length of the crystal. The equation shows that shorter crystals accept a larger pump spectral bandwidth. This is intuitive since the accumulated phase difference between the design wavelength and those far from it would be smaller.

Other than the ability to be poled, and demonstrate a high effective nonlinear coefficient (d_{eff}), lithium niobate has several other advantages that make it suitable for our requirements. These include a high melting point of $1253°C$ and a Curie temperature of about $1210°C$ [11] (exact values for both temperatures depend on the actual chemical composition of the material, including impurities). The material also exhibits good mechanical stability; high molecular stability with respect to ageing in a laboratory environment, and finally it is highly transparent in the range between 0.35 and $5.2\,\mu m$ [12], which puts it in the range of possible future applications. It is interesting to note that OPOs have been demonstrated to operate well into the absorption regime of lithium niobate. Watson et. al. have shown operation of an OPO with idler output to $7.3\,\mu m$ [13], which may prove useful in certain applications.

Lithium niobate unfortunately suffers from optically-induced inhomogeneities in its refractive index (photo-refractive effect). This is caused when light is able to excite free charge carriers within the material that leads to a space-charge separation, and due to the electro-optical effect this causes a localised variation in the refractive index. The result is that wavefronts of light passing through the material are distorted, and this reduces the conversion efficiency of the device. Fortunately, this effect can be reduced by raising the temperature of the material, which induces a homogeneous separation of the free charge carriers throughout the material and thus removes them from the influence of the photo-refractive effect [2]. Raising the temperature above $\approx 100°C$ for near infrared processes is sufficient to reduce the photo-refractive effect to within tolerable limits.

2.3 Ultrashort Pulse Parametric Interaction

In this work ultrashort pulses are temporally shaped by a pulse shaper and are then converted to a different wavelength using an OPO. The understanding of ultrashort pulse parametric interaction is important to understand any limitations on the transfer process. Compared to continuous-wave (CW) interaction, ultrashort pulse interactions are more difficult to understand. Part of this is because general analytical solutions can not be found and modelling of short-pulse interaction must be performed numerically. However numerical modelling makes it harder to develop intuition about the problem and this can hinder understanding.

This section of the chapter examines some of the unique features of ultrashort pulses. It uses existing theory to understand and foresee any issues arising from their use. A mathematical treatment of ultrashort pulse parametric interaction is discussed to put the discussion on a more rigorous grounding. The mathematical treatment used has been performed by Imeshev et. al. [14–16] and those results are used to understand the pulse transfer processes.

The unique features of short pulse interaction occur because of their large spectral bandwidths. It can be immediately seen that this causes a problem with the conversion efficiency of the parametric process because, as described above, the traditional QPM device is designed for maximum conversion efficiency at one wavelength. This point is elaborated in more detail later in the text.

The large spectral bandwidth of a pulse results in noticeable chromatic dispersion. Figure 2.3 uses data from reference [7] to show a plot of the group velocity versus wavelength for lithium niobate.

As discussed earlier, the OPO relies on difference frequency generation between the pump and signal beams to produce an idler and new signal. As the signal and pump beams are of different central wavelengths they travel through the crystal with different speeds (group velocities). The difference between the group velocities is called the group velocity mismatch (GVM). If the two pulses enter the crystal at the same time, then due to GVM they will begin to separate in time. Figure 2.4 shows a schematic of the process. After a length L_{gv} the pulses have little temporal overlap and the desired parametric interaction is substantially reduced. The relationship between L_{gv} and the temporal full width at half maxima

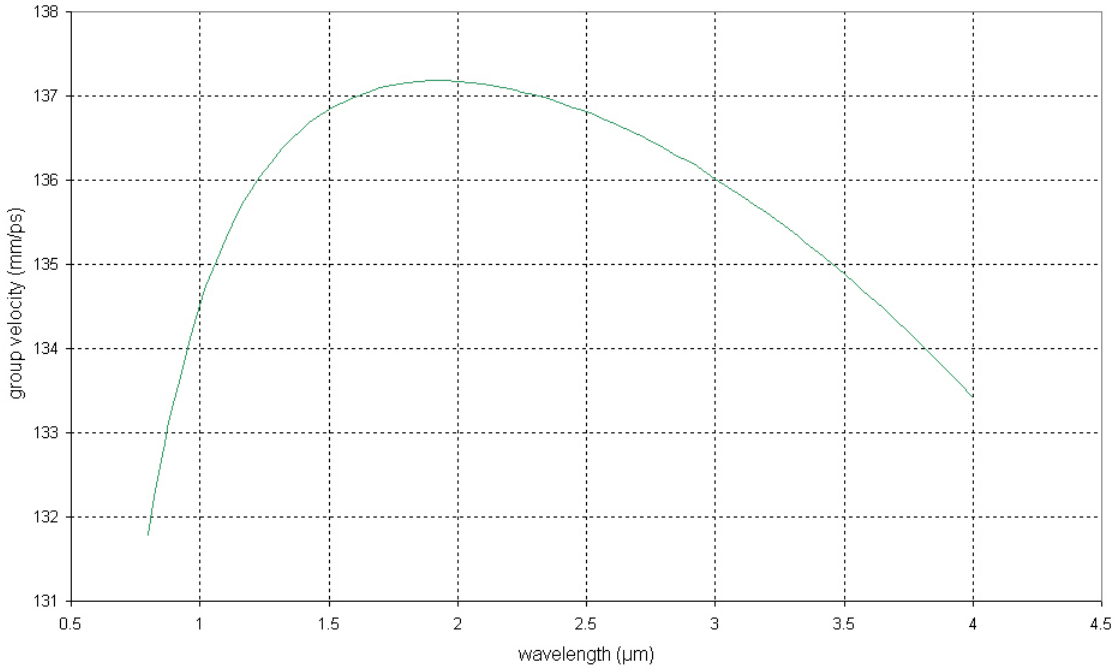

FIGURE 2.3: Theoretical plot of group velocity versus wavelength in congruent lithium niobate. The graph was produced using data and a modified Sellmeier equation as presented by Jundt in Ref [7] The plot is for extraordinary polarised light propagating along the crystal axis and for a temperature of 150 $°C$

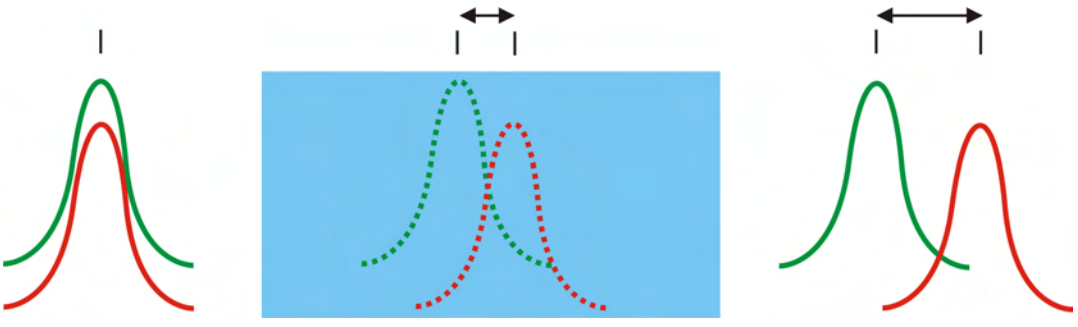

FIGURE 2.4: Schematic diagram showing the effects of group velocity mismatch. Two pulses of different central wavelengths enter the nonlinear crystal at the same time. But due to chromatic dispersion one of them travels faster than the other and upon leaving the crystal they are temporally separated.

(FWHM) of the widest pulse (τ) is given by:

$$L_{gv} = \frac{\tau}{\mid \delta\upsilon \mid} \tag{2.10}$$

where $\mid \delta\upsilon \mid$ is the absolute group velocity mismatch parameter and is discussed fully in section 2.4. Crystals that have a length greater than L_{gv} can result in a distorted signal pulse and this does not confer any advantages for OPO performance. Hence, the crystal length is restricted to $\leq L_{gv}$.

Another consideration arising from chromatic dispersion occurs within the pulse. Since the pulse consists of a finite spectral bandwidth, different frequency components of the pulse travel at different velocities, this is called group velocity dispersion (GVD). The result of GVD is that a bandwidth-limited pulse travelling through a material is temporally broadened. It is inferred from this that the pulse leaving the material has a non-flat phase, as would be the case for a bandwidth-limited pulse. With most materials, if the dispersion curve is observed far away from atomic resonances, it is found that shorter wavelengths of light travel at a lower velocity than longer wavelengths, this is called normal dispersion. Pulses that travel through this kind of material are said to have acquired a positive chirp. The contrary case is when a pulse passes through a material in which longer wavelengths travel at a lower velocity than shorter wavelengths. This is called anomalous dispersion and the pulse acquires a negative chirp. In many applications it is desirable to cancel the positive chirp on a pulse, but due to the rarity of anomalous dispersive materials at arbitrary wavelengths the effect is often performed "artificially" with the use of a suitable arrangement of dispersive optical elements, such as prisms or gratings, or a combination of both. GVD becomes more important for shorter pulses and longer crystal lengths. The length of crystal over which GVD becomes important is called the dispersion length, L_β. This is related to the pulse width (τ) via the GVD parameter (β) [17] as:

$$L_\beta = \frac{\tau^2}{\beta} \tag{2.11}$$

GVD is a problem for OPOs that operate with femtosecond pulses as it increases the threshold for oscillation and produces chirped pulses. In order to achieve femtosecond transform-limited signal pulses, dispersion compensation is often incorporated within the OPO. This is usually achieved using intracavity prisms [18, 19].

Another feature of GVD is its ability to change the signal wavelength with detuning of the SPOPO cavity length [20]. This phenomena occurs because changing the cavity length results in the signal pulse no longer being synchronised with the pump pulse, therefore the signal sees a reduction in parametric gain. However, it is possible for a signal pulse to re-achieve synchronism by changing its central wavelength, such that, the new wavelength results in a change of group-velocity in the nonlinear crystal which compensates for the change in length.

2.4 Model of Short Pulse Propagation in Difference Frequency Generation

So far only specific considerations of the OPO have been examined. These considerations can be tied together on a more rigorous basis by modelling the propagation of a short optical pulse through a QPM OPO. As stated earlier short pulses are harder to model mathematically and it is not the purpose of this research to extend this area. However, some understandings of the mathematics of the problems are crucial for gaining insight into the issues arising from mid-infrared pulses shaping.

The mathematical model for short pulse propagation in DFG is described by Imeshev et. al. [14–16] and is described below with the aim of tying together the above ideas, and gaining some intuition about the pulse transfer process and its limitations.

For simplicity, pulse propagation in only one dimension (z direction) is considered. Other assumptions are that the material has no free charge carriers, is non magnetic, does not absorb any of the incoming light, is isotropic, and the spectrum of the pump, signal, and idler do not overlap. These are all reasonable assumptions for the material and experimental setup used throughout this research.

The model of short pulse DFG begins with Maxwell's equations in one dimension, and in the frequency domain:

$$\nabla \times \hat{\mathbf{E}}(\mathrm{z}, \omega) = -i\omega \hat{\mathbf{B}}(\mathrm{z}, \omega) \tag{2.12a}$$

$$\nabla \times \hat{\mathbf{H}}(\mathrm{z}, \omega) = \mathrm{i}\omega \hat{\mathbf{D}}(\mathrm{z}, \omega) \tag{2.12b}$$

Where $\hat{\mathbf{E}}(\mathrm{z},\omega)$, $\hat{\mathbf{B}}(\mathrm{z},\omega)$, $\hat{\mathbf{H}}(\mathrm{z},\omega)$, $\hat{\mathbf{D}}(\mathrm{z},\omega)$ are the Fourier transforms of the full electric field, magnetic field, magnetic displacement, and electric displacement vectors respectively and ω is the angular frequency. Since the equations are in the frequency domain the polarisation field given by eqn 2.1 is also Fourier transformed into the frequency domain, for simplicity it is split into its linear and nonlinear parts to give:

$$\hat{\mathbf{P}}(z,\omega) = \varepsilon_0 \chi^{(1)}(z,\omega)\hat{E}(\mathrm{z},\omega) + \mathbf{P}_{NL}\hat{(}z,\omega) \tag{2.13}$$

The constitutive Maxwell relations are given as:

$$\hat{\mathbf{D}}(\mathrm{z},\omega) = \varepsilon_0 \varepsilon(\omega)\hat{\mathbf{E}}(\mathrm{z},\omega) + \hat{\mathbf{P}_{\mathrm{NL}}}(\mathrm{z},\omega) \tag{2.14}$$

$$\hat{\mathbf{B}}(\mathrm{z},\omega) = \mu_0 \hat{\mathbf{H}}(\mathrm{z},\omega) \tag{2.15}$$

where μ_0 is the permeability of free space, ε_0 is the permittivity of free space, $\varepsilon(\omega)$ is the dielectric constant of the material, and the relationship $\varepsilon(\omega) = (1 + \chi^{(1)})$ has been used.

It is assumed throughout the analysis that the QPM material is designed for difference frequency generation between the pump and signal pulse and that all other parametric process are unphasematched and hence can be ignored. So far all the assumptions up to this point have been reasonable. But in order to continue with this analytical analysis it is required that the pump is assumed to be undepleted and the signal unamplified. These are common approximations in parametric theories. However, they place a limitation on the accuracy of this treatment and it is for this reason that numerical simulations are often required for a better treatment. This last point may sound like a severe restriction on the validity of the model but this is not necessarily the case. It has been shown mathematically that OPOs are most efficient when they are operated about 2-4 times above threshold [6, 21]. If an OPO is operated too far above threshold then unfavourable back-conversion of the idler and signal photons into a pump photon becomes significant. Furthermore, nonlinear processes other than the desired DFG between pump and signal become apparent. These processes can result in the observation of new wavelengths close to the desired signal wavelength [22].

Continuing with the analysis, the above equations can be used to form a set of equations to describe the propagation of the three pulses through the material:

$$\frac{\partial^2 \hat{\mathbf{E}}_{\mathrm{i}}(z,\omega)}{\partial z^2} = -k^2(\omega)\hat{\mathbf{E}}_{\mathrm{i}}(z,\omega) - \mu_0\omega^2\hat{\mathbf{P}_{\mathbf{NL}}}(z,\omega) \tag{2.16a}$$

$$\frac{\partial^2 \hat{\mathbf{E}}_{\mathrm{s}}(z,\omega)}{\partial z^2} = -k^2(\omega)\hat{\mathbf{E}}_{\mathrm{s}}(z,\omega) \tag{2.16b}$$

$$\frac{\partial^2 \hat{\mathbf{E}}_{\mathrm{p}}(z,\omega)}{\partial z^2} = -k^2(\omega)\hat{\mathbf{E}}_{\mathrm{p}}(z,\omega) \tag{2.16c}$$

where the subscripts i,s,p represent the idler, signal, and pump respectively. To solve equation 2.16 Imeshev et. al. assume that the electric field of the various pulses can be described by the following general equation:

$$\hat{\mathbf{E}_m}(z,\omega) = \hat{\mathbf{A}_m}(z,\Omega_m)\exp[-ik(\omega_m+\Omega_m)z] \tag{2.17}$$

where the m subscript is used to represent either the pump, signal, or idler, ω_m is the central frequency, $\Omega_m = \omega - \omega_m$ is the frequency detuning from the central frequency and $\hat{\mathbf{A}_m}(z,\Omega_m)$ is the frequency domain envelope of the pulse (and should not be confused with the temporal envelope). Using eqn 2.16 and 2.17 the output for the idler envelope after propagating a length L of the crystal can be determined as:

$$A_i(L,\Omega_i) = -i\gamma\int_0^L d(z)dz\int_{-\infty}^{+\infty} d\Omega_s \hat{\mathbf{A}_\mathbf{s}}^*(\Omega_s)\hat{\mathbf{A}_\mathbf{p}}(\Omega_i+\Omega_s)\exp[i\Delta k(\Omega_s,\Omega_i)z] \tag{2.18}$$

where $\gamma \equiv 2\pi/(\lambda_i n_i)$, λ_i is the idler wavelength, n_i is the refractive index at the idler wavelength, $d(z) \equiv \frac{1}{2}\chi^{(2)}(z)$ is the nonlinear coefficient (the spatial dependence is to account for the periodic domain reversal of QPM materials) and $\Delta k(\Omega_s,\Omega_i)$ is the k-vector mismatch given by:

$$\Delta k(\Omega_s,\Omega_i) = k(\omega_p+\Omega_s+\Omega_i) - k(\omega_i+\Omega_i) - k(\omega_s+\Omega_s) \tag{2.19}$$

Equations 2.18 and 2.19 are slightly different from the equations presented by Imeshev et. al. In their treatment they derive the equations by performing a convolution with respect to the pump frequency, but here it has been performed with respect to the signal frequency, as shown by Prawiharjo et. al [23]. Equation 2.18 is the most general equation for describing pulse transfer, but can not be solved for arbitrary pump and signal frequency envelopes. However the equation is important in understanding some of the principles of the pulse shaping process,

and can be used to put on a more firm footing some of the principles of an OPO mentioned so far.

As can readily be seen by equation 2.18 the idler frequency envelope is not a convolution between the pump and the signal; it only becomes a convolution when $\Delta k = 0$. As mentioned before, the near-infrared (NIR) pump pulse is temporally shaped before entering the OPO and this shape is transferred onto the mid-infrared (MIR) idler pulse. For a good transfer fidelity equation 2.18 suggests that the resonating signal should have a narrow spectral bandwidth. In practise, this is achieved by placing optical component(s) within the OPO cavity, so as to restrict the signal bandwidth.

Another consideration from equation 2.18 lies in the k-vector mismatch. This has an effect on the transfer process. Its effect can be analysed by expanding equation 2.19 in a double Taylor series expansion to give:

$$\begin{aligned}\Delta k(\Omega_s, \Omega_i) &= \Delta k_0 + \delta\nu_{ps}\Omega_s + \delta\nu_{pi}\Omega_i + \frac{1}{2}\delta\beta_{ps}\Omega_s^2 + \frac{1}{2}\delta\beta_{pi}\Omega_i^2 + \beta_p\Omega_s\Omega_i \\ &+ \sum_{n=3}^{\infty}\left\{\frac{1}{n!}\left[\Omega_s\frac{d}{d\Omega_s} + \Omega_i\frac{d}{d\Omega_i}\right]^n \Delta k\right\}\end{aligned} \tag{2.20}$$

where $\Delta k_0 = k(\omega_p) - k(\omega_s) - k(\omega_i)$ is the k-vector mismatch of the central frequencies , $\delta\nu_{ps} = \frac{1}{u_p} - \frac{1}{u_s}$ is the pump-signal group velocity mismatch (GVM) parameter, $\delta\nu_{pi} = \frac{1}{u_p} - \frac{1}{u_i}$ is the pump-idler GVM parameter where $u_m = [dk(\omega)/d\omega]^{-1}|_{\omega=\omega_m}$ are the group velocities, and $\delta\beta_{ps} = \beta_p - \beta_s$ is the pump-signal group velocity dispersion (GVD) mismatch, $\delta\beta_{pi} = \beta_p - \beta_i$ is the pump-idler GVD mismatch where $\beta_m = d^2k(\omega)/d\omega^2|_{\omega=\omega_m}$ is the group velocity dispersion (GVD) parameter. Naturally the Taylor series can continue beyond the second, it is therefore important to know when to stop. A suitable stopping criterion should depend on the explicit value of the derivatives of the k-vector mismatch. These derivatives have a physical meaning and represent higher order dispersion of the pulse. The characteristic length at which a higher order dispersive term becomes important for a pulse of width τ_0 is given by the equation [24]:

$$L_{\beta mn} = \frac{\tau_0^n}{|\beta_{m_n}|} \tag{2.21}$$

where the subscript m represents a reference to the pump, signal, or idler pulse, and $\beta_{m_n} = d^n k(\omega)/dk^n$ is the dispersion parameter of order n (with $n = 2$ corresponding to GVD as discussed earlier). β_{m_n} can be evaluated for a particular material

by using the Sellmeier equation and the corresponding material co-efficients. A quick calculation can then be done to determine the significance of higher order dispersion within the material. The nonlinear material used in this research is lithium niobate and the typical pulse durations are between $0.7 - 4\,ps$, with a range of wavelength between $1 - 4\,\mu m$. It is found that progressively higher order dispersion is only problematic for increasing lengths of crystal. GVD is noticeable if the characteristic length of the nonlinear crystal is typically a few meters in length and third order dispersion is important for nonlinear crystals that are typically a few kilometers in length. Hence it is expected for our experiments that pulse broadening due to GVD and higher order dispersion is not significant.

Equation 2.20 also shows that mismatch between the group-velocities and GVDs could affect the pulse transfer process. GVM is an issue for many parametric devices. It can be seen from graph 2.3 that there are instances where the group velocity between two wavelengths can be the same, but since all three pulses have different central wavelengths it is impossible for them all to have the same group-velocity. Group-velocity mismatch between the pump and typical signal wavelengths restricts the parametric process in our nonlinear crystal to a length of about 1 cm. Finally, a plot of GVD versus wavelength (figure 2.5) shows that unlike the plot of group-velocity there is no situation in which two wavelengths can have the same GVD.

The analysis of the pulse transfer process can be simplified if it possible to approximate the signal pulse as a continuous wave (CW) beam. Imeshev et. al. have shown the reverse case, that of approximating the pump to a continuous wave [16]. However, due to the generality of their reasoning, their results and can be applied to the signal pulse. Therefore showing that if the duration of the signal pulse, τ_s, can be made significantly longer than the accumulated group-velocity mismatch over the length of the crystal $\tau_s = L \mid \delta\upsilon_{ps} \mid$, where L is the length of the crystal, then signal pulse can be regarded as CW. This situation doesn't arise naturally, since to a first approximation the temporal width of the signal pulse is the same as the pump. However, it is possible to increase the duration of the signal pulse by restricting its spectral bandwidth. This can be achieved by inserting wavelength selective optics inside the OPO. Using standard optical elements such as birefringent filters and etalons it is possible to have a pump pulse of $1\,ps$ in duration and to increase the resonating signal pulse to about $4\,ps$. Thus, using a crystal

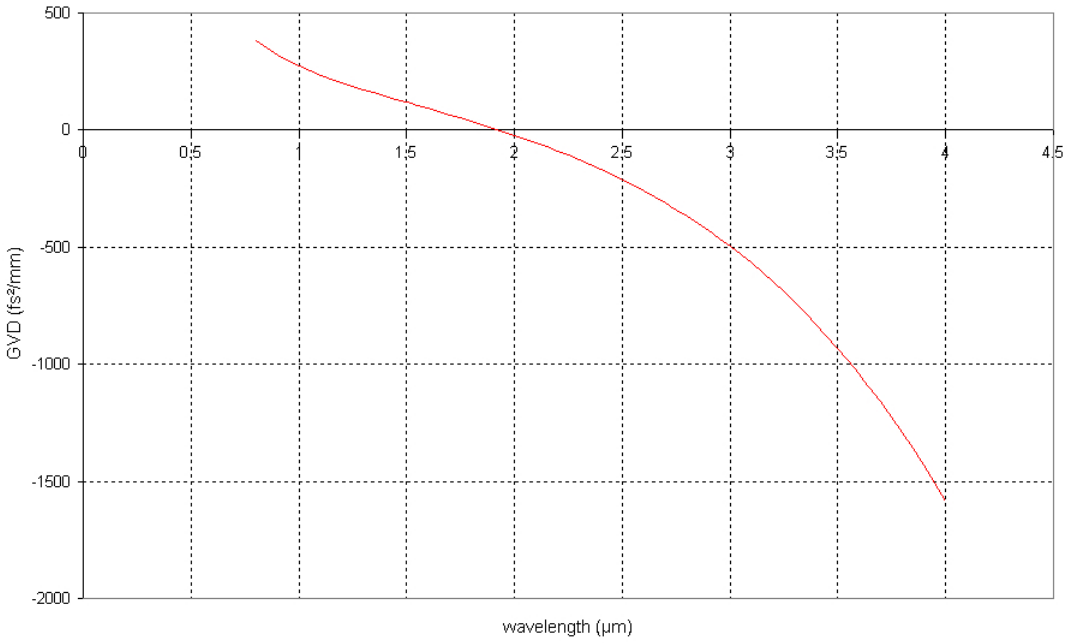

FIGURE 2.5: Theoretical plot of GVD versus wavelength for lithium niobate. Plot constructed using the modified Sellmeier equation and parameters presented in Ref [7], plot corresponds to a temperature of $150°C$ with light polarised along the c-axis, and propagating perpendicualar to it

of $1\,cm$ in length it is possible to achieve the CW signal approximation. This approximation is useful since short pulse parametric DFG is difficult to understand mathematically. It is for this reason that analysis for CW beams is often used as a first approximation to describe experimental results. CW approximations are used throughout this work with relevant justifications.

2.5 Conclusion

The analysis shown above indicates that pulse transfer from the near to mid infrared could be possible. In order to achieve good spectral transfer it is necessary to restrict the spectrum of the signal pulse. Furthermore, some considerations are necessary to reduce the effects of a non-zero Δk, these are investigated in the experimental chapters.

The mathematical treatment of Imeshev et. al. has some clear limitations, such as only being true for negligible pump depletion and signal amplification. We can take some consolation from knowing that transfer of temporally shaped pulses

from one wavelength to another has been achieved using an alternative type of DFG device, an optical parametric amplifier (OPA) [25–29]. However, the use of an OPO to achieve arbitrary temporal pulse transfer has never been performed before. Furthermore, OPOs are typically quite efficient devices and can result in significant pump depletion. Therefore, experimental verification is required to test the spectral fidelity of the transfer process.

2.6 References

[1] P. A. Franken, A. E. Hill, C. W. Peters, and G. Weinreich, "Generation of Optical Harmonics," Phys. Rev. Lett. **7**(4), 118–119 (1961).

[2] R. W. Eason and A. Miller, *Nonlinear optics in signal processing*, Engineering aspects of lasers series, 1st ed. (Chapman and Hall, London; New York, 1993).

[3] A. C. Newell and J. V. Moloney, *Nonlinear Optics*, 1st ed. (Addison-Wesley Publishing Company, New York, 1992).

[4] R. W. Boyd, *Nonlinear optics* (Academic Press, Boston, 1992).

[5] A. Yariv, *Quantum electronics*, 3rd ed. (Wiley, New York, 1989).

[6] R. Byer, *Parametric Oscillators and Nonlinear Materials, in Nonlinear Optics, P.G. Harper and B.S. Wherrett, Editors* (Academic Press, San Francisco, CA, 1977).

[7] D. H. Jundt, "Temperature-dependent Sellmeier equation for the index of refraction, n(e), in congruent lithium niobate," Opt. Lett. **22**(20), 1553–1555 (1997).

[8] R. W. Boyd, *Nonlinear optics*, 2nd ed. (Academic Press, San Diego, CA, 2003).

[9] M. M. Fejer, G. A. Magel, D. H. Jundt, and R. L. Byer, "Quasi-Phase-Matched 2Nd Harmonic-Generation - Tuning and Tolerances," IEEE J. Quantum Electron. **28**(11), 2631–2654 (1992).

[10] L. E. Myers and W. R. Bosenberg, "Periodically poled lithium niobate and quasi-phase-matched optical parametric oscillators," IEEE J. Quantum Electron. **33**(10), 1663–1672 (1997).

[11] K. G. Deshmukh and K. Singh, "Domain-Structure in Lithium-Niobate Single-Crystals," Journal of Physics D Applied Physics **5**(9), 1680 (1972).

[12] W. Brunner and H. Paul, "Theory of Optical Parametric Amplification and Oscillation," Prog. Optics. **15**, 3–75 (1977).

[13] M. A. Watson, M. V. O'Connor, P. S. Lloyd, D. P. Shepherd, D. C. Hanna, C. B. E. Gawith, L. Ming, P. G. R. Smith, and O. Balachninaite, "Extended operation of synchronously pumped optical parametric oscillators to longer idler wavelengths," Opt. Lett. **27**(23), 2106–2108 (2002).

[14] G. Imeshev, M. A. Arbore, M. M. Fejer, A. Galvanauskas, M. Fermann, and D. Harter, "Ultrashort-pulse second-harmonic generation with longitudinally nonuniform quasi-phase-matching gratings: pulse compression and shaping," J. Opt. Soc. Am. B: Opt. Phys. **17**(2), 304–318 (2000).

[15] G. Imeshev, M. A. Arbore, S. Kasriel, and M. M. Fejer, "Pulse shaping and compression by second-harmonic generation with quasi-phase-matching gratings in the presence of arbitrary dispersion," J. Opt. Soc. Am. B: Opt. Phys. **17**(8), 1420–1437 (2000).

[16] G. Imeshev, M. M. Fejer, A. Galvanauskas, and D. Harter, "Pulse shaping by difference-frequency mixing with quasi-phase-matching gratings," J. Opt. Soc. Am. B: Opt. Phys. **18**(4), 534–539 (2001).

[17] D. L. Mills, *Nonlinear optics: basic concepts*, 2nd ed. (Springer, New York, 1998).

[18] C. McGowan, D. T. Reid, Z. E. Penman, M. Ebrahimzadeh, W. Sibbett, and D. H. Jundt, "Femtosecond optical parametric oscillator based on periodically poled lithium niobate," Journal of the Optical Society of America B-Optical Physics **15**(2), 694–701 (1998).

[19] W. S. Pelouch, P. E. Powers, and C. L. Tang, "Ti-Sapphire-Pumped, High-Repetition-Rate Femtosecond Optical Parametric Oscillator," Optics Letters **17**(15), 1070–1072 (1992).

[20] D. C. Edelstein, E. S. Wachman, and C. L. Tang, "Broadly Tunable High Repetition Rate Femtosecond Optical Parametric Oscillator," Appl. Phys. Lett. **54**(18), 1728–1730 (1989).

[21] S. Guha, "Focusing dependence of the efficiency of a singly resonant optical parametric oscillator," Appl. Phys. B **66**(6), 663–675 (1998).

[22] M. V. O'Connor, M. A. Watson, D. P. Shepherd, and D. C. Hanna, "Use of a birefringent filter for tuning a synchronously pumped optical parametric oscillator," Appl. Phys. B **79**(1), 15–23 (2004).

[23] J. Prawiharjo, H. S. S. Hung, D. C. Hanna, and D. P. Shepherd, "Theoretical and numerical investigations of parametric transfer via difference-frequency generation for indirect mid-infrared pulse shaping," J. Opt. Soc. Am. B: Opt. Phys. **24**(4), 895–905 (2007).

[24] G. P. Agrawal, *Nonlinear fiber optics*, Optics and photonics, 3rd ed. (Academic Press, San Diego, 2001).

[25] H. S. Tan, W. S. Warren, and E. Schreiber, "Generation and amplification of ultrashort shaped pulses in the visible by a two-stage noncollinear optical parametric process," Opt. Lett. **26**(22), 1812–1814 (2001).

[26] H. S. Tan, E. Schreiber, and W. S. Warren, "High-resolution indirect pulse shaping by parametric transfer," Opt. Lett. **27**(6), 439–441 (2002).

[27] H. S. Tan and W. S. Warren, "Mid infrared pulse shaping by optical parametric amplification and its application to optical free induction decay measurement," Opt. Express **11**(9), 1021–1028 (2003).

[28] F. Eickemeyer, R. A. Kaindl, M. Woerner, T. Elsaesser, and A. M. Weiner, "Controlled shaping of ultrafast electric field transients in the mid-infrared spectral range," Opt. Lett. **25**(19), 1472–1474 (2000).

[29] T. Witte, D. Zeidler, D. Proch, K. L. Kompa, and M. Motzkus, "Programmable amplitude- and phase-modulated femtosecond laser pulses in the mid-infrared," Opt. Lett. **27**(2), 131–133 (2002).

Chapter 3

Pulse Shaping

3.1 Pulse Shaping

The purpose of this section is to examine the pulse shaping apparatus and the theory behind it. This research uses a zero dispersion pulse-shaper with a liquid crystal spatial light modulator. The arrangement used is common in the field of pulse shaping [1]. However, it is often used to shape pulses which have a far larger spectral bandwidth than the one used in this research. This results in some careful design considerations, most originating from resolution criteria, as shall be discussed later.

The zero dispersion pulse-shaper is not a perfect device, it not only shapes the temporal aspect of the pulse but also, to some extent, the spatial profile. This manifests itself as degradation in the M^2 of the beam. This is an important consideration as the pulses from the shaper are used to pump an optical parametric oscillator (OPO). For efficient use, OPOs generally require a highly coherent pump beam, with good spatial properties.

There are different mathematical treatments for the pulse shaping apparatus. The most common procedure [1] assumes that the pulse can be decomposed into its temporal and spatial characteristics. It then ignores the spatial part of the pulse and concentrates on the effects of the pulse-shaper on the temporal profile. This treatment is referred to as the temporal theory. Although intuitive this procedure has the unfortunate side effect of not being able to predict the space-time coupling that the pulse shaper introduces. The space-time coupling causes behaviour that

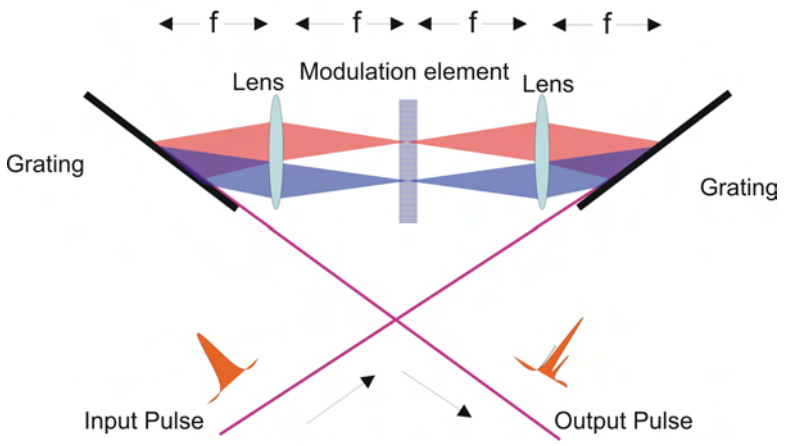

FIGURE 3.1: Schematic of a zero-dispersion pulse shaper

the temporal theory is unable to explain. Nevertheless, the temporal theory is useful as a good approximation to describing the nature of the pulse-shaper and is often used in literature [2, 3].

This section first describes some basic characteristics of the pulse-shaper without going into any detailed mathematics. These characteristics can be intuitively deduced by observing the components used within the shaper. Then the temporal theory is briefly explained, this illuminates some important points that can not be grasped by the previous analysis. Finally, the general theory of pulse shaping is explored. This theory does not decouple the spatial profile of the pulse, and this theory reveals the space-time coupling of the pulse-shaper and some more points to consider in designing experiments utilising this device.

3.2 The Pulse-Shaper

The pulse-shaper used in our research consists of a one-to-one telescope arrangement arranged between two diffraction gratings, as shown in figure 3.1. Both lenses have the same focal length. The distance between the lens and grating is equal to one focal length of the lens. Hence, the total length of the shaper is four times the focal length of the lens. An input laser pulse is first angularly dispersed by the first grating according to its wavelength. The first lens performs a transformation of the angular dispersion of the beam, to a spatial position at the focal plane of the lens. A liquid crystal spatial light modulator (SLM) is placed at this location. The SLM consists of 128 discrete pixels, which are capable of phase-only retardation

of light. The other half of the setup is symmetric to the first and performs the inverse process. A pulse leaving the setup has its temporal profile altered due to manipulation of its spectral phase. Full control of the pulse's temporal behaviour requires the ability to manipulate the spectral amplitude as well as the phase. However, in common with previous authors, this research concentrates on phase only modulation as this still allows a great variety of pulse shapes to be formed and is sufficient for the purposes of this project.

Certain behaviour of the pulse-shaper can be predicted without going into any specific details. It can be noted that the pulse-shaping apparatus is a linear optical system with standard optical components. It can be analysed using ray tracing and simple geometry to intuitively understand its behaviour. The optical components used in the shaper (grating and lenses) have well known properties, which are examined in order to determine their effect on the pulse shaping process.

The first component to encounter the laser pulse is a diffraction grating. This angularly disperses the wavelength components of the pulse according to the following equation, called the grating equation [4]:

$$m\lambda = d(\sin\theta_i + \sin\theta_d) \tag{3.1}$$

where m is the diffraction order (here we shall only be interested in the first order, $m = 1$), d is the groove period, and θ_i, θ_d are the angles incident to the diffraction grating and diffracted from the grating, respectively. The SLM consists of pixels that all have the same width. Hence, it is desirable that the light incident on the SLM has a linear spread of wavelengths across it, so each pixel has the same bandwidth of light passing through it. However, the angular spread of different wavelengths is not linear. This can be seen by differentiating 3.1 with respect to λ

$$\frac{d\theta_d(\lambda)}{d\lambda} = \frac{1}{d\cos\theta_d(\lambda)} \tag{3.2}$$

Which shows a cosine dependence for the dispersion. Analysis of this problem have been performed by Wefers and Nelson [5] to show this is only a limiting issue for pulses that have very large bandwidths, corresponding to time-bandwidth-limited pulses of 20 fs in duration [5], or 80 nm of spectral bandwidth in the near infrared. The pulses used in the experiments have a significantly smaller bandwidth than this, so this effect can be ignored.

A very real issue regarding the grating is its resolving power R. The resolving power is described as the smallest difference between two wavelengths that a grating can accurately distinguish, and is set by the Rayleigh criterion. The resolving power has the elementary mathematical form of [4]:

$$R = \frac{\lambda_0}{\Delta\lambda_R} = mN \tag{3.3}$$

where $\Delta\lambda_R$ is the smallest difference between two wavelength components of equal magnitude, λ_0 is the central wavelength, and N is the total number of lines illuminated on the grating. As can be seen from eqn 3.3, the resolving power is directly proportional to the number of lines illuminated on the grating. For a small number of illuminated lines the spectral resolution of the grating is low and fine features in the spectrum are not resolved at the position of the SLM. One important property of the zero dispersion pulse-shaper is that for no applied phase profile across the SLM, the pulse leaving the shaper should be identical to the one that entered. Clearly this condition is not met if the gratings do not faithfully transfer the spectral profile of the pulse. Furthermore, if this condition is not met, alignment of the shaper becomes problematic; this is discussed in more detail in the experimental chapters.

It is intuitive to want the highest grating resolution in order to allow for good spectral resolution. However, this is impractical, as it would mean illuminating an infinite number of lines. A practical limit on the resolving power must be initiated. One consideration is due to the spectrum of the incoming pulse. For a complicated spectrum (such as in our case) it is important that all the features are resolved. Shannon's sampling theorem [6, 7] can be used to show that the resolving power of the grating need only be high enough to distinguish between the finest features in the spectrum. This is not the only criteria that must be obeyed. A more demanding criterion on R is placed by the SLM, such that the lower limit on the resolving power should be such that each pixel within the SLM should modulate a unique wavelength, otherwise the full potential of the device is not realised. This requirement requires that $\Delta\lambda_R = \Delta\lambda/n$, where $\Delta\lambda$ is the spectral bandwidth of the pulse and n is the number of pixels in the SLM ($n = 128$ for our device). This requirement gives an unintuitive (but necessary) resolving criterion for pulses with different spectral bandwidths, in that smaller bandwidth pulses require more lines of a grating to be illuminated than broad bandwidth pulses. Furthermore, the spectrum for our pulse is not Gaussian or a smooth spectrum (as used by many

authors in the field of pulse shaping) but is instead one that has many peaks and troughs. This means the resolving power of the gratings required is higher than that used in the experiments of other authors.

Weiner [3] has considered the issue of a diffraction grating inside a pulse-shaper and determined its effect on the output pulses. He has found that the grating puts a fundamental limit on the complexity of the output pulse, irrespective of the modulating element at the Fourier plane [3]. The measure of the complexity of the shaped pulse can be characterised by the parameter η, where η represents the distinct number of temporal features that can be realised in the outgoing pulse; or equivalently the number of spectral features that may be placed inside the bandwidth of the pulse. It is defined as [3]:

$$\eta = \frac{\Delta t}{\delta t} = \frac{\Delta \nu}{\delta f} \tag{3.4}$$

Where $\Delta\nu$ represents the total frequency bandwidth of the pulse, Δt represents the maximum temporal window within which pulse shaping can arise and is set by the fundamental characteristics of the pulse-shaper [3]; δt and δf are the shortest temporal and finest spectral feature which can be realised in the outgoing pulse. Weiner shows that η can be calculated using the following formula:

$$\eta = \frac{\Delta\lambda}{\lambda_0} \frac{\pi}{(\ln 2)^{1/2}} \frac{w_{in}}{d\cos(\theta_{in})} \tag{3.5}$$

where w_{in} is the input beam spot-size (measured as the radius of the beam, where the intensity falls to $1/e^2$ of its maximum value). For typical pulse-shaping apparatus, η has a value in the range of a few hundred [3]. As can be seen from equation 3.5 the complexity parameter can be most easily increased by illuminating as much of the diffraction grating as possible, this can be achieved by placing a telescope arrangement before the diffraction grating, such that the width of the beam is maximised to cover as much of the grating surface as possible.

Expanding the incident beam before the shaper also has another desirable effect, that of achieving a small focused spot-size at the Fourier plane. It is clear that the use of a lens in the shaper results in the individual wavelengths diffracted from the grating being focused to a certain spot-sizes at the Fourier plane. For efficient use of the SLM the focused spot-size should be less than the width of the SLM pixel. Otherwise each pixel does not modulate a unique wavelength and this results in a reduction in the range of temporal shapes that are produced. The spot-size of

each wavelength component due to a lens of focal length f can be calculated using the well known result of focusing a Gaussian beam [8]:

$$w_0 \approx \frac{f\lambda}{\pi w(f)} \tag{3.6}$$

where λ is the wavelength of light we are interested in, w_0 is the spot-size of that wavelength component at the focus of the lens, and $w(f)$ is the spot-size at the lens. However, care must be taken to avoid quartic-phase-aberration [9], which degrades the quality of the beam. This type of aberration is most pronounced by having a high f-number ($f^{\#} = f/2w(f)$), that is for having a large beam width passing through a short focal length lens.

Finally, chromatic dispersion of the lens should be considered. The focal length of the lens is specified for a given wavelength. But the beam impinging on the lens consists of a range of wavelengths. Due to chromatic dispersion each wavelength is focused at a slightly different distance from its neighbouring wavelength. Since the spectral bandwidth of light used in the research is relatively small, the range of focusing is not expected to be significantly different from the expected focal length of the lens. If the shaped pulses had bandwidths greater than a few tens of nanometers, then chromatic dispersion would be significant and the lenses should be replaced with mirrors, which do not suffer from chromatic dispersion.

3.3 Temporal Mathematical Treatment

As described in the introduction the pulse-shaper manipulates the spectral components of the pulse in order to manipulate its temporal properties. Intuitively the process can be described as performing a Fourier transformation of the pulse from its time domain to the frequency domain; then adding a phase and/or amplitude pattern across its spectrum, then performing the inverse Fourier transformation in order to recover the temporal pulse. The mathematical treatment of the pulse-shaper reflects this procedure. In the time domain the problem can be summarised as:

$$e_{out}(t) = e_{in}(t) \otimes h(t) = \int e_{in}(t')h(t-t')dt' \tag{3.7}$$

Where $e_{in}(t)$ and $e_{out}(t)$ are the temporal electric field profiles of the pulse before and after entering the pulse-shaper respectively and $h(t)$ is called the impulse

response function, and describe the effects of the pulse-shaper on the electric field. The expression is a convolution (signified by $\otimes$) between the input electric field and the impulse response function. Equation 3.7 can be Fourier transformed to give:

$$E_{out}(\omega) = E_{in}(\omega)H(\omega) \tag{3.8}$$

Where $E_{in}$and E_{out} are the respective Fourier transforms of the electric fields travelling into and leaving the apparatus. $H(\omega)$ is the complex frequency response of the system. Equation 3.8 is a general result that can be used as a starting position to analyse many different types of pulse shaping equipment. The mathematical treatment for our type of pulse-shaper has been well examined in the literature [3]. It is not the purpose of this section to present new theories of pulse shaping or add to the existing literature. Existing pulse shaping theories is presented with the aim of understanding the processes and consequences arising from the pulse shaping apparatus.

Much of the early mathematical treatment for the pulse shaping apparatus can be traced back to various groups associated with the research departments of AT&T. The earliest mathematical analysis of the setup can be traced back to Martinez [10, 11]. The apparatus was intended to temporally compress and stretch pulses by displacing the last grating in the setup, it was in order to understand this process that Martinez performed the analysis. Weiner et. al. [1] used this work and the work conducted by Thurston et. al. [12] to understand arbitrary pulse shaping of the apparatus using a liquid crystal modulator. The analysis described by Weiner [1] is briefly presented here in order to understand some consequences of the shaping process. As mentioned before, it ignores the space-time coupling that the shaper introduces, but its simplicity makes it a good starting point to understand the more complicated treatment.

The analysis starts with the assumption that the input beam can be separated into its temporal and spatial components, where the spatial profile is assumed to be Gaussian:

$$e_{in}(x,t) = e_{in}(t)e^{(-x^2/w_{in}^2)} \tag{3.9}$$

Here w_{in} is the spot-size of the incoming beam. Equation 3.8 indicates that it is easier to perform the analysis in the frequency domain than the time domain. A

Fourier transformation is performed to convert 3.9 into the frequency domain:

$$E_{in}(x,\omega) = E_{in}(\omega)e^{(-x^2/w_{in}^2)} \tag{3.10}$$

Martinez gives an equation to describe the angular dispersion of a pulse from a diffraction grating [11]. This operator and that for the transformation of the pulse by a lens is applied to the pulse. Finally, the pulse is multiplied by a function to describe the mask $M(x)$ at the Fourier plane. The equation immediately after the mask is given by:

$$E_m(x,\omega) \sim E_{in}(\omega)e^{-(x-\alpha\omega)^2/w_0^2}M(x) \tag{3.11}$$

Where α represents the spatial dispersion and w_0 is the focused Gaussian beam radius at the masking plane for a single frequency component. In order to describe phase and amplitude modulation the masking function $M(x)$ is generally a complex quantity. The formulae for α and w_0 are as follows:

$$\alpha = \frac{\lambda^2 f}{2\pi c d\cos(\theta_d)} \tag{3.12}$$

$$w_0 = \frac{\cos(\theta_{in})}{\cos(\theta_d)}\left(\frac{f\lambda}{\pi w_{in}}\right) \tag{3.13}$$

Where the variables c represents the speed of light in a vacuum, f is the focal length of the lens, d is the grating period, and θ_{in} and θ_d are the input angles to the diffraction grating, normal to its surface, and diffracted angle, respectively.

It can be seen that eqn 3.11 is a non-separable function of both space and frequency. All that remains is to transform equation 3.11 through another lens and grating in order to derive the output pulse. However, in many applications only the temporal profile is required and a spatial profile similar to that which entered the pulse-shaper. In order to recover the spatial profile of the input beam a spatial filtering is performed. Physically this operation can be performed if the light after the shaper is passed through a single mode optical fiber of sufficient length so as to act as a spatial filter, typically achieved with as little as a few centimeters of fibre. However, care must be taken to choose a suitable fibre such that it does not introduce any nonlinear behaviour which could alter the shaped pulse in an unfavourable manner. Alternatively the light could be focused through the aperture of a pin hole such that higher order transverse modes are not transmitted. Weiner et. al. show that using this approximation the equation for the pulse spectrum after the shaper is independent of spatial co-ordinates (except for a

multiplicative factor), and $H(\omega)$ in equation 3.8 is then given by:

$$H(\omega) = \left(\frac{2}{\pi w_0^2}\right)^{\frac{1}{2}} \int dx M(x) e^{-2(x-\alpha\omega)^2/w_0^2} \tag{3.14a}$$

The important implication of equation 3.14a is that the frequency filter is not solely given by the mask function, but by the mask function convolved with the spatial intensity profile of the beam. This limits the full width at half maximum (FWHM) spectral resolution $\delta\omega$ of the pulse-shaper to $\delta\omega \equiv (\ln 2)^{1/2} w_0/\alpha$. and thus limits the finest features which can be transferred onto the filtered spectrum.

The last stage in this analysis is to Fourier transform 3.14 to reveal some aspects related to the temporal profile. It can be shown that 3.14a can be transformed into:

$$h(t) = m(t)g(t) \tag{3.15}$$

where

$$m(t) = \frac{1}{2\pi} \int d\omega M(\alpha\omega) e^{i\omega t} \tag{3.16}$$

and

$$g(t) = \exp(-w_0^2 t^2/8\alpha^2) \tag{3.17}$$

The equations show that $g(t)$ restricts the temporal range over which the shaping of the pulse reflects the response of the mask. The FWHM of $g(t)$ is called the time window Δt. It has been previously encountered in equation 3.4 and is given by:

$$\Delta t = \frac{4\alpha\sqrt{\ln 2}}{w_0} \tag{3.18}$$

The time window for typical pulse shaping parameters is usually in the pico- to tens of picosecond range. The desirable shaped pulses for this research are considerably less than this.

3.4 Spatio-Temporal Effects

The analysis above is restricted by the requirement to perform a spatial filtering after the shaper in order to recover the fundamental Gaussian beam. However, the loss of power this entails may not be practically desirable. It is therefore important to be aware of any effects arising from not performing the spatial filtering.

The space-time analysis of pulse-shapers was first performed by Danailov et. al. [13]. This analysis was further elucidated by Wefers and Nelson [14]. Wefers et. al. analysis reveals a simple equation to describe the output pulse. In this analysis the incoming pulse is not separated into temporal and spatial components, the analysis uses two general mathematical operations on an arbitrary pulse equation. These operations are: the transformation of the pulse equation by a grating (as given by Martinez [11]), and the transformation of a pulse equation at the focal plane of the lens. There is one more general operator that they use for analysis purposes, but it is not needed for the case of a perfectly aligned shaper. This operator describes the free space propagation of an arbitrary pulse equation.

Using the slowly varying envelope approximation the carrier frequency of the pulse equation separable from its envelope function, as shown by:

$$e_1(x,t) = e_{in}(x,t)e^{i\omega_0 t} \tag{3.19}$$

Where $e_{in}(x,t)$ is the envelope function of the pulse in space and time, ω_0 is the temporal angular carrier frequency of the pulse. The derivation of the final equation is elegantly performed and described in their paper [14]. But the final result is simply quoted, this shows that the spectrum of the output pulse, in terms of the double Fourier transformation of time (t) into angular frequency (ω) and position (x) into wavevector (k), is given by the output pulse $E_{out}(k,\omega)$ in terms of the input pulse $E_{in}(k,\omega)$ via the relationship:

$$E_{out}(k,\omega) = E_{in}(-k,\Omega)G(k,\Omega) \tag{3.20}$$

Where $\Omega = \omega - \omega_0$, ω_0 is the angular carrier frequency, and $G(k,\Omega)$ is the impulse function, given by the expression:

$$G(k,\Omega) = m(-\lambda_0 f[\gamma\omega + \beta k]/2\pi) \tag{3.21}$$

Where $\beta = \cos(\theta_{in})/\cos(\theta_d)$, $\gamma = \lambda_0/cd\cos(\theta_d)$ and $m(x)$ is the masking function. Equation 3.21 shows that the masking function shapes both the spectrum of the pulse and its spatial wavevector. The degree to which it shapes the frequency over the spatial wavevector is given by the ratio γ/β. For the case of $\gamma/\beta \to 0$ the apparatus performs purely spatial shaping and for the opposite case $\gamma/\beta \to \infty$ the shaper performs purely temporal shaping. The parameter γ/β can be expressed

as:

$$\gamma/\beta = \lambda_0/(cd\cos(\theta_i)) \tag{3.22}$$

Hence, the ratio is totally governed by angular dispersion of the grating. Wefers and Nelson show that for a typical pulse-shaper there is an inherent pulse tilt on the outgoing pulse, irrespective of the modulating profile put onto the SLM. This inherent pulse tilt is given by the parameter β/γ and is quoted in millimeters per picosecond. Ideally γ/β should be maximised so that there is no spatial shaping of the beam, and therefore no degradation in the beam's M^2. This means using a grating with a small grating period and at an incident angle far away from the normal to the grating (ideally almost parallel to the grating surface). Due to the space-time coupling, it is also important that the spatial profile of the pulse which enters the shaper be free from any structure; as this will be coupled into the outgoing temporal pulse.

3.5 An Adaptively Controlled Spatial Light Modulator

The mid-IR pulse shaping system developed in this thesis makes use of a computer controlled feedback loop. This allows a computer to receive feedback from an experiment (often via a photodiode or oscilloscope), and use it to choose an appropriate phase profile to apply to the SLM, record the result, and repeat the above procedure until a satisfactory outcome has been reached.

In practise the setup looks like that shown schematically in chapter one, figure 1.6. The computer system consists of a search algorithm, computer routines to collect data from a data acquisition card (DAQ), and routines to send and receive data over a general purpose interface bus (GPIB). The spatial light modulator (SLM) is connected to the GPIB. The DAQ card can have a number of instruments connected to it. An oscilloscope is connected to the GPIB for data collection purposes.

The key to this system is the search algorithm, which chooses the phase profiles put to the hardware. Two search algorithms have been investigated. A publicly available genetic algorithm (GA) called GALib, and a proprietary built simulated annealing (SA) algorithm, which was developed based on work conducted

by Lester Ingber [15, 16]. These two algorithms were chosen as examples of two broad categories of global optimisation algorithms, with the aim of comparing their performance. There are other search algorithms which could have been employed but that was beyond the scope of this research. The computer code for all components was written in object orientated ANSI C++. The use of object orientated programming and one computer language allowed ease in transferring data between different modules within the code.

This section describes some basic principles of the SLM and the type of phase profiles put to the hardware. It then investigates some general advice regarding search algorithms.

3.5.1 Liquid Crystal Spatial Light Modulator

The spatial light modulator (SLM) used in this research is manufactured by Cambridge Research Instrumentation (CRI) and the model is MIR-PHS. The device is capable of phase-only modulation of light and is designed for laser pulses with wavelengths between 900 and 1620 nm. The device consists of a single row of 128 individually addressable pixels, with one large "calibration pixel" at the end of this row. This pixel is used to determine the response of the liquid crystal with different drive voltages. The pixels are computer controlled via GPIB. Each pixel has a width of 97 μm, height of 2 mm, and a dead region between pixels of 3 μm. The device is the same model as used by several previous authors [2, 14]

The LC SLM consists of a thin layer of zero-twist nematic liquid crystals sandwiched between glass covers. These glass covers have microscopically etched parallel valleys on the inside, and are coated with transparent electrodes. The liquid crystals are long rod like molecules. In the absence of an electric field this allows the crystals to align themselves parallel to the surface of the etched glass covers. By applying a voltage across the electrodes the molecules align themselves to the electric field. Light that is polarised parallel to the liquid crystals therefore experiences a change in refractive index (see fig 3.2). The liquid crystals are contained within small cells (called pixels) which are aligned in a linear array.

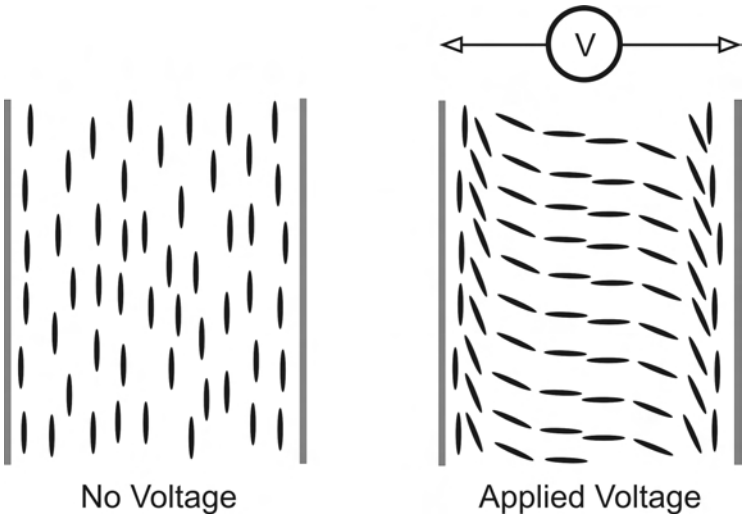

FIGURE 3.2: Schematic of liquid crystal orientation with and without an applied voltage to the electrodes

The retardation of light of wavelength λ passing through a LC cell of thickness l is given by the following equation

$$\Delta\phi = \frac{2\pi\Delta n(V)l}{\lambda} \tag{3.23}$$

Where $\Delta n(V)$ is the change in refractive index of the material with voltage. The voltage can be varied continuously but, due to the digital nature of computer control, is in fact varied digitally. The voltage across the cell can take one of 4096 different states ("12 bit"), which allows grey-scale control of the retardation.

3.5.2 Basics of a Search Algorithm

Part of the purpose of this research is to demonstrate computer control of the laser pulse-shape. There are numerous search algorithms that could have been used. This research does not determine which is the best algorithm. This question depends entirely on the problem being solved since some algorithms perform better with certain problems, and others perform better with a different class of problem. This phenomenon extends to all search algorithms used in any situation. Within the field of computational heuristics this problem is expressed by Koppen, Wolpert and Macready as the "no free lunch theorem" [17]. The theorem shows mathematically that any two algorithms are equivalent when their performance is averaged across an infinite number of problems. That is to say, for the right

sort of problems, even a simple hill climbing algorithm can outperform the most "advanced" search algorithm. Therefore, the notion of a "one size fits all" search algorithm must be dimissed. As a result, this research assesses the performance of two search algorithms, which are representative of two broad categories of global optimisation algorithms, under our particular experimental conditions. The key to a good search algorithm lies in tailoring it to the problem at hand. With the aid of insight one should aim to reduce the use of a global search algorithm to that of a local optimisation routine, or ideally a non-iterative routine.

It is with this spirit that an explanation of the sort of functions the search algorithms will be optimising is explained, and some basic considerations for a good search algorithm investigated. The algorithm should be grounded to the physical problem being solved. To do this it is important to consider the SLM and the type of phase-profiles it can produce. It is also important to consider some general analysis of search algorithms. It can be noted that all search algorithms have three universal considerations for optimum convergence, these are: the "sensitivity" of the search-space, the size of the search space, and multiple solutions within the search space.

Ideally the search space should be continuous and smoothly varying, so as to always provide the algorithm with a strong feedback on its performance. The worst case scenario is one in which the search space is simply a delta function of one set of variables. In this case even the best tailored algorithm would be no better than a random search. The search space for any problem investigated with our apparatus is dependent on the types of phase profiles the SLM can produce. To gauge the size of the SLM search space it can note that there are 128 pixels in the SLM, and each pixel can have one of 4096 values. Placing these numbers into the formula for permutations with replacement, it can be shown that there are 10^{462} possibilities. This is a very large number and it is unlikely that the apparatus will find the optimum phase profile by merely allowing it to try all possible permutations. There is also another reason for not allowing all possible permutations of the search space to be used. This reason is grounded in the physics of the SLM and pulse-shaper. Sardesai et. al. [2] found that a pulse shaper performs spectral phase-to-amplitude modulation for phase features in the mask which vary rapidly compared to the spot-size of a single wavelength component at the Fourier plane. This phenomenon occurs because the spectrum presented at the SLM is in fact continuous and so sudden jumps in phase from one pixel to another inevitably

lead to light being diffracted out of the beam. The concept of a spot size for a single wavelength component is really related to the resolution of the pulse shaper without the pixellated SLM. If this spot size is less than the pixel size then the resolution of the overall system is set by the SLM pixellation and the degree of amplitude modulation is small. For this reason, the phase profiles are restricted to smoothly varying curves and thus unwanted amplitude modulation is avoided.

Most of the problems encountered in this research involve dispersion compensation for the SPM-chirped output from a fibre. The dominant dispersion in the fibre is caused by GVD, then by third order dispersion (TOD) and successively higher order dispersion. By examining the phase distortion that these dispersion types cause it can see that GVD causes a parabolic phase profile to occur across the spectrum of the pulse, TOD causes a cubic phase profile, and higher order dispersion terms correspond to higher order monomials. A possible strategy for dispersion compensation consists of cancelling out these terms by applying a polynomial phase profile across the spectrum. This concept also arises naturally by taking a Taylor series expansion of an arbitrary phase-profile $\phi_{slm}(\omega)$:

$$\begin{aligned}\phi_{slm}(\omega) \quad = \phi_{slm}(\omega_0) \quad &+\frac{\phi^{(1)}_{slm}(\omega_0)}{1!}(\omega-\omega_0)+\frac{\phi^{(2)}_{slm}(\omega_0)}{2!}(\omega-\omega_0)^2 \\ &+\frac{\phi^{(3)}_{slm}(\omega_0)}{3!}(\omega-\omega_0)^3+\sum_{n=4}^{\infty}\frac{\phi^{(n)}_{slm}(\omega)}{n!}(\omega-\omega_0)^n \quad (3.24)\end{aligned}$$

where $n!$ is the factorial of n and $\phi^{(n)}_{slm}(\omega_0)$ denotes the nth derivative of $\phi_{slm}(\omega)$ at the point ω_0. The Taylor series expansion can continue indefinitely to replicate faithfully the real profile. But for the problems proposed in this dissertation only the first few terms are required.

For the case of a short pulse travelling through a material it can be noted that the derivatives in the Taylor series correspond to ever increasing orders of dispersion. Within this framework GVD corresponds to the value obtained from $\phi^{(2)}_{slm}(\omega_0)$ and TOD corresponds to $\phi^{(3)}_{slm}(\omega_0)$. A special note about the first two terms in the expansion can be made: they can be neglected because they do not change the shape of the pulse. The first term in the expansion corresponds to a constant phase across the spectrum, which in the time domain merely shifts the whole carrier-wave envelope. Since the SLM is capable of retarding light by only a few optical cycles this shift in the carrier-wave envelope is negligible compared to the duration of the pulse [18]. The second term corresponds to temporal displacement of the

whole pulse, again this does not change the temporal profile of the pulse and is therefore irrelevant for our purpose [18]. Successively higher order terms can be observed, but for phase profiles caused by dispersion in a material, higher order terms become appreciatively smaller. For situations envisaged, such as propagation of a picosecond pulse through an optical fiber, fourth order dispersion only becomes appreciable for fiber lengths that are many kilometers in length. Hence, for short lengths of fiber it is certainly sufficient to model the dispersion up to the fourth order dispersion. The phase equation can therefore be written as:

$$\phi_{slm}(\omega) = \alpha_2(\omega - \omega_0)^2 + \alpha_3(\omega - \omega_0)^3 + \alpha_4(\omega - \omega_0)^4 \tag{3.25}$$

Where α_2 denotes GVD, α_3 represents TOD, and α_4 symbolises FOD. Therefore, the purpose of any search algorithm used here is to optimise these coefficients, which will therefore optimise or manipulate the experiment. This very procedure has been used by several authors in experiments regarding dispersion compensation [19–22].

3.6 Conclusion

The design of the pulse shaping apparatus requires some thought since many of the design parameters are coupled together. Therefore, a balance must be met in order to find the best compromise. In chapter four these design considerations are made explicit for our experimental setup.

It is clear from the full spatio-temporal treatment of the pulse shaper that the pulses leaving the shaper have a degree of pulse- front tilt and this results in a degradation of the beam quality. However, it is hoped that the OPO can perform a spatial filtering of the beam, and the pulse-front tilt may not affect control of the idler pulse.

A search algorithm has been chosen so that it is capable of efficiently compensating for dispersion caused by propagation of a pulse through a length of fibre. However, the model is not limited to dispersion compensation; it is also used for adaptive control of pulses in the mid-infrared. In general the use of a Taylor series expansion of the phase profile is a useful method for reducing the total number of parameters that the search algorithm will have to optimise.

3.7 References

[1] A. M. Weiner, "Femtosecond Optical Pulse Shaping and Processing," Prog. Quant. Electron. **19**(3), 161–237 (1995).

[2] H. P. Sardesai, C. C. Chang, and A. M. Weiner, "A femtosecond code-division multiple-access communication system test bed," J. Lightwave Technol. **16**(11), 1953–1964 (1998).

[3] A. M. Weiner, "Femtosecond pulse shaping using spatial light modulators," Rev. Sci. Instrum. **71**(5), 1929–1960 (2000).

[4] C. Palmer, *Diffraction Grating Handbook* (Newport Corporation, London, 2005).

[5] M. M. Wefers and K. A. Nelson, "Programmable Phase and Amplitude Femtosecond Pulse Shaping," Opt. Lett. **18**(23), 2032–2034 (1993).

[6] M. Dodson, "Shannon Sampling Theorem," Current Science **63**(5), 253–260 (1992).

[7] A. J. Jerri, "Shannon Sampling Theorem - Its Various Extensions and Applications - Tutorial Review," Proceedings of the IEEE **65**(11), 1565–1596 (1977).

[8] O. Svelto and D. C. Hanna, *Principles of lasers*, 4th ed. (Plenum Press, New York, 1998).

[9] A. E. Siegman, "Analysis of Laser-Beam Quality Degradation Caused by Quartic Phase Aberrations," Appl. Opt. **32**(30), 5893–5901 (1993).

[10] O. E. Martinez, "3000 Times Grating Compressor with Positive Group-Velocity Dispersion - Application to Fiber Compensation in 1.3-1.6 Mu-M Region," IEEE J. Quantum Electron. **23**(1), 59–64 (1987).

[11] O. E. Martinez, "Grating and Prism Compressors in the Case of Finite Beam Size," J. Opt. Soc. Am. B: Opt. Phys. **3**(7), 929–934 (1986).

[12] R. N. Thurston, J. P. Heritage, A. M. Weiner, and W. J. Tomlinson, "Analysis of Picosecond Pulse Shape Synthesis by Spectral Masking in a Grating Pulse Compressor," IEEE J. Quantum Electron. **22**(5), 682–696 (1986).

[13] M. B. Danailov and I. P. Christov, "Time-Space Shaping of Light-Pulses by Fourier Optical-Processing," J. Mod. Optic. **36**(6), 725–731 (1989).

[14] M. M. Wefers and K. A. Nelson, "Space-time profiles of shaped ultrafast optical waveforms," IEEE J. Quantum Electron. **32**(1), 161–172 (1996).

[15] L. Ingber, "Simulated Annealing - Practice Versus Theory," Mathematical and Computer Modelling **18**(11), 29–57 (1993).

[16] L. Ingber, "Very Fast Simulated Re-Annealing," Mathematical and Computer Modelling **12**(8), 967–973 (1989).

[17] M. Koppen, D. H. Wolpert, and W. G. Macready, "Remarks on a recent paper on the " No free lunch " theorems," IEEE Trans. Evol. Comput. **5**(3), 295–296 (2001).

[18] R. Trebino, *Frequency-resolved optical gating: the measurement of ultrashort laser pulses* (Kluwer Academic Publishers, Boston, 2000).

[19] A. Efimov, M. D. Moores, B. Mei, J. L. Krause, C. W. Siders, and D. H. Reitze, "Minimization of dispersion in an ultrafast chirped pulse amplifier using adaptive learning," Appl. Phys. B **70**, S133–S141 (2000).

[20] A. Efimov and D. H. Reitze, "Programmable dispersion compensation and pulse shaping in a 26-fs chirped-pulse amplifier," Opt. Lett. **23**(20), 1612–1614 (1998).

[21] F. G. Omenetto, J. W. Nicholson, B. P. Luce, D. Yarotski, and A. J. Taylor, "Shaping, propagation and characterization of ultrafast pulses in optical fibers," Appl. Phys. B **70**, S143–S148 (2000).

[22] F. G. Omenetto, D. H. Reitze, B. P. Luce, M. D. Moores, and A. J. Taylor, "Adaptive control methods for ultrafast pulse propagation in optical fibers," IEEE J. Sel. Topics. Quantum Electron. **8**(3), 690–698 (2002).

Chapter 4

Experimental Apparatus

This chapter describes the experimental setup used throughout the research. The components are discussed in the following order: the laser source, mid-infrared diagnostics, the optical parametric oscillator, spatial light modulator, pulse shaper, and search algorithms.

4.1 Laser Source

Our initial laser source is a commercial diode-pumped Nd:YLF laser (Microlase DPM-1000-120). The laser produces a continuous train of approximately $4\,ps$, bandwidth-limited pulses, at a central wavelength of $11047\,nm$, and average powers of $1\,W$. The output from this laser is amplified by a second commercial laser (Q-Peak MPS-1047 CW-10) operating in amplification mode. The average power is increased to $7\,W$ while all other parameters stay the same. The master oscillator power amplifier (MOPA) configuration has the advantage of decoupling the formation of the short pulses from the scaling to high average powers, so that each can be independently optimised. A half-waveplate and polariser is placed soon after the laser source to control the power entering the rest of the setup. This is important, as not all of the power from the laser can be used in our pulse shaping apparatus. This is in part due to the spatial light modulator (SLM), which has a maximum operating power of approximately $1.8\,W$. Slightly increasing the laser power above this value alters the responsiveness of the liquid crystals. This is due to the electric field of the laser pulses interfering with the voltage used to control the orientation of the crystals. Fortunately, this is a non destructive process

and reducing the power levels below the threshold value returns the device to its previous state. However, caution must be taken not to significantly exceed the threshold value, as this causes irreversible thermal damage to the liquid crystals.

The spectral bandwidth leaving the MOPA system is approximately $0.3\,nm$, which is insufficient for pulse shaping into the sub-picosecond regime. To increase the spectrum, the pulses are passed through a short piece ($\sim 55\,cm$) of single-mode polarisation-maintaining fibre (Fibercore HB1000). The pulses undergo self-phase modulation (SPM) which causes the spectrum to broaden [1]. SPM is a $\chi^{(3)}$ process which is dependent on the intensity of the incoming pulses as well as the incoming spectral shape and chirp. It is a well known phenomena and used in many areas of laser physics, such as modelocking of lasers [2, 3].

It is important to use polarisation maintaining (PM) fibre as the high intensity of light inside the fibre may cause nonlinear polarisation rotation (NPR) [1]. This effect is unwanted because it causes the temporal peak of the pulse to be rotated about the optical axis of the fibre more so than the leading and trailing edges of the pulse. Placing a polariser after the fibre it can be seen that, depending on the orientation of the polariser, NPR causes a variable number of multiple pulses to be observed via autocorrelation measurements (Figure 4.1). This can be explained by the central peak being rotated by 3π while the edges of the pulse have remained fairly stationary. Nonlinear polarisation rotation has found advantages in many areas of laser physics, including modelocking of lasers [2, 3]. However, it is undesirable for our purpose since the pulse shaper and OPO are polarisation sensitive. The use of polarisation maintaining fibre can eliminate NPR, and this sort of fibre has been used by previous authors for similar research purposes [4–6].

In order to achieve the correct amount of spectral broadening it is found to be necessary to couple $2.3\,W$ of power into the fibre. It is observed with laser intensities greater than $7 \times 10^{10}\,W/m^2$ the coupling of light into the fibre is abruptly decreased. It is thought this is caused by ablation of material at the coupling end of the fibre. To couple sufficient light, an "end-cap" is used; this is a small piece of fibre that has no core. It is attached to the polarisation maintaining fibre using a fibre fusion splicer (Sumitomo Electric, model: Type-36 or Ericsson FSU 925). Figure 4.2 shows a schematic of the fibre launch system and the end-cap. Light is focused into the fibre through the end-cap. Due to the focusing of the light, the end-cap has a larger surface area illuminated and therefore does not experience any thermal damage. The maximum length of the end-cap, called L_{ec} is calculated

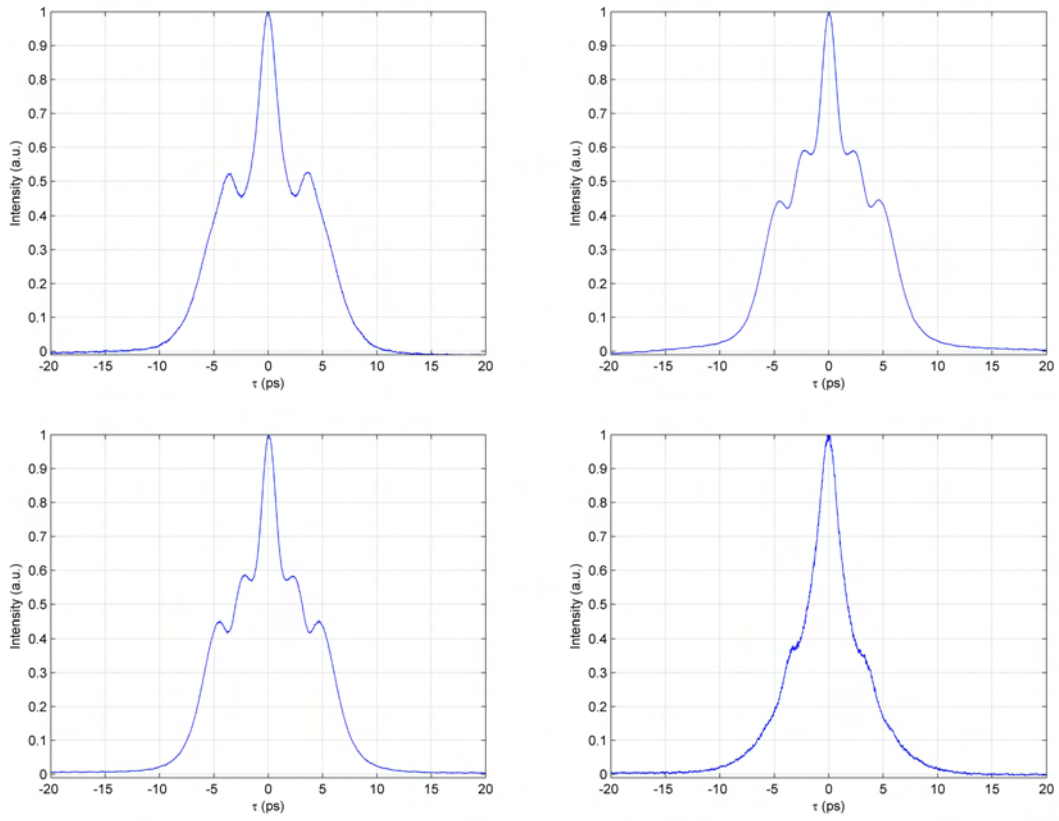

FIGURE 4.1: Nonlinear polarisation rotation of the pulse after the fibre. Figures show the autocorrelation trace as seen after passing through a polariser at different orientation. From the top right going clockwise the orientations of the polariser is 67°, 188°, 310° and 351°.

using the numerical aperture (NA) of the fibre and the radius of the fibre. An end-cap longer than L_{ec} results in clipping of the beam into the fibre. The end cap also has a minimum length associated with it, determined by the minimum area of the fiber end that has to be illuminated in order to avoid ablation. Typical lengths of end-caps used were between 100 and 300 μm, with shorter lengths having better fibre coupling efficiencies. Typical coupling efficiencies for the fibre launch were between 60% and 75%, which is similar to the coupling efficiency seen without the end-cap. For the power levels coupled through the fibre, the polarisation contrast ratio depended on whether the light was polarised parallel to the fast or slow axis of the PM fibre. For low powers (tens of milliwatts) it is irrelevant which axis the light is polarised along. However, for high powers (2.3 W) it was observed that a contrast ratio of typically 8000:1 could be achieved using one polarisation of light. But for light polarised along the other axis the ratio was as low as 12:1. This phenomena could be explained [1] due to the high intensity light inducing a refractive

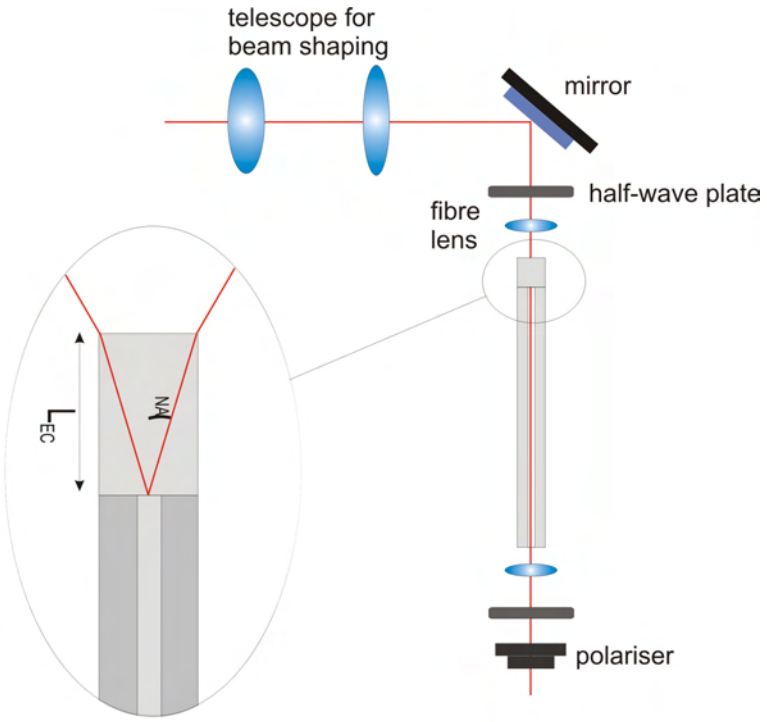

FIGURE 4.2: Schematic of fibre launch system (right) and end-cap (left) attached to the fibre. A spherical telescope arrangement is used to adjust the beam size and divergence before it enters the fibre. The length of the end-cap has to be long enough to increase the surface illuminated by the laser to avoid thermal damage, but short enough so as not to cause the laser beam to "clip". The latter requirement is dependent on the numerical aperture (NA) of the fibre, the end-cap must be shorter than the L_{ec}.

index change in the material. When the input beam is polarised to the slow axis (highest refractive index), the induced nonlinear birefringence of the beam adds to the intrinsic linear birefringence of the fibre, making the fibre more birefringent. But for light polarised to the fast axis the nonlinear induced polarisation does not add constructively and competes with the fibres internal birefringence.

The procedure for aligning the birefringent fibre consists of first coupling the maximum amount of light through the end-cap and fibre, then adjusting the polarisation of light going through the fibre so as to align it with the fibre's optical axis. Each end of the fibre is secured on a fixed mount, and two mirrors are used to reflect the laser light onto the fibre, and parallel to the optics bench. A half-wave-plate is placed before the fibre, however it is only adjusted after the optimal amount of light has been coupled through the fibre. A sensitive InGaAs detector is placed at the other end of the fibre to detect power levels. The light entering the fibre is

maximised by adjusting the two mirrors. At this stage the light entering the fibre is a tiny fraction of the total light available. The purpose of this stage is to ensure that the light entering the fibre is perpendicular to the cleave of the end-cap. The power incident on the fibre is reduced to about $100\,mW$ and a lens of focal length $\sim 6.4\,mm$ is then introduced before the fibre. The focal length is chosen based on the NA of the fibre and the spot-size of the laser beam. The lens is attached to a high precision flexture stage capable of translation in all three directions. The stage was controlled using differential micrometer screw gauges, which have a stated precision of $50\,nm$. Once the maximum amount of light is coupled by adjustments of the lens, final adjustments are made by slightly tilting the mirror just before the fibre and simultaneously making small adjustments to the $6.4\,mm$ lens. At this stage, the light entering the fibre is optimised. If good coupling efficiency can be achieved, then the fibre is retained. Otherwise it is rejected and a new section of polarisation maintaining fibre is cut, and an end-cap is attached. Once adequate coupling is achieved, $2.3\,W$ of light is coupled through the fibre. The spectrum from the fibre is monitored using an optical spectrum analyser and the fibre is progressively cut-back to reduce its length until the required amount of spectral broadening is achieved. After this procedure, the polarisation of light entering the fibre is adjusted.

This is achieved by introducing a polariser at the output end of the fibre and using the half-wave-plate situated before the fibre. A detector is placed soon after the polariser to monitor power levels. The polarisation alignment procedure consists of adjusting the polariser to find the minimum power level recorded on the detector. Then adjusting the half-wave-plate to reduce the power-levels further. The last two procedures are repeated until the minimal amount of light is coupled through the fibre. If the contrast ratio of light coupled through the fibre is less than a 100:1, then the polarisation of the laser is aligned to the fast axis of the fibre. This can be confirmed by reducing the power levels entering the fibre, in which case the contrast ratio increases. To align the polarisation of the laser to the slow axis, the half-wave-plate is adjusted by approximately 90 degrees and the iterative procedure between the polariser and half-wave-plate is repeated.

The spatial beam quality was measured after the fibre using a Coherent Mode-Master (model MMH-3D). The ModeMaster obtains measurements using a fixed Ge detector array and a moving a lens. This effectively focuses a collimated beam through the lens and measures the beam size at different distances from the lens.

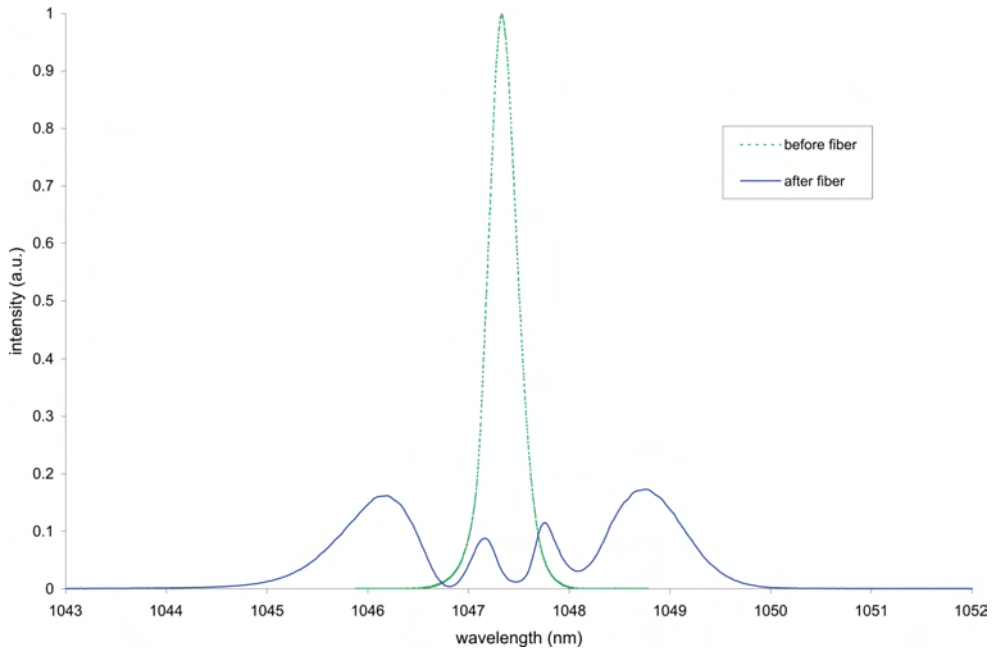

FIGURE 4.3: Experimental spectrum of a pulse before and after entering the short length of fibre, the data was captured on an optical spectrum analyser. The green curve represents the pulse spectrum before entering the fibre, while the blue curve corresponds to the spectrum of the pulse leaving the fibre. The area underneath the curves represents the energy of the pulse. In order to show the full effect of the pulse broadening the area underneath the curves have been normalised to the same value (i.e. it is assumed that propagation through the fibre has no effected the energy of the pulse).

The beam quality is parameterised by the M^2 factor (also called the beam quality factor). An $M^2 = 1$ corresponds to a spatial profile of the beam that is a diffraction-limited Gaussian; this is the most desirable situation. It was found that the M^2 after the fibre had a value of 1.1.

After the pulse had propagated through the fibre the pulse's spectrum had broadened to approximately $3.5\,nm$, while the pulse width remained approximately the same. The spectral bandwidth is large enough to allow the pulse shaper to produce sub-picosecond pulses, but still narrow enough for the acceptance bandwidth of the OPO crystal.

Figure 4.3 shows experimental broadening of the pulse spectrum. The asymmetry in the broadened spectrum is believed to be caused by a slight chirp or asymmetry on the incoming pulse. For a bandwidth-limited symmetric pulse, the SPM spectrum should be symmetric around the central wavelength.

The broadened spectrum is spread out across the spatial light modulator, which changes the phase profile across the spectrum. However, care must be taken to ensure that our seed laser is always mode-locked as it is noticed that when the laser becomes un-modelocked the peak intensity is significantly reduced, resulting in less spectrum generated from the fibre and therefore the aperture of the SLM is not "filled". Thus all of the power is concentrated on a small number of pixels at the centre of the SLM which could result in a significant increase above the maximum operational threshold value for safe use.

4.2 Mid-IR Diagnostics

An essential component of mid-IR pulse shaping is characterisation of the temporal and spectral properties. The spectrum of the pulse can be easily determined using a standard monochromator; the temporal profile of the pulse is more difficult since there exists no standard laboratory equipment to determine the pulse's temporal profile beyond $2\,\mu m$. For this reason, a mid-IR interferometric autocorrelator (IAC) was built to meet this demand. The autocorrelator was built by H.S.S.Hung and she played a significant contribution in characterisation of the mid-IR temporal pulses.

Working with light in the mid-infrared is difficult as standard optical components rarely work at these extreme wavelengths. Most commercial lasers operate in the visible to near-infrared and so most commercial instrumentation are designed for these wavelengths. Novel detectors and beam detection methods are therefore required. This section briefly mentions the commercial monochromator used, which was modified to allow for computer control. It then discusses the mid-IR IAC, some of the theory behind it and the experimental arrangement.

4.2.1 Spectral Analysis

The monochromator used in the research was a Bentham M300 Czerny-Turner monochromator. Information on this type of monochromator can be found in reference [7]. The device was used with 300 grooves per millimeter gratings and with variable entrance and exit slit widths of typically 10 to $30\,\mu m$. This with other monochromator parameters gives a wavelength resolution of less than $0.4\,nm$ [7].

A liquid nitrogen cooled InSb detector (EG&G Optoelectronics, Model: J10D-M204-R02M-19) with amplifier was used to measure the light at the exit slit.

The detector was attached to an oscilloscope in order to log the spectral trace. The monochromator was electrically modified so that it could trigger the oscilloscope. Therefore, with one switch it was possible to simultaneously start the monochromator and the oscilloscope. Each spectral trace typically took a few seconds to complete. CaF_2 lenses were used to focus and shape the light before the monochromator. Alignment of the monochromator was performed in two stages. Firstly a crude alignment using the $1.047\,\mu m$ pump light from the OPO, which was approximately collinear to the idler. Then a more accurate alignment by blocking the pump light and using a heat sensitive beam card to trace the path of the idler.

4.2.2 Mid-Infrared Autocorrelation

The temporal profile of the pulse is characterised via two photon interferometric autocorrelation (IAC). The technique of autocorrelation is well documented [8, 9] with the two main types of autocorrelations being intensity and interferometric. Interferometric autocorrelation was favoured because it reveals more information about the pulse [10], and for our purpose this entailed indicating whether a pulse is chirped or bandwidth-limited. Figure 4.4 shows the interferometric autocorrelation of two Gaussian pulses, one of which is heavily chirped, both pulses have the same intensity autocorrelation. The chirped pulse can be easily distinguished as it lacks full interferometric fringes throughout the trace, resulting in a pedestal, whereas the bandwidth-limited pulse has full fringes throughout and thus has no pedestal.

Figure 4.5 shows the Michelson interferometric setup used. The input beam is split into two by the beamsplitter; one of the beams follows a fixed path length while the other is varied. The beams are reformed at the beamsplitter and focused into a detector. The two photon autocorrelation seen by the detector is given by

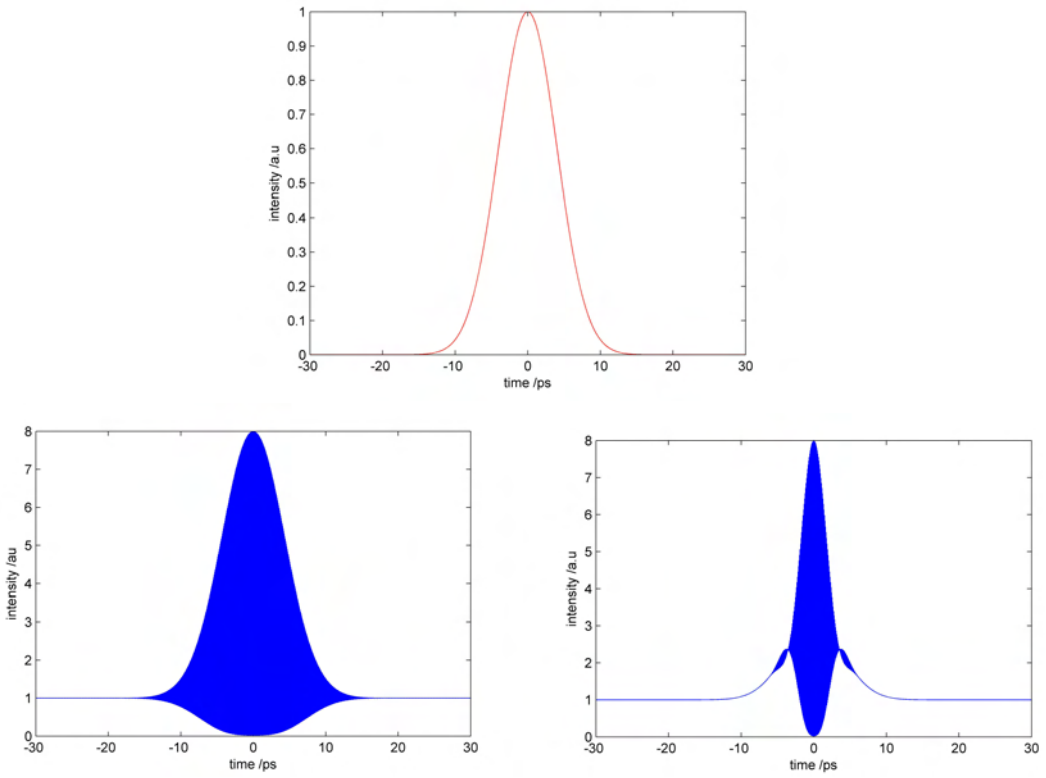

FIGURE 4.4: The figures at the bottom show theoretical interferometric autocorrelation traces for two Gaussian pulses. The figures show the interferometric fringes of the pulses, but since the fringes have a very short period compared to the width of the pulse, they have the effect of appearing in the figures as solid blue shading. The figure on the left corresponds to a bandwidth-limited pulse, which the right indicates a heavily chirped pulse. The intensity autocorrelation of the pulses is the same, and shown in the top figure.

the expression:

$$\begin{aligned} I_{IAC}(\tau) &= \int_{-\infty}^{\infty} [I^2(t) + I^2(t-\tau)]dt \\ &+ 4\int_{-\infty}^{\infty} [I(t) + I(t-\tau)]\mathrm{Re}[E(t)E^*(t-\tau)]dt \\ &+ 2\int_{-\infty}^{\infty} \mathrm{Re}[E^{*2}(t-\tau)E^2(t)]dt \\ &+ 2\int_{-\infty}^{\infty} I(t)I(t-\tau)dt \end{aligned} \tag{4.1}$$

where $I_{IAC}(\tau)$ is the intensity seen by the detector, $E(t)$ is the electric field of the pulse and τ is the variable delay. The first term in the expression is a constant, the last term is the intensity autocorrelation. The second term describes the interferogram of the pulse. The third term describes the interferogram of the

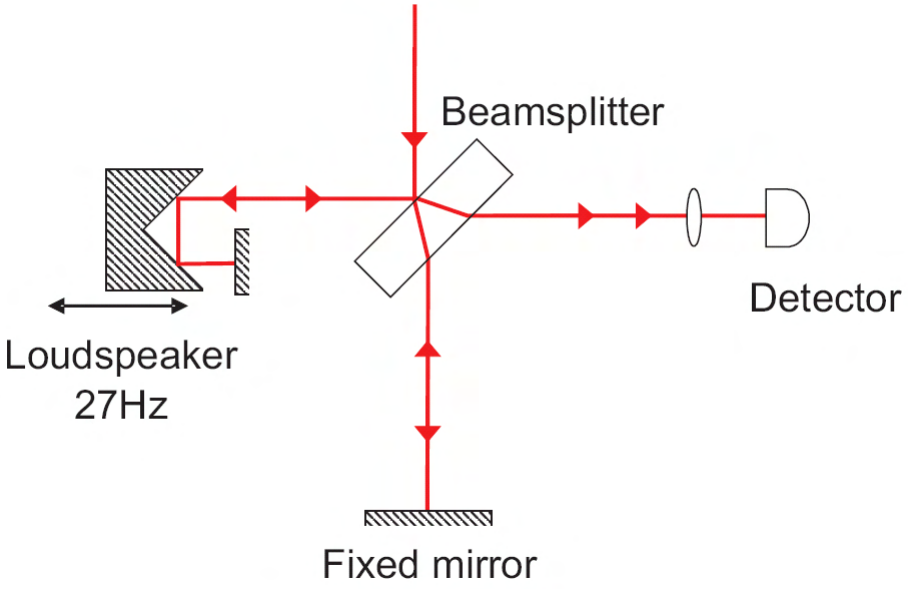

FIGURE 4.5: Schematic of Michaelson interferometric autocorrelator. The variable delay was provided by the loudspeaker fitted with a retro reflecting corner cube mirror.

pulses second harmonic, this term oscillates at twice the frequency of the second term [9]. As can be seen the IAC is a complicated expression with many terms, but despite this, it is useful in determining temporal characteristics of a pulse. For all IAC the contrast ratio for peak to background is 8:1.

The autocorrelator used a $2\,mm$ thick silicon window as the beamsplitter, using Fresnel reflection off the front surface. The thickness of the material is not expected to significantly broaden the pulses due to GVD. The variable delay was provided by mounting a corner cube mirror on a loudspeaker. A retro-reflecting mirror was inserted just after the speaker so as to double the displacement range. The maximum displacement of the speaker was $4\,mm$, which gives the autocorrelator a time window of $26\,ps$. The extended InGaAs photodiode used two photon absorption (TPA) in the mid-IR spectral regime [11]. The process of using TPA in a photodiode is a cheap, simple, and highly effective way of making an interferometric autocorrelator [12]. The current from the diode is converted to a voltage and amplified. This amplified voltage in then recorded on an oscilloscope.

The calibration of the IAC is important in order to relate the trace of the autocorrelation observed on the oscilloscope to the time duration of the real pulse. The most common calibration method involves moving one of the mirrors in the setup by a fixed distance, and observing the shift in the autocorrelation trace across the screen of the oscilloscope [13]. The displacement of the mirror can be converted into a time difference by first noticing the change in the path length of the beam. Moving the fixed mirror in figure 4.5 the path difference the beam experiences is twice the displacement of the mirror, and for movements of the speaker this corresponds to four times the displacement. This path difference is then divided by the speed of light, therefore relating distances observed on the oscilloscope, with real time differences of the pulse's autocorrelation. This method can be used for interferometric as well as intensity autocorrelations.

The other common calibration method can only be used with interferometric autocorrelators, and is often referred to as "internal calibration" [14]. This method does not rely on adjusting the setup or measuring any physical parameters within the autocorrelator. To determine the time axis of the interferometric autocorrelation, all that is required is data from the oscilloscope and knowledge of the central wavelength of the pulse. In order to relate the pulse trace seen on the screen to the real time domain it can be noted that the difference between two adjacent interference maxima on the scope t_i is related to the speed of the speaker v via the simple expression of $v = \lambda_0/t_i$ where λ_0 is the central wavelength of the pulse. Hence, the speed of the speaker can be inferred without actually measuring it. Using this expression one can relate an arbitrary displacement on the scope t_{scope} to the real time t using the expression $t = vt_{scope}/c$. This method was preferred in determining the calibration factor of the IAC. To increase the accuracy of determining the separation of interference maxima on the scope the average across 30 interference fringes was determined. The calibration factor was determined to be $2\,ps/ms$.

4.3 The Optical Parametric Oscillator

A schematic of the basic synchronously pumped OPO (SPOPO) setup is shown in figure 4.6 The cavity length of the SPOPO is determined by the repetition rate of the laser. For our laser this corresponds to a round trip of 2.5 meters. The SPOPO

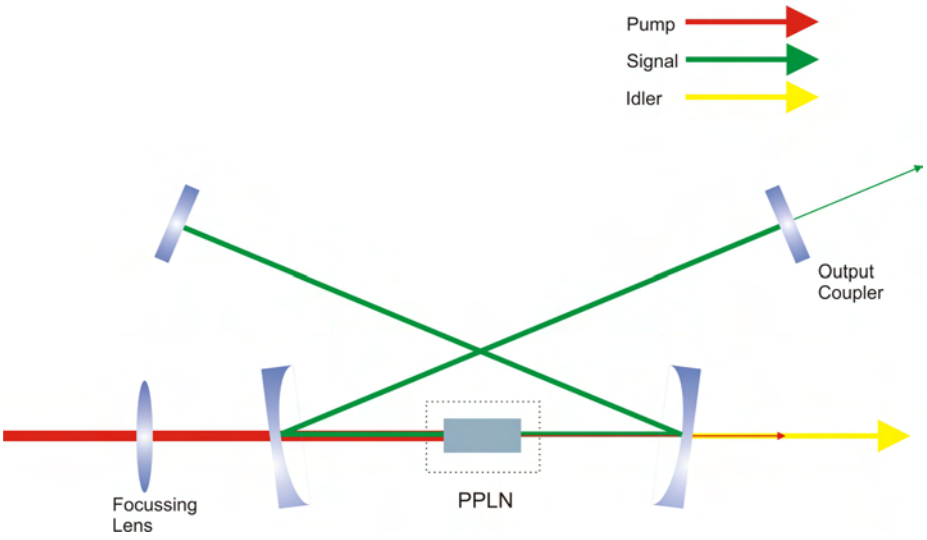

FIGURE 4.6: Basic layout of OPO consisting of 2 concave mirrors with radius of curvature of 150 mm, one plane mirror and one output coupling mirror.

is constructed in a standard standing-wave arrangement [15–19]. The other common arrangement is a ring cavity [20, 21], which has a lower threshold, due to lower losses, mainly as a consequence of one-pass through the PPLN crystal. However, ring resonators are more difficult to align than standing-wave resonators, this is especially true when changes in the cavity length are required. Furthermore, spectral narrowing optics are placed within the OPO in order to restrict the spectral bandwidth of the signal. These optics are typically birefringent filters and etalons. With a standing-wave SPOPO, the signal beam per round trip experiences two passes through these optics (compared to one pass for a ring-cavity), thus doubling the loss that the undesired spectrum sees. It is also far easier to insert the spectral narrowing optic within a standing-wave arrangement, since the beam off the plane mirrors is exactly retro-reflected back along the original direction of propagation. Inserting the new optics does not deviate the beam, and one needs only translate a flat mirror to account for the reduced path length the new optic has introduced. Finally, one of the mirrors could be replaced with a diffraction grating in order to achieve spectral narrowing [22, 23].

The SPOPO consists of four mirrors, two of which are concave with radius of curvature of 150 mm, and two of which are plane mirrors. The two curved mirrors are used to focus the resonating signal beam into the crystal. All of the mirrors within the OPO are dielectric coated and highly reflective in the wavelength range between 1.3 and 2 μm, with high transmission at the pump and idler wavelengths

(although one of the plane mirrors can have a reduced reflectivity to allow signal output coupling, if desired). This arrangement allows only the signal pulse to resonate within the cavity. The residual pump and idler are extracted through the second curved mirror (see fig 4.6). However, since the idler is typically in the $3\,\mu m$ wavelength region, the mirrors can not be made of standard BK7 optical glass - as this is only transparent up to $2.1\,\mu m$. Instead, CaF_2 was used as the substrate, as this has a transparency range of up to $8\,\mu m$. The idler passes through the curved mirror at a slight angle, which may degrade its beam quality. If this should be a problem then a flat mirror can be placed soon after the crystal. Using this, the curved mirror can then be relocated away from the path of the idler beam.

In order to maximise the DFG process it is important to have high intensity pump and signal beams. The signal beam is confocally focused into the crystal by the two curved mirrors within the SPOPO. Confocal focusing roughly maximises the intensity of the beam over the length of the crystal. It is related to the Rayleigh range z_R, which is the distance from the beam waist (of a diffraction limited Gaussian beam) w_0 whereby the beam radius has increased by a factor of $\sqrt{2}$:

$$Z_R = \frac{\pi w_0^2 n(\lambda)}{\lambda} \tag{4.2}$$

where λ is the wavelength in free space and $n(\lambda)$ is the refractive index of the material. The signal waist size is thus set to give a Rayleigh range that is half the length of the PPLN crystal and is located at its centre. The pump beam is also confocally focused. The resonator cavity nominally restricts the transverse mode of the signal to a diffraction-limited Gaussian.

The analysis of focusing for parametric processes has been studied in depth by previous authors [24, 25]. The most comprehensive is by Guha [25], who assumes CW interaction, low-gain, and beams with a TEM_{00} transverse profile. Guha's analysis shows that the optimum focusing is a function of wavelengths used and in general better efficiency can be achieved with somewhat tighter than confocal focusing. However, the theoretical increase in efficiency is not large and therefore near confocal focusing is used here, as the slightly larger spot sizes are easier to achieve in practise.

The crystal used throughout this work has a length of $10.7\,mm$. This gives a confocal focusing spot size of $35\,\mu m$ for a $1510\,nm$ signal and $29\,\mu m$ for $1047\,nm$ pump. However, resonator beam propagation calculations show that achieving

this size in both spatial axes is difficult for the signal. As can be seen from figure 4.6 the curved mirrors are used at a slight angle to the incoming signal beam. This causes the effective focal length of the mirror to be different in the two planes, which causes the spot sizes in the tangential (x-axis) and saggital (y-axis) direction to be slightly different. The angle of the lens also cause slight astigmatism and coma of the beam [26]. Care is taken in trying to use the mirror as close to normal incidence as possible. In practise the angle of incidence for the signal beam is estimated to be less than 3 degrees from the normal of the mirror. Using this angle, the best spot size of the signal beam in the crystal is estimated to be $32\,\mu m$ in the x plane and $36\,\mu m$ in the y plane. This may change in practise as it is customary to optimise the threshold of the OPO by adjusting the separation of the curved mirrors. This has the effect of changing the signal spot size, and optimal performance is achieved when the signal spot size achieves good spatial overlap with the pump.

The nonlinear crystal used in the research. As mentioned before is periodically poled lithium niobate. It was poled at the Optoelectronics Research Center by Lu Ming. The crystal was $0.5\,mm$ thick and has 6 grating periods: $29.2\,\mu m$, $29.5\,\mu m$, $29.8\,\mu m$, $30.0\,\mu m$, $30.2\,\mu m$, and $30.4\,\mu m$. The crystal was housed inside a custom built oven. The purpose of the oven was to allow temperature tuning of the signal wavelength. With the crystal at a fixed temperature of $150°C$ the tuning range of the crystal across all grating periods was 1.5 to $1.7\,\mu m$ for the signal wavelength and an idler range of 2.8 to $3.4\,\mu m$. Temperature tuning of the OPO is possible due to two effects; the change of the refractive index of the material with temperature, and thermal expansion changing the grating period. Changing the temperature in the practical region of $100°C$ to $280°C$ results in a change of signal wavelength of 100 to $400\,nm$ depending on the grating period, with longer grating periods having longer tuning ranges.

The crystal was polished, and anti-reflection (AR) coated in an Edwards vacuum coating machine by depositing a single layer of magnesium fluoride (MgF_2) on both sides of the crystal. The thickness of the deposition was chosen to minimise the reflection losses for a signal wavelength of $1.7\,\mu m$, as this is approximately the middle signal wavelength for the crystal. To calculate the required AR coating thickness, data in relation to the refractive index of magnesium fluoride was taken from reference [27], while information regarding the refractive index of lithium niobate was used from reference [28]. To achieve the minimum reflection loss, the

layer of MgF_2 should be 310 nm on each side of the crystal. However, in practise, coating thicknesses of 306 and 311 nm were recorded by the Edwards vacuum coating machine. It is expected that with these coating thickness the maximum reflection loss over the signal wavelength range of the crystal is less than 1%. The crystal is not specifically AR coated for the pump and idler wavelengths. Therefore, it is expected that the pump reflection is approximately 11% off each surface of the crystal, which is slightly better than the case of no AR coating ($\sim$ 14%). The idler reflection loss on the other hand is reduced from about 12% per surface to about 7%.

Calculating the threshold of the OPO can be performed using a number of different analyses. The method used throughout this thesis is an extension of the method described by Guha [25] to include the effects of a pulsed pump and signal. The treatment combines Guha's analysis with that described by McCarthy and Hanna [20], this combined treatment is described by Hanna et. al. in Ref [22]. The treatment uses the threshold condition given by Guha, but includes the temporal effects mentioned by McCarthy. It can be noted that the spatial overlap of the beams is already accounted for in Guha's analysis, therefore the spatial term g_s from McCarthy's treatment is omitted. The temporal nature of the pulse, has the effect of replacing the crystal length used in Guha's analysis with an "effective parametric gain length" (given as l'_g in Ref [20])

$$l'_g = l_t \mathrm{erf}\left(\frac{\sqrt{\pi}}{2}\frac{l_c}{l_t}\right) \tag{4.3}$$

where l_c is the length of the crystal, $\mathrm{erf}(x)$ is the error return function, and l_t is the temporal aperture length [20]. The change to an effective parametric gain length was included in order to account for the effects of group velocity mismatch between the pump and signal; whereas in Guha's original analysis the pump and signal are assumed to be CW. Furthermore the gain coefficient (C_1) given by Guha [25] is modified by multiplying it by McCarthy's temporal overlap factor g_t, which accounts for the averaging of the gain due to the temporal shape of the pump and signal pulse. Therefore the threshold calculation takes into account focusing of the pump and signal beams, and pulsed interaction between the pump, signal, and gain. However, it still assumes low gain. Finally, in order to account for the effects of M^2 to a first approximation, it can be assume that only the embedded TEM_{00} Gaussian beam (as is explained in section 4.5.2) of the pump interacts with the signal beam. This is because the higher order spatial components of the

pump beam have poor spatial overlap with the signal beam and it is expected they do not contribute significantly to the overall parametric process.

Using the pulses out of the fibre, and after the pulse shaper, and by only having high reflecting mirrors within the OPO, the threshold of the OPO was measured to be $85\,mW$ incident on the PPLN crystal. The M^2 of the pump beam was approximately 1.6, and it was focussed into the PPLN crystal such that the confocal focussing condition was met for the embedded TEM_{00} Gaussian beam. If we assume the signal pulse width is similar to the pump and that the losses in the cavity for the signal round trip are estimated to be 10%, then the theoretical threshold of the OPO is calculated as $68\,mW$.

Typical signal, idler and pump spectra and autocorrelation traces are shown in figure 4.7. As expected, it can be seen that the idler spectrum does not show the fine structure seen in the pump. Furthermore, the idler IAC shows a pedestal. As discussed previously, this shows us that the idler pulse is heavily chirped.

In Chapter 6 methods of ensuring better spectral transfer from the pump to the idler shall be investigated.

4.4 The Spatial Light Modulator

For a phase modulator to be effective it must be able to introduce a phase shift of up to 2π to each frequency component. Most modulators are able to retard light by more than this amount. The excess retardance is not necessarily required since introducing a phase shift of exactly 2π merely brings the peaks and troughs of the wave back into phase with each other. A phase shift with a value greater than 2π is the equivalent of a shift with the same value but minus 2π. This principle can be used to put a phase profile to the pulse that varies by more than 2π. To do this the extended phase can be wrapped within a 2π range, see figure 4.8. This is the same trick used in Fresnel lenses. There is a limit to this technique, in that the phase profile put to the hardware must approximate a smoothly varying curve, since large phase differences between adjacent pixels results in diffraction of the beam, and thus phase-to-amplitude modulation [29]. Therefore, the phase difference between adjacent pixels must be significantly less than π.

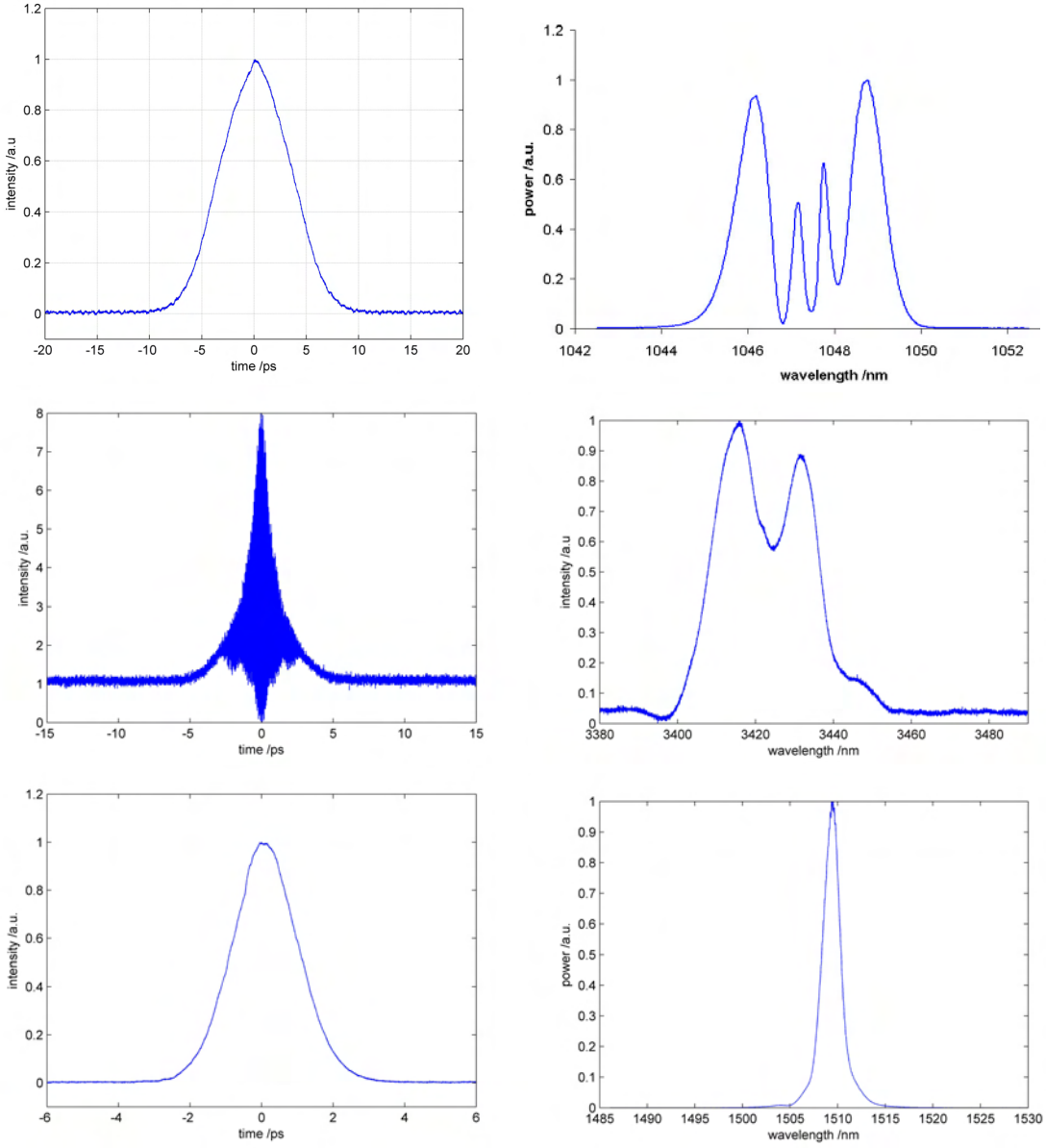

FIGURE 4.7: From the top going downwards show autocorrelations and spectra for the pump, idler, and signal. The idler autocorrelation is interferometric, but the time scale is too long to show the individual interferometric fringes. While the other autocorrelations are intensity autocorrelations

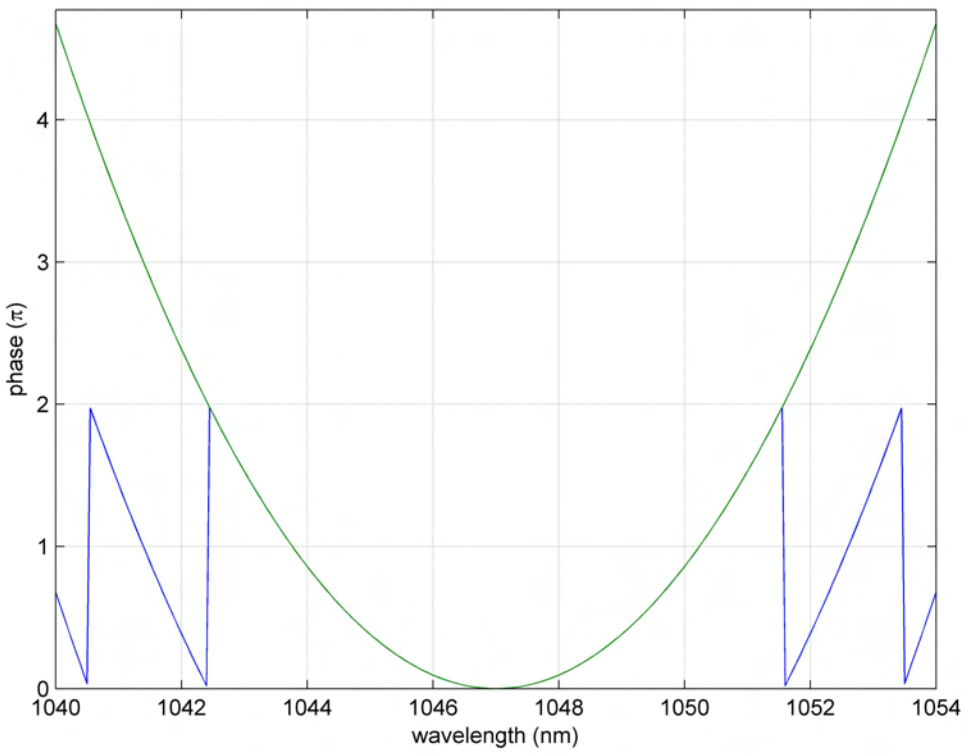

FIGURE 4.8: Theoretical plot of the phase versus wavelength. The blue line represents the phase bounded between 0 and 2π while the green line represents "unwrapping" of the phase profile.

It is important to know the phase response of the SLM when a certain drive voltage is put on a pixel. Without this information it is impossible to obtain meaningful phase coefficients to equation 3.25. Directly measuring the phase response of the liquid is difficult. Fortunately, the device can be converted to amplitude modulation with a suitable arrangement of polarisers. Normally, for phase retardation, the SLM is used with horizontally polarised light. But by having the incoming light at 45 degrees to the slow and fast axis of the crystal, it is possible to produce elliptically polarised light, and in this way the liquid crystals act like a variable waveplate. By placing a polariser after the SLM, which is in the same orientation as the polarisation of the incoming light, it is possible to achieve amplitude modulation. The relationship between phase ϕ and transmission of light T through the setup is given by $T = I/I_{max} = \cos^2(\phi/2)$ where I_{max} is the maximum intensity of light observed.

For calibration purposes the device includes a special $2 \times 2\,mm$ pixel at the end of the pixel array. The large pixel allows for calibration without concern for

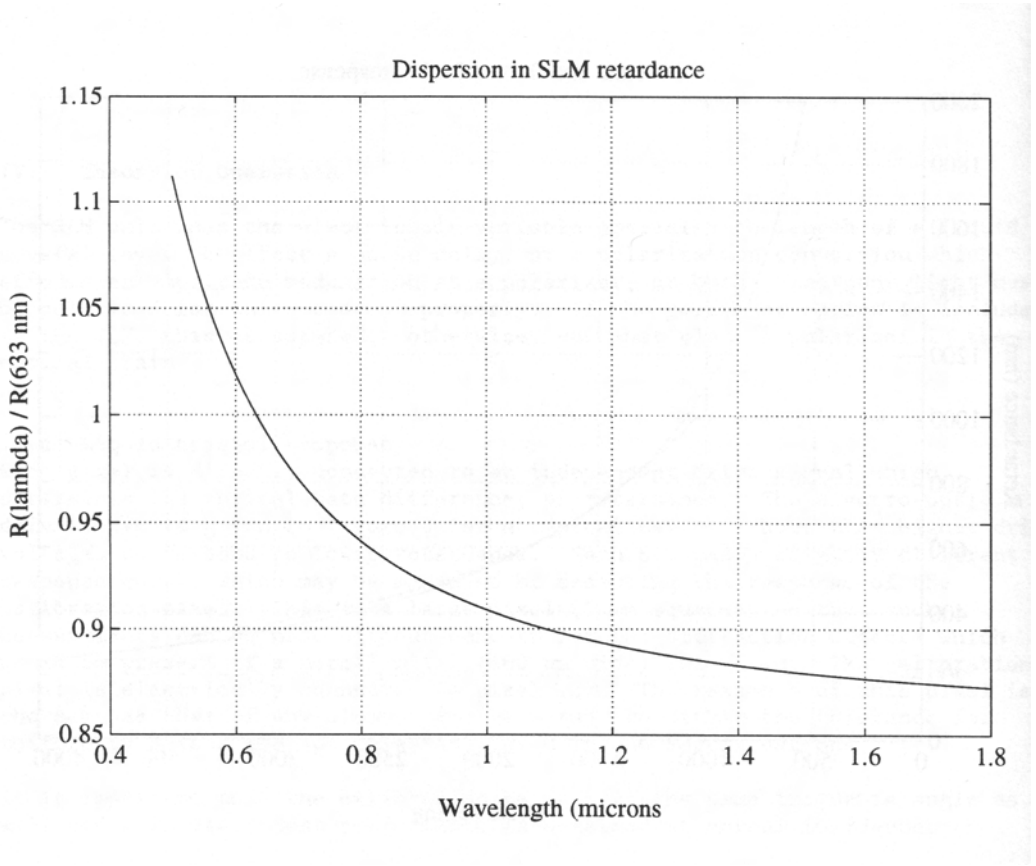

FIGURE 4.9: Graph showing ratio of retardance at 633 nm compared to an arbitrary wavelength, as a function of wavelength.

diffraction effects, which would be present if a normal ($100\,\mu m$ wide by $2\,mm$ height) pixel was used. It is assumed that the response of all the pixels to an applied voltage is the same. There is a chance that this may not be true, which would mean that any experimental parameters retrieved from the code contain a systematic error. But since an adaptive search algorithm is used, incorrect phase to voltage calibration data do not affect the convergence of the algorithm. Furthermore, since the spectral bandwidth used in future experiments is small ($3.5\,nm$) it is assumed that the response curve for the central wavelength is the same for all wavelengths within the bandwidth. This is partially justified by data supplied by the manufacturers. Figure 4.9 shows a graph taken from the SLM's operating manual. It shows a curve which relates the ratio of retardance of light at $633\,nm$, R($633\,nm$), to that of an arbitrary wavelength, R(lambda). It can be seen that the change in retardance at about 1 μm wavelength, is significantly less than 1%. Hence justifying our assumption of the retardance being constant with wavelength across our bandwidth. In order to correctly locate the calibration

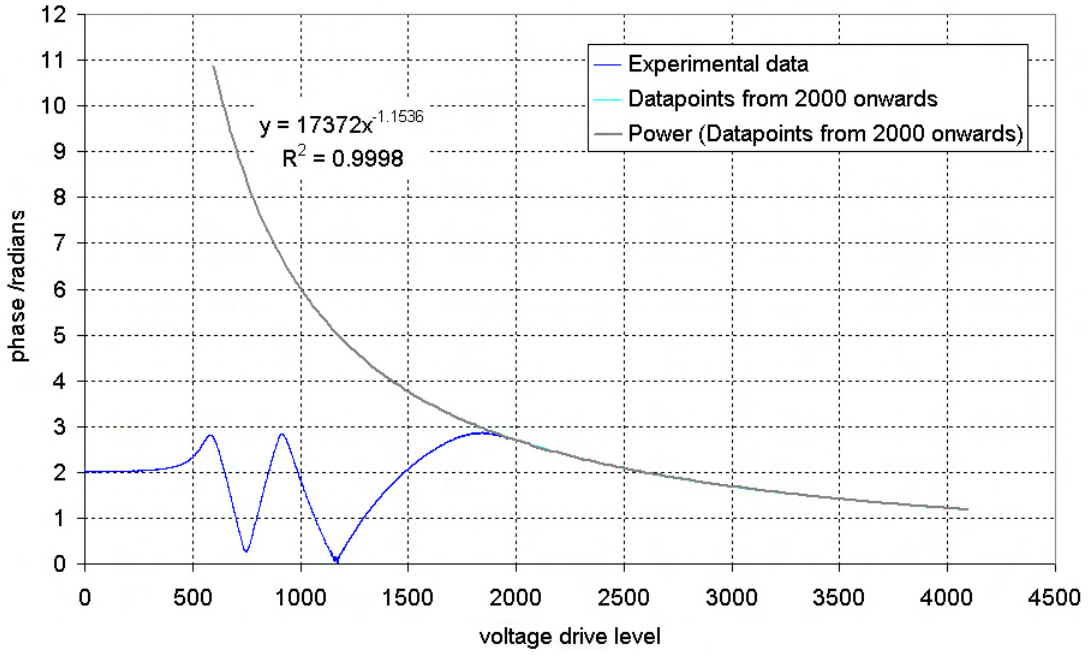

FIGURE 4.10: Experimental data for phase response of SLM with voltage drive level. Also shown is best fit (power function) curve which is determined by fitting a curve to data points 2000 onwards. The best fit curve shows the equation of the curve, and the "R squared value" for data points from 2000 onwards. The R squared is a measure of how well the best fit curve fits the data points, a value of 1 indicates a perfect fit.

pixel a small blinking program was coded. This program repetitively changed the voltage drive level on the calibration pixel between two set values, allowing the pixel to be found quickly and accurately by simply moving the SLM until maximum change was observed on a photodiode. The data for the phase response of the calibration pixel to voltage drive level is shown in figure 4.10. The data points show an oscillation from high to low retardance as the voltage level is increased; this is due to the liquid crystals being able to retard light by more than 2π radians and is to be expected. However the oscillations prove problematic in trying to "unwrap" the phase response of the pixels. From the user manual it is expected that the phase response of the liquid crystal should be smoothly varying with drive voltage. Attempts to try to "manually unwrap" the experimental phase response did not yield a smooth curve. Instead an alternative approach is required. It can be seen that the data points from 2000 onwards are away from any inflection point. Therefore, the last 2096 data points were considered, and a best fit curve was applied to them, the curve was extrapolated backwards to determine the phase response for lower voltage drive levels. Finally, it can be seen from the experimental data points that for the first 500 data values the liquid crystals do

not significantly change the retardance of light. This is because before the liquid crystals can change orientation they must first overcome any resistance to their motion. Such resistance is provided by Van der Waals forces of attraction between molecules. In order to determine accurate phase response data, only voltage drive levels from 600 onwards are considered.

The best fit curve is used to generate data points which are placed inside a simple text file. The computer program reads all the data from this text file and store it as a lookup table. This lookup table is used to relate phase to voltage drive level. An alternative approach to the lookup table was to use the equation for the best fit curve. But a lookup table is more robust and easier for future users to modify, as it does not require the user to change the program. By considering the highest and lowest phase response of the SLM calibration pixel it is found that the SLM is able to achieve a phase shift of 9.60 radians for 1047 nm light.

4.5 The Pulse Shaper

4.5.1 Theoretical Characteristics

The pulse shaper has many design criteria with most design parameters being coupled together. One such criterion is that the spectrum of the pulse should fill the SLM aperture. This criterion couples the dispersion of the grating, the focal length of the lens, the bandwidth of the spectrum, and the width of the SLM aperture. Fortunately, the dispersion of the grating varies with the incident angle, and this gives some leeway in the design.

The pulse shaper used holographic diffraction gratings (Newport, catalogue number 53108BK01-136H) with a groove density of 1714 grooves per mm (gr/mm). The gratings were gold coated and had a length of 52 mm. They were held in a custom mount, which was mounted on top of a tilt stage, which was secured on top of a high precision rotation stage. This arrangement allowed the grating to be tilted and rotated in a number of directions, therefore allowing both gratings in the setup to be orientated identically. Two identical BK7 plano-convex cylindrical lenses were used inside the shaper. The exact focal length of the lenses for 1047 nm light was determined using technical data supplied by the manufactures and a ray tracing program called Zeemax. The focal length was calculated to be

254.9 mm. The lenses were placed inside mounts that allowed them to be tilted in the direction perpendicular to the incoming beam. It is important that the lenses have exactly the same orientation to avoid distorting the beam. For the rest of this research the spatial profile of the beam parallel to the table is referred to as the x axis, the profile vertical to the table is the y axis. The optics used (grating, lens, SLM) only effect the beam in the x direction, the vertical component of the beam (y direction) is left unchanged.

Based on the focal length and grating groove density the diffraction gratings were angled such that light was incident at an angle of 53.4°, which leads to a diffracted angle of 82.7°. This resulted in the middle 12 mm of the SLM aperture (which has a total width of 12.8 mm) being illuminated by the FWHM of the pulse spectrum. It can be seen from figure 4.3 that the spectrum generated by SPM has steep edges at the extreme ends of its spectrum, it is therefore expected the SLM is able to modulate most of the spectrum. The area either side of the pixel array is transparent, as a result light that is not modulated by the pixels is not truncated by the SLM but pass through it

As mentioned in section 3.2, illuminating a large section of the grating is advantageous. The beam before the grating was expanded to a spot size of 5 mm using a cylindrical telescope arrangement. This, coupled with the angle that the grating was used at, ensured that the maximum number of grating lines were illuminated. The beam size was not large enough to cause significant quartic-phase-aberration after passing through the lens inside the shaper as it is only 1mm at this point. The reduction in the spot size is due to the beam being diffracted off the grating at a very shallow angle to the grating surface. All of the lenses used in the setup were carefully chosen so as to cause minimum degradation to the spatial profile of the beam.

In order to achieve a wide variation of temporal pulse shapes a large spectral bandwidth is required. This is readily deduced by the time-bandwidth product (for a sech^2 pulse this is 0.315), which implies that the shortest temporal feature δt in the outgoing shaped pulse is inversely related to the spectral bandwidth B ($B\delta t \cong constant$) [30]. There is also an equivalent relationship between the maximum temporal window in which the pulse shaping can occur, and the finest spectral feature δf which can be modulated in the bandwidth. These relationships put a limit on the total number of temporal features η which can be realised in the

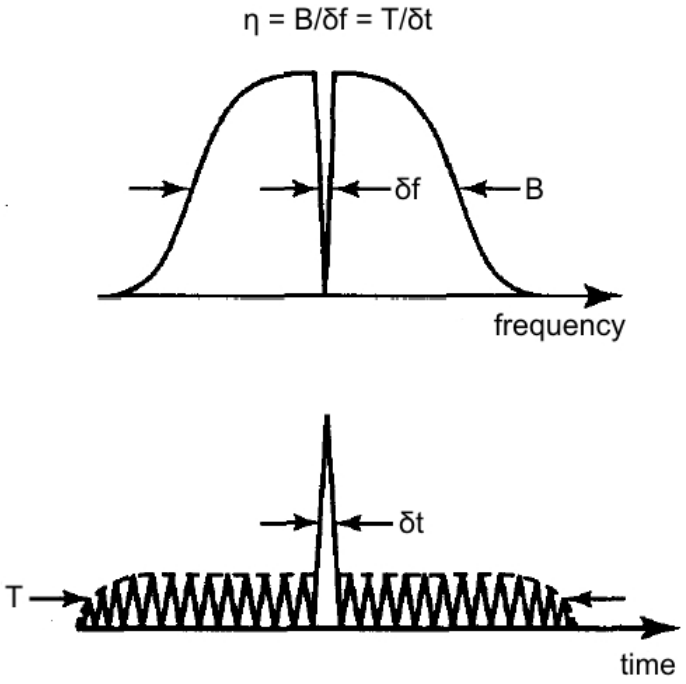

FIGURE 4.11: Top diagram showing spectral frequency of a pulse of bandwidth B. δf represents the smallest spectral feature that can be modulated. Lower diagram showing a highly modulated pulse, δt is the shortest feature in the pulse and is related to the total bandwidth, B. It can be seen that the pulse shaper can only modulate a pulse within a certain time window called T. Diagram taken from [30]

final shaped pulse, as was discussed in section 3.2. Figure 4.11 pictorially shows these principles:

Characteristics of our pulse shaper can be calculated using equations given in chapter 3.2. Shannon's sampling theorem was used in order to determine the minimum resolving power the system should have in order to recombine the pulse using the diffraction gratings. In order to determine the sampling frequency a Fourier transformation of the spectrum of the pulse was performed. Using this it was determined that the minimum resolving power of the grating should be $0.28\,nm$. The actual resolving power of the grating (equation 3.3) was calculated to be $\sim 0.023\,nm$. In order for each pixel to sample a unique part of the bandwidth the resolving power should be $0.027\,nm$. The maximum complexity of the shaper is calculated using equation 3.5 to give a value of $\eta = 181$, and the time window was calculated using equation 3.18 as $\Delta t = 84\,ps$. Finally the spot diameter of individual frequency components focused at the SLM was calculated to be $159\,\mu m$,

which is larger than the width of the pixels. This effectively reduces the number of pixels in the modulator.

If the spectral bandwidth of the laser was 35 nm instead of 3.5 nm then this would make it easier to satisfy more of the requirements in the pulse shaper. Since with a 35 nm bandwidth, each pixel in the SLM would modulate a larger bandwidth of light, therefore the gratings do not need to be as dispersive. To illustrate this point, a pulse with a 35 nm bandwidth would only require 1100 gr/mm gratings, which could be operated close to Littrow [31] with the same 255 mm lens, and using the same expanded beam onto the shaper would produce a spot diameter for an individual frequency component at the SLM of 40 μm.

4.5.2 Experimental Alignment and Results

The pulse-shaper was aligned using the guide presented by Weiner in Ref [32]. For completeness, the procedure is described here. Before aligning the shaper it is important to ensure than the incoming laser beam is well collimated, parallel to the table, and free of any spatial irregularities. This was easily achieved since the beam originated from a single-mode fibre. To ensure the collimation of the beam a far-field imaging system was used. For a well collimated beam the width of the spot size, as seen at the focal plane of a lens placed in the beam path, is at its minimum. A larger spot-size can be corrected by micrometer adjustments of the distance between the end of the fibre and the fibre lens. The system used a CCD camera to observe the focused spot-size.

With the laser well collimated a cylindrical telescope was placed to expand the laser beam horizontally. The cylindrical telescope used -60 and 500 mm focal length cylindrical lenses, which magnified the horizontal component of the beam to a spot-size of 5mm. To minimise aberrations for a collimated beam hitting the lens, the first surface that experiences the beam should be curved, and for a focused beam impinging on the lens the flat surface of the lens should be the first surface the beam encounters. This rule-of-thumb was followed for all lenses used within the setup (including spherical lenses). The output beam from the cylindrical telescope was collimated using the same setup described earlier. The collimation apparatus was first setup, then each of the cylindrical optics was introduced and the position of the beam on the camera checked to ensure that the light was passing through the centre of the lens. The lenses were AR coated for 1047 nm light, but despite

this, a small amount of light would be reflected off each surface. This light can be seen using a sensitive handheld infrared beam viewer. The lenses were tilted in their mounts until the reflected light from the first surface on the lens was retro-reflected back to the fibre. This method ensured that the lenses were mounted perpendicular to the incoming beam and would therefore not deviate the beam in the vertical plane. This procedure was used with all cylindrical lenses. With the lenses in place, the separation between them was adjusted to achieve maximum collimation (as observed on the beam camera).

The lenses used within the shaper were arranged in a 1:1 cylindrical arrangement. Although the focal length of the lenses had been calculated the required separation of the lenses was tested experimentally by setting then up in the collimated beam. The separation of the lenses was adjusted to maximise collimation and the distance from the flat surface of one lens to the flat surface of the other lens was measured using a ruler. The distance was determined to be $501\,mm$. When the 1:1 cylindrical is incorporated inside the pulse shaper the lenses were separated by $501\,mm$, to ensure they were in an exact 1:1 cylindrical arrangement.

The 1:1 cylindrical arrangement is removed from the optics bench. Therefore, the beam leaves the fibre and passes through the first cylindrical arrangement. This beam is then incident on the first diffraction grating of the pulse shaper. The grating was adjusted to retro-reflect the light back to the fibre, as observed using the handheld infrared viewer. The grating was then rotated in the plane of the table, and different diffraction orders were observed and their heights from the table were measured. The grating was tilted such that the diffraction orders all had the same height above the table. This ensured that the grooves on the diffraction were perpendicular to the optics bench.

The gratings needed to be correctly rotated. It was found that using the vernier scale on the rotation stage was ineffective for accurately determining the angle required. This is impart due to the high accuracy required. For example, from theory it is known that light incident on the grating at $53.39°$ results in a wavelength spread at the Fourier plane of $12.00\,mm$, but with light incident at $53.33°$, the spread increases to $12.46\,mm$. Instead of measuring angles an alternative method was used, which involved observing the spread of light at the Fourier plane. The rotation stage was crudely rotated to the correct angle, and then the first lens was placed inside the shaper at the correct distance. The spread of the beam at the Fourier plane was measured and fine adjustments of the rotation stage made until

the desired broadening was observed. The lens was readjusted to ensure the beam passed through its centre and the broadening checked again and if need be, the grating was rotated, this process was iterated until the correct spread was observed and the beam passed through the centre of the lens. The height of the SLM pixels is $2\,mm$, and the vertical component of the light was able to pass through this region.

The 1:1 cylindrical telescope was placed inside at the distance previously determined. Then the last grating was placed one focal length away from the last lens. The groove periods on the grating were aligned using the same method as used for the first grating. Then the grating was crudely rotated by retro-reflecting the light back to the fibre and then adjusting the angle using the vernier scale.

With the diffraction grating angles used, the grating efficiency of dispersing the incoming light into the first order was measured to be 69% for the first grating and 64% for the last grating. With $2.3\,W$ passing through the fibre this gave $1.7\,W$ of power incident onto the SLM, which is below the damage threshold of the SLM. The SLM device had a thin polariser incorporated just in front of it in order to remove any incorrectly orientated light, which had an experimental contrast ratio better than 6,600:1.

In order to ensure that the pulses leaving the shaper were not spatially chirped the procedure given in Ref [32] was extended by focusing the light after the shaper onto a beam camera using a $500\,mm$ lens, which is placed one focal length away from the camera. By performing this procedure it is possible to view the far-field diffraction pattern of the beam. The light at the Fourier plane was progressively blocked out by sweeping a small sheet of metal through it. It is expected for a spatially-chirp-free beam that the intensity of the beam decreases uniformly across its spatial profile. However, if the beam possesses some spatial-chirp then this results in an uneven decrease in its intensity across the beam. By observing the beam in the far-field the sensitivity of the detection process is increased. In order to correct for any spatial-chirp the last grating in the setup is rotated so as to angularly recombine all of the frequencies. With this procedure it was possible to produce spatial-chirp free pulses. Furthermore, an autocorrelator was used to adjust the position of the last grating such that the pulse duration seen on the autocorrelator was the same as the input pulse to the shaper. It was necessary to iterate between grating rotation and position in order to compensate for both spatial chirp and pulse duration. Figure 4.12 shows the autocorrelation trace of

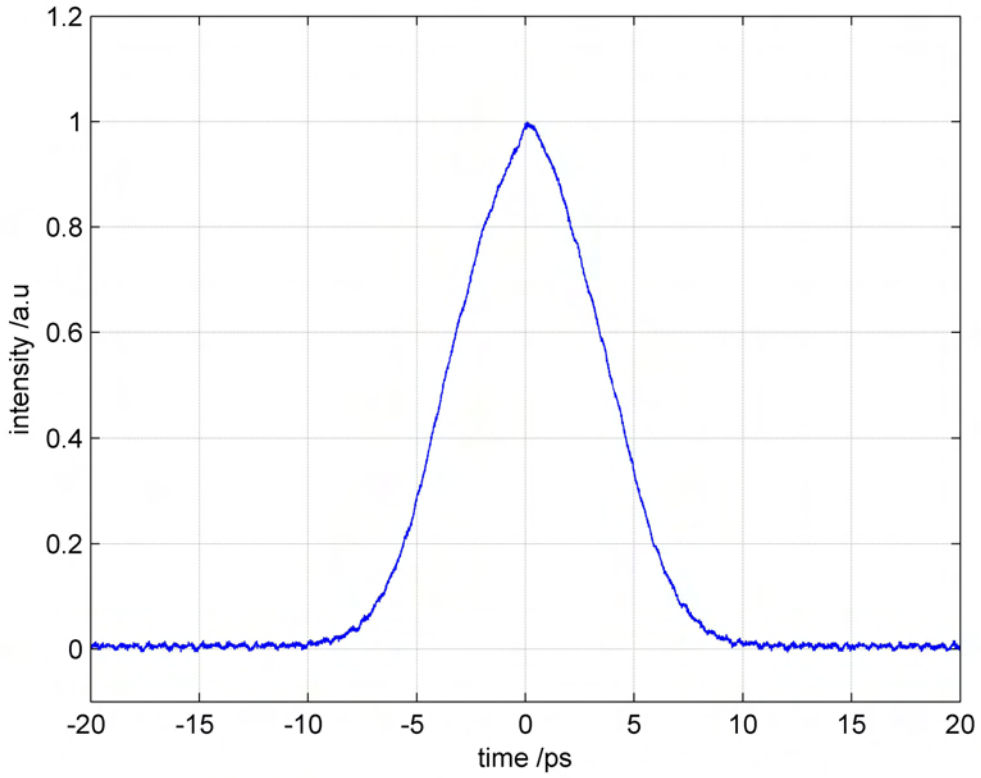

FIGURE 4.12: Autocorrelation trace shown after shaper. The FWHM is 6.5ps, assuming this trace corresponds to a sech^2 pulse gives the FWHM of the pulse as 4.2ps.

the pulse after the shaper, it has a similar FWHM as the input autocorrelation and the same shape. The spectrum of the pulse after the shaper is identical to that which entered.

A cylindrical telescope arrangement, with focal lengths 500 and $-150\,mm$, was placed after the shaper in order to shape the spatial profile of the beam and to correct for divergence asymmetry. In order to perform these tasks successfully it is necessary to measure the M^2 of the beam, and consider this when correcting for the spot-size and divergence of the beam. The best value for the M^2 in the x direction was 1.20 and in the y direction this was 1.27. These values changed whenever the shaper was realigned. More typical values for M^2 were 1.6 and 1.5 for the x and y axes, respectively. It can be imagined that within this beam profile lies an embedded diffracted-limited Gaussian beam. Compared to a diffraction-limited Gaussian beam, non-diffraction-limited beams can not be focused to the

equivalent spot size, they are M times larger:

$$w_0 = M w_0^{(1)} \tag{4.4}$$

where $w_0^{(1)}$ is the focused spot size of the diffraction limited beam ($M^2 = 1$). Since the beam quality factor is different in both planes of the beam, this must be taken into account when focusing the beam within the OPO. If M_x^2 represents the beam quality factor in the x plane, and M_y^2 represents this quantity in the y plane. Then the beam waist within the OPO should be M_x/M_y larger in the x plane than y. This then corresponds to the case of having a circular embedded Gaussian beam focused within the OPO crystal. As previously discussed, the signal beam within the OPO crystal is focused asymmetrically due to the angle of the curved mirrors. A slightly non-symmetrical pump beam would therefore produce a better spatial overlap with the signal, however, the decrease in threshold is expected to be small.

A similar argument can be made regarding the divergence of the beam in the x and y direction. The divergence half angle Θ_{Div} of the beam is M^2 greater than that of the fundamental Gaussian:

$$\Theta_{Div} = M^2 \Theta_{Div}^{(1)} \tag{4.5}$$

where $\Theta_{Div}^{(1)}$ is the divergence half angle of the fundamental. Hence, in order to eliminate astigmatism of the fundamental beam, it is required that the divergence in the x plane to be M_y^2/M_x^2 greater than the y plane.

The ModeMaster was used to carefully align the cylindrical telescope after the shaper. The device was capable of calculating key parameters with little user intervention, these include the astigmatism of the beam, the waist asymmetry (at the focus within the ModeMaster), and divergence asymmetry.

The light from the pulse-shaper is focused into the OPO, which is approximately 1.5 meters away. It is important to eliminate spatio-temporal effects that can ruin any future experiment. One of these effects can be observed at the focus of the OPO crystal; the beam is seen to be transversely translated by a few micrometers when varying phases are put to the SLM. This translation was detected at the focus of the OPO crystal using a silicon CCD camera. This translation effect has been documented and explored by Tanabe et. al. [33]. To eliminate it relay optics are used to relay the image of the beam at the last grating surface, to the

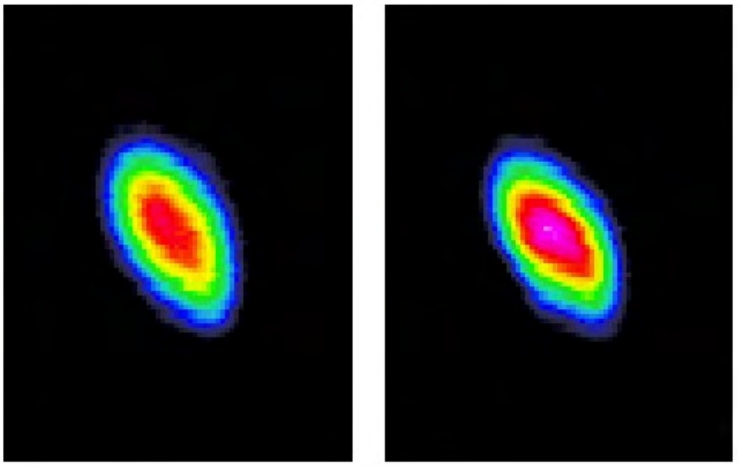

FIGURE 4.13: Pictures showing spatial profile of beam at the focus of the OPO crystal. Profile on the left is for the case of no phase profile on the SLM, and the right profile corresponds to the case of a phase profile put to the SLM to reduce the temporal pulse width of the beam. No discernable movement of the spot can be seen using a beam camera. The spot size's are approximately 29 μm in the horizontal plane.

image-plane at the OPO crystal. The relaying-optics consisted of three telescope arrangements. Hence, the first telescope arrangement after the shaper therefore served two purposes, one to correct for beam size and divergence, and the second to act as one of the relay telescopes. The other two telescopes consisted of spherical lenses, which could have been replaced with a single telescope, but sufficient focal length lenses were not available to make this possible. With the relay optics in place, no transverse translation of the beam at the OPO focus can be detected on a beam camera. Figure 4.13 shows images, as seen on the beam camera, showing the shape of the focused beam at the position of the OPO crystal, for the case of no phase on the SLM, and for a phase profile that compresses the temporal duration of the pulse by about 4 times its original duration. It can be seen there is relatively little change in the spatial profile of the beam.

4.5.3 Search Algorithms

The two search algorithms investigated were a publicly available genetic algorithm (GA) called GALib 2.4.4 [34], and a inhouse-built simulated annealing code that was a simplified version of the publicly available Adaptive Simulated Annealing

code written by Lester Ingber [35, 36]. The simulated annealing (SA) code was preferred due to it simplicity. The algorithms used are discussed, however it is important to remember that any number of suitable algorithms could have been used as the search algorithm.

4.5.3.1 Genetic Algorithm

The basics of a genetic algorithm have already been covered in chapter one. To recap, a GA consists of a population of possible solutions; with the individual solutions being called genomes. The solution/genome does not have to be a single real number, there are a number of methods to represent the solution. A popular method involves representing the genome as an array of objects, common object are either bits, integers, real numbers, or characters. Each object within the array is called a gene and typically several genes make up a genome. The process of running the GA is called evolving, but before it can evolve the genomes in the population must be initialised. Often this is performed by simply allowing them to have random values (within a set of allowed values). The randomly initialised genomes must then be evaluated for 'fitness'. This involves testing the genomes, this can involve anything from putting the genome to some hardware (as in our case), or evaluating a mathematical function. The value obtained from the evaluation is called the objective parameter. The objective parameter can be scaled and the final value is called the fitness value/parameter. Scaling is sometimes advantageous as it alters the search space seen by the GA. In some cases there is no scaling, and the fitness parameter is the same as the objective parameter.

The process of the GA consists of selecting genomes to undergo cross-over (mating) and mutation. The genomes selected for cross-over are called the parents, and the new genomes produced by this procedure are called children. Mutation is effectively an asexual reproduction involving mutation of a gene, or many genes. Once again the offspring of mutation is called a child and the original genome is called the parent.

Once the selected genomes have undergone cross-over and mutation, they are evaluated for fitness. As new children are produced a replacement method is required to determine how the children are accommodated into the population. The new population is called a new generation. The GA involves evolving the population over many generations. A stopping/termination criteria for the GA

can consist of allowing the GA to run for a preset number of generations, or until the population has converged to some value.

The genetic algorithm investigated (GALib) consisted of a comprehensive codebase, which could depict a great variety of optimisation schemes. A few highlights of the code are mentioned below:

1. Four random number generators.
2. Algorithm can be used with PVM (parallel virtual machine) to evolve populations and/or individuals in parallel on multiple CPUs.
3. Genetic algorithm parameters can be configured from file, command-line, or by modifying the source code.
4. Overlapping (steady-state GA) and non-overlapping (simple GA) populations are supported. With the user being able to specify the amount of overlap (% replacement). The code includes examples of other derived genetic algorithms such as a genetic algorithm with sub-populations and another that uses deterministic crowding.
5. Built-in termination methods to stop the code include number-of-generations and convergence of the whole or part of the population, or a new criteria can be coded by the user.
6. Speciation can be done with either DeJong-style crowding [37] (using a replacement strategy) or Goldberg-style sharing [37] (using fitness scaling).
7. Elitism is optional for non-overlapping genetic algorithms.
8. Built-in replacement strategies (for overlapping populations) include replace parent, replace random, replace worst. Or a custom made replacement operator can be implemented
9. Built-in selection methods include rank, roulette wheel, tournament, stochastic remainder sampling, stochastic uniform sampling, and deterministic sampling. Or a customised selection operator can be implemented.
10. Built-in chromosome types include real number arrays, list, tree, 1D, 2D, and 3D arrays, 1D, 2D, and 3D binary string. The binary strings, strings, and arrays can be variable length. The lists and trees can contain any object in their nodes. The array can contain any object in each element.

11. All chromosome initialisation, mutation, crossover, and comparison methods can be customised.

12. Built-in initialisation operators include uniform random, order-based random, and initialise-to-zero.

13. Built-in mutation operators include random flip, random swap, Gaussian, destructive, swap subtree, swap node.

14. Built-in crossover operators include partial match, ordered, cycle, single point, two point, even, odd, uniform, node- and subtree-single point.

15. Objective functions can be population- or individual-based.

Detailed information on each of the various attributes of the code can be found in the user manual that accompanies the code [34]. Clearly numerous GA schemes could have been used. Choosing an appropriate scheme is still very much an art. A good scheme should be capable of exploration (broad search) and exploitation (local search) of the search space. It is not uncommon for a GA to be run within a GA, in order to look for the best optimisation scheme for the problem at hand. This method is clearly very computationally intensive, but it does have the advantage of being simple to automate. Ultimately, there is no definitive guide in determining the best scheme, but some common sense helps in the matter. Numerous schemes were tested using simple experiments, such as the one to be described soon, and it was found that the good schemes generally included the following properties:

1. The genomes were coded as a 1D array of real numbers. In the case of optimising four coefficients, these numbers corresponded to the coefficients being optimised.

2. Each gene had a range of values it could take, these values were set by the problem being solved. For example, if we were compensating for dispersion of a pulse as it propagates through a length of fibre it would be expected that the fourth order dispersion, to be of orders of magnitude lower than group velocity dispersion. It would therefore make sense to appropriately limit the range of values that the fourth order dispersion can take.

3. The genomes were initialised using a random number generator. The random number generator chose values for each gene with a uniform probability within the limits of acceptable values.

4. Individuals from the population were selected for mating using a roulette wheel selection (sometimes called fitness proportionate selection). In this type of selection the fitness values of each genome is used to metaphorically construct a roulette wheel, with slots weighted in proportion to the genomes fitness. The probability of genome i being selected from a total of N genomes is then given by $p_i = f_i / \sum_{j=1}^{N} f_j$, where f_i is the fitness of the genome. This type of selection method favours fitter genomes for reproduction, but still allows a chance for less fit genomes to be mated and therefore maintains the genetic diversity.

5. A single point cross-over operator was used for mating of two genomes. This involved randomly choosing a point in the genome array and swapping all genes from this point onwards with the same part from the other genome. The result was two new child genomes.

6. The mutation operator consisted of randomly choosing a genome. Then choosing a gene within that genome. Finally, stochastically changing the value of the gene with a Gaussian probability centred about the current value.

7. Objective function consisted of converting a genome to an array of voltage drive levels which were sent to the SLM. A voltage was then recorded from a photodiode and this value was used as the objective function. The task of the GA was to maximise this value. Each genome was evaluated individually and assigned a fitness parameter.

8. Goldberg simple GA was used as the replacement operator (for more details about this operator and for a good introduction to GAs see reference [37]). In this operation the children always replace the parent, irrespective of their fitness value. Two popular alternatives to this operation involve a 'steady-state GA' in which a certain percentage of the population consists of the parents and the rest the children. The other popular alternative is the so called 'incremental genetic algorithm'. This operation allows for a great variety of replacement operators to be used, for example the newly generated children could only replace their parents if they have a higher evaluated fitness value, or replace random individuals in the population, or replace individuals that are most like them, or replace the best/worst individuals in a population, and so forth. There are other, more specialised replacement operators/schemes

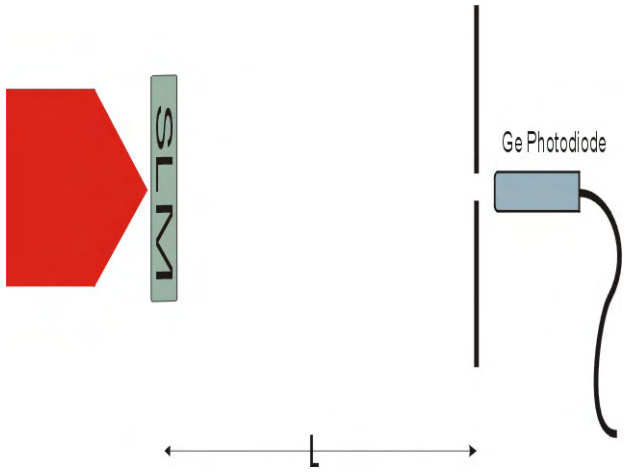

FIGURE 4.14: Schematic diagram of the lensing experiment

that can be used, these involve 'deterministic crowding' (Speciation) which maintains different species of individuals during the evolution. This can be advantageous in the case of multiple good solutions within the search space, as it allows groups of individuals to converge to the various best solutions. And finally, multiple populations and migration between populations can be implemented. Although this last scheme is best suited to a GA running on multiple CPU's, which is not the case in our situation. The Goldberg simple GA was used because it afforded some noise immunity to the code, as is discussed later.

9. The stopping criteria consisted of the number of generations, or when the fitness values of the population are quite similar.

A very simple experiment was chosen to investigate the GA. This involved using the SLM to spatially modulate light (as opposed to using it within a temporal pulse shaping apparatus). The experiment involved using the SLM to adaptively simulate a lens. In the experiment the laser beam was expanded parallel to the optics bench using a cylindrical telescope arrangement, the SLM focused this collimated beam of light through a thin slit with a photodetector immediately behind it (figure 4.14). The feedback for the GA was to optimise the voltage on the detector. This is best achieved if the SLM focuses the light through the slit, in effect behaving like a lens. The test was simple but it allowed all the components of the adaptive search loop to be programmed and tested together to make a working system. Some of this involved writing code to retrieve data from the photodiode

using a data acquisition card, updating the voltage drive levels to the spatial light modulator via a GPIB interface, and finally implementing a search algorithm.

In order to simulate a lens the phase properties of the SLM are used. The maximum phase difference of the SLM with $1047\,nm$ light is 9 radians (allowing for a comfortable margin of error) and the array of liquid crystals is $12.8\,mm$ long. If the SLM was to simulate a parabolic lens, then by a simple geometric argument the minimum focal length possible is 14 meters, which is impractical. In order to reduce the focal length, only the middle 30 pixels of the SLM were illuminated by changing the cylindrical telescope before the SLM, and only these pixels were controlled by the GA. The minimum focal length is thus reduced to $0.75\,m$. Illuminating only 30 pixels inevitably produces a poor lens (by considering the Huygens Fresnel argument regarding beam propagation). But in principle there is a noticeable increase in the voltage on the detector.

For the problem of focusing light into a slit, only the parabolic Taylor coefficient of the Taylor method is needed. The phase profile was put to the hardware, the detector and slit apparatus was moved until the maximum voltage recorded on the photodiode. The phase profile was then removed from the SLM and the GA initialised. For this simple experiment the genomes in the GA consisted of a single gene which represented the parabolic term. The population size was ten and after only four generations the GA expectedly converged to a steady value which was very close to the previous value. The GA was run again, but this time with four optimisation coefficients, three of which provide the monomials for the phase profile and a new coefficient that shifts the phase profile along the length of the SLM pixel array. In this case the GA took longer to converge, seven generations till reaching a steady value. The results showed that slightly more light was collected by the photodiode. A possible explanation for why more phase coefficients produced a better result could be found by noting the earlier concern about only illuminating 30 pixels. This inevitably causes problems in "incomplete interference" between the Huygens-Fresnel "wavelets". It is possible (although not mathematically verified) that the higher order terms are causing the wavelets to interfere more favourably.

The GA was tested using different schemes, some involved simply changing the probability of mutation or crossover, others involved changing the type of operator used for the mutation, crossover, and replacement of a genome. An important issue discovered was the noise immunity afforded when using the Goldberg simple GA

method as the replacement operator. The laser used to perform these experiments was sometimes temperamental in its modelocking, this would produce occasionally unusual noise spikes when taking results, sometimes leading to a very large voltage being recorded on the photodiode. Clearly this would be unfavourable for the search algorithm since when this happens the GA records a high value fitness value for the genome that is being tested. The high fitness of this genome is undeserved and effects convergence. However, with the Goldberg simple GA the parent genomes are always replaced with the children, irrespective of the fitness of the children. As a result, a high fitness value caused by the occasional noise spikes by the laser does not significantly affect this GA scheme. Therefore, GAs can be coded to naturally compensate for occasional noisy data. It was found that the best procedure for optimising the parameters within a scheme was to start off with a very low probability of mutation for a selected genome (> 0.005) and have a relatively high probability of crossover (~ 0.6). This ensures that the code most likely converges to the global maxima, but it often takes a very long time. In order to reduce the time taken the probability of mutation should be increased in small intervals and the code run to check for satisfactory convergence.

4.5.3.2 Simulated Annealing

An issue that is often overlooked when working with search algorithms is the time taken to optimise the code, or in the case of GAs, to look for a good scheme. Comparisons between types of search algorithms often overlook this important consideration and in many instances the time taken to optimise the search algorithm can be significantly greater than the time taken to run the code, as this step is usually conducted by trial and error. In future applications of pulse shaping it is most probable that the search algorithm will be used to repetitively solve a similar set of problems. In this instance, it would be advantageous to inves time in finding a quick search algorithm. However if it is required that vastly different problems are investigated then the landscape of the search space will most likely be vastly different. In this instance, it would be better to find a robust algorithm that is not necessarily fast or even computationally efficient.

One such algorithm is simulated annealing (SA). SAs have the distinct advantage over GA in that for infinitely slow convergence they are guaranteed to converge to a solution, irrespective of the search space [36]. This makes SAs a robust choice

for use as a search algorithm. The disadvantage of SAs is that they are often far slower than competing algorithms, but there is less time taken in optimising an SA than competing algorithms such as GAs.

Simulated annealing mimics the annealing process seen when a hot liquid solidifies into a crystalline state. The key to achieving a crystalline state in its lowest energy configuration is to begin the process with a high enough temperature, thereby allowing the atoms to move freely and "sample" different energy states. Then slowly reducing the temperature, and therefore the mobility of the atoms.

Annealing is very much a statistical phenomenon, since for any given temperature the atoms have a distribution of energies. For atoms whose behaviour can be explained classically, and at quasi-equilibrium temperatures, the energy distribution of the atoms can be given by the Boltzmann distribution. Therefore, as the temperature of the system cools the atoms arrange themselves in certain configurations, some of these configurations might result in the atoms being trapped in a non-globally optimal energy minima. However, due to the statistical nature of the energy distribution of the atoms, there is always a probability that they can leave these minima. This probability decreases with the temperature, and with the energy difference between the current configuration and that of other possible configurations.

The various energy configurations of the atoms can be represented as a search space. It can be imagined that what is occurring, is that the system is moving across this search space, so as to find the global minimum. Simulated annealing performs precisely this. The SA starts with a random position in the search space, where the search space can represent any problem at hand. Then using a stochastic function it decides on the magnitude and direction in which to make its next move. The algorithm has a fictional temperature that it steadily decreases with number of iterations of the algorithm. The temperature controls the step-sizes generated by the stochastic function, and the probability that a move from one state to another is accepted.

A simple outline of the code is given, but first some parameter must be defined. The number of iterations of the algorithm is k. The function being optimised typically consists of 3 parameters, which correspond to GVD, TOD, and FOD. The value of each parameter can be represented by a_k^i, where i has the value of either 2, 3, or 4 and is used to denote GVD, TOD, or FOD. It is clear that each of

these parameters have a different characteristic range, therefore solutions in each parameters are limited to within $[A_i, B_i]$. By applying these parameters to the SLM, hardware their effect on x_k can be recorded. Finally, the temperature of the system can be given by $T(k)$. The temperature has the same units as the problem being solved, i.e. if optimising the voltage from a photodiode then the temperature is in units of volts. $T(0)$ denotes the initial temperature of the system, which is typically a few times higher than the maximum difference expected in the physical system, i.e. if it is expected that the photodiode will at best give a reading of 10 volts, then $T(0)$ might be chosen to be 40.

The outline of the code is given as follows:

1. For a given position in the search space a_k, new positions is generated for each i via the expression

$$a_{k+1}^i = a_k^i + y^i(B_i - A_i) \tag{4.6}$$

where y^i is generated from a uniform distribution u^i, which is limited in the range $u^i \in [0, 1]$

$$y^i = signum(u - \frac{1}{2})T(k)[(1 + 1/T(k))^{|2u^i - 1|} - 1] \tag{4.7}$$

where the function signum(x) is -1 when x is negative, zero when x is zero, and 1 when x is positive.

2. The new position is experimentally evaluated by applying the phase profile to the SLM and recording the response. If we let the response of the old phase profile be called x_k and the new one x_{k+1}. If $x_{k+1} > x$ then the new move is accepted, otherwise a random number, U, is chosen from a uniform distribution between $U \in [1, 0]$. The move is accepted if

$$U < \exp\left\{\frac{(x_{k+1} - x_k)}{T(k)}\right\} \tag{4.8}$$

otherwise it is rejected and the old variables retained. It can be seen that for $T(k) \to 0$ the probability of accepting a move tends towards zero.

3. The temperature of the system is reduced using

$$T(k) = T_0 \exp(-ck) \tag{4.9}$$

where c is a constant that is set by the user. In practise the best value of c is determined by trial and error. If the value of c is too high then the temperature is reduced too quickly and the algorithm gets trapped at a local minima. And a low value of c means that the algorithm takes a long time to converge to the global maxima. In practise it is sensible to estimate the highest expected value for the objective function. Then run the algorithm with a very low value for c, this increases the chance of the algorithm converging, but at the expense of time. If the time taken for convergence is too slow, the value of c should be slowly increased until satisfactory convergence is meet.

4. The iteration count k of the algorithm is increased by one, and the stopping criteria are checked. If they are not satisfied then the procedure is repeated from step 1.

The code was checked by performing optimisation tests, one of these tests involved maximising the second-harmonic generation from a thin BBO crystal.

4.6 Conclusion

This chapter has described all the apparatus used in the experiments. The laser source, consisting of the SPM fibre was able to deliver chirped pulses with $3.5\,nm$ of spectrum. Preliminary experiments conducted using the OPO and the pulses from the fibre demonstrate the ability of the OPO to be operated with these pulses, despite the increase in M^2 caused by the pulse-shaper and the pulse-front-tilt it introduces. The power available at the OPO was about $1\,W$ of average power. This is enough to operate the OPO at pump powers a few times the threshold value and therefore to achieve stable operation.

The encoding of phase profiles for the SLM is performed using a polynomial and simulated annealing is the choice of search algorithm used throughout this research. Simulated annealing is not the fastest algorithm, but less time is required to optimise it for satisfactory convergence as only one parameter needs to be modified. However, the SA has no built in mechanism to deal with noise, in comparison a GA with a suitable scheme can be made to overcome this. To transcend the effects of occasional noise spikes from the laser, the laser used in the research is carefully

tuned in order to reduce the likelihood of going out of modelocking. If the laser does leave modelocking, the SA is stopped and the test repeated.

4.7 References

[1] G. P. Agrawal, *Nonlinear fiber optics*, Optics and photonics, 3rd ed. (Academic Press, San Diego, 2001).

[2] K. Tamura, C. R. Doerr, L. E. Nelson, H. A. Haus, and E. P. Ippen, "Technique for Obtaining High-Energy Ultrashort Pulses from an Additive-Pulse Mode-Locked Erbium-Doped Fiber Ring Laser," Optics Letters **19**(1), 46–48 (1994).

[3] H. A. Haus, E. P. Ippen, and K. Tamura, "Additive-Pulse Modelocking in Fiber Lasers," IEEE Journal of Quantum Electronics **30**(1), 200–208 (1994).

[4] A. M. Johnson, R. H. Stolen, and W. M. Simpson, "80X Single-Stage Compression of Frequency Doubled Nd-Yttrium Aluminum Garnet Laser-Pulses," Appl. Phys. Lett. **44**(8), 729–731 (1984).

[5] J. P. Heritage, A. M. Weiner, and R. N. Thurston, "Picosecond Pulse Shaping by Spectral Phase and Amplitude Manipulation," Opt. Lett. **10**(12), 609–611 (1985).

[6] J. P. Heritage, R. N. Thurston, W. J. Tomlinson, A. M. Weiner, and R. H. Stolen, "Spectral Windowing of Frequency-Modulated Optical Pulses in a Grating Compressor," Appl. Phys. Lett. **47**(2), 87–89 (1985).

[7] K. M. Rosfjord, R. A. Villalaz, and T. K. Gaylord, "Constant-bandwidth scanning of the Czerny-Turner monochromator," Appl. Opt. **39**(4), 568–572 (2000).

[8] K. L. Sala, G. A. Kenneywallace, and G. E. Hall, "Cw Auto-Correlation Measurements of Picosecond Laser-Pulses," IEEE J. Quantum Electron. **16**(9), 990–996 (1980).

[9] R. Trebino, *Frequency-resolved optical gating: the measurement of ultrashort laser pulses* (Kluwer Academic Publishers, Boston, 2000).

[10] J. C. M. Diels, J. J. Fontaine, I. C. Mcmichael, and F. Simoni, "Control and Measurement of Ultrashort Pulse Shapes (in Amplitude and Phase) with Femtosecond Accuracy," Appl. Opt. **24**(9), 1270–1282 (1985).

[11] D. T. Reid, W. Sibbett, J. M. Dudley, L. P. Barry, B. Thomsen, and J. D. Harvey, "Commercial semiconductor devices for two photon absorption autocorrelation of ultrashort light pulses," Appl. Opt. **37**(34), 8142–8144 (1998).

[12] D. T. Reid, M. Padgett, C. McGowan, W. E. Sleat, and W. Sibbett, "Light-emitting diodes as measurement devices for femtosecond laser pulses," Opt. Lett. **22**(4), 233–235 (1997).

[13] P. Myslinski, "Rapid Scanning Autocorrelator for Measurements of Ultrafast Laser-Pulses," Rev. Sci. Instrum. **58**(4), 711–713 (1987).

[14] J. A. I. Oksanen, V. M. Helenius, and J. E. I. Korppitommola, "A Femtosecond Autocorrelator with Internal Calibration," Rev. Sci. Instrum. **64**(9), 2706–2707 (1993).

[15] M. V. O'Connor, M. A. Watson, D. P. Shepherd, D. C. Hanna, J. H. V. Price, A. Malinowski, J. Nilsson, N. G. R. Broderick, and D. J. Richardson, "Synchronously pumped optical parametric oscillator driven by a femtosecond mode-locked fiber laser," Opt. Lett. **27**(12), 1052–1054 (2002).

[16] S. D. Butterworth, P. G. R. Smith, and D. C. Hanna, "Picosecond Ti:sapphire-pumped optical parametric oscillator based on periodically poled LiNbO3," Opt. Lett. **22**(9), 618–620 (1997).

[17] S. D. Butterworth, V. Pruneri, and D. C. Hanna, "Optical parametric oscillation in periodically poled lithium niobate based on continuous-wave synchronous pumping at 1.047 mu m," Opt. Lett. **21**(17), 1345–1347 (1996).

[18] V. Pruneri, S. D. Butterworth, and D. C. Hanna, "Low-threshold picosecond optical parametric oscillation in quasi-phase-matched lithium niobate," Appl. Phys. Lett. **69**(8), 1029–1031 (1996).

[19] S. D. Butterworth, M. J. Mccarthy, and D. C. Hanna, "Widely Tunable Synchronously Pumped Optical Parametric Oscillator," Opt. Lett. **18**(17), 1429–1431 (1993).

[20] M. J. Mccarthy and D. C. Hanna, "All-Solid-State Synchronously Pumped Optical Parametric Oscillator," J. Opt. Soc. Am. B: Opt. Phys. **10**(11), 2180–2190 (1993).

[21] M. J. Mccarthy and D. C. Hanna, "Continuous-Wave Mode-Locked Singly Resonant Optical Parametric Oscillator Synchronously Pumped by a Laser-Diode-Pumped Nd-Ylf Laser," Opt. Lett. **17**(6), 402–404 (1992).

[22] D. C. Hanna, M. V. O'Connor, M. A. Watson, and D. P. Shepherd, "Synchronously pumped optical parametric oscillator with diffraction-grating tuning," J. Phys. D **34**(16), 2440–2454 (2001).

[23] K. Puech, L. Lefort, and D. C. Hanna, "Broad tuning around degeneracy in a singly resonant synchronously pumped parametric oscillator by means of a diffraction grating," J. Opt. Soc. Am. B: Opt. Phys. **16**(9), 1533–1538 (1999).

[24] S. J. Brosnan and R. L. Byer, "Optical Parametric Oscillator Threshold and Linewidth Studies," IEEE Journal of Quantum Electronics **15**(6), 415–431 (1979).

[25] S. Guha, "Focusing dependence of the efficiency of a singly resonant optical parametric oscillator," Appl. Phys. B **66**(6), 663–675 (1998).

[26] D. Hanna, "Astigmatic Gaussian beams produced by axially asymmetric laser cavities," IEEE J. Quantum Electron. **5**(10), 483 (1969).

[27] M. J. Dodge, "Refractive Properties of Magnesium Fluoride," Applied Optics **23**(12), 1980–1985 (1984).

[28] D. H. Jundt, "Temperature-dependent Sellmeier equation for the index of refraction, n(e), in congruent lithium niobate," Opt. Lett. **22**(20), 1553–1555 (1997).

[29] H. P. Sardesai, C. C. Chang, and A. M. Weiner, "A femtosecond code-division multiple-access communication system test bed," J. Lightwave Technol. **16**(11), 1953–1964 (1998).

[30] A. M. Weiner, "Femtosecond Optical Pulse Shaping and Processing," Prog. Quant. Electron. **19**(3), 161–237 (1995).

[31] J. Turunen and F. Wyrowski, *Diffractive Optics for Industrial and Commercial Applications*, 1st ed. (Akademie Verlag, Berlin, 1997).

[32] A. M. Weiner, "Femtosecond pulse shaping using spatial light modulators," Rev. Sci. Instrum. **71**(5), 1929–1960 (2000).

[33] T. Tanabe, F. Kannari, F. Korte, J. Koch, and B. Chichkov, "Influence of spatiotemporal coupling induced by an ultrashort laser pulse shaper on a focused beam profile," Appl. Opt. **44**(6), 1092–1098 (2005).

[34] *http://lancet.mit.edu/ga* (2007).

[35] L. Ingber, "Very Fast Simulated Re-Annealing," Mathematical and Computer Modelling **12**(8), 967–973 (1989).

[36] L. Ingber, "Simulated Annealing - Practice Versus Theory," Mathematical and Computer Modelling **18**(11), 29–57 (1993).

[37] D. E. Goldberg, *Genetic algorithms in search, optimization, and machine learning* (Addison-Wesley Pub. Co., Reading, Mass., 1989).

Chapter 5

Adaptive Control of an Optical Parametric Oscillator

This chapter demonstrates adaptive computer control of an OPO. The experiments successfully show the ability to minimise the threshold of an OPO via optimisation of the signal power. Control of the idler pulse shape is also demonstrated via optimisation of two-photon-absorption.

5.1 Optimisation of OPO Threshold

This experiment shows adaptive control over the SPOPO by minimisation of the threshold. This was achieved by maximising the signal power recorded by an InGaAs photodiode. Factors that affect this experiment are most obviously changes in the spatial characteristics of the beam; these include a change in the spatial chirp, changes in the spatial profile of the beam, and translation of the beam. These spatial effects change the overlap between the pump and signal beam and therefore affect the threshold and efficiency of the OPO. Spatial effects have broadly been satisfied by using relay optics, as discussed in the previous chapter. Another issue that invalidate the claim of maximising signal power to minimise threshold is if the OPO is pumped many times above threshold. In such a situations, nonlinear effects other than our desired DFG become apparent. One of these is back conversion of the signal and idler photons back into a pump photon. Other issues such as SPM become significant with even higher pumping powers.

With 4 ps pump pulses (as seen in figure 4.12) and a 95% reflective output coupler (O/C) the power into the OPO was adjusted so it operated about two times threshold. The signal power from the reflective O/C was used as feedback to the SA. A polariser and half-wave plate were placed before the SPOPO in order to vary the power into the setup and determine the threshold.

The threshold of the OPO with $\sim 4\,ps$ chirped pulses and no phase across the SLM was measured to be 100 mW with all high reflectors. A photodiode was used to determine the average power of the signal beam. This information was conveyed to the computer via a data acquisition card, National Instruments PCMCIA DAQCard-1200, where it was used by the SA as the objective function. The task of the SA was to maximise the voltage on the photodiode by applying different phase profiles to the SLM. It sent the phase profiles (voltage drive levels) to the SLM via the attached GPIB interface (National Instrument PCMCIA-GPIB). The SA was run for 500 iterations; this was plenty of iterations to allow it to converge to a steady power level. Once this was achieved, the power into the OPO was decreased in order to determine its threshold, and then it was increased for the next measurement. The output coupler was removed and replaced with a highly reflective mirror (for the signal wavelength). The angle and distance of the mirror was adjusted until the OPO was oscillating and the minimum threshold of the OPO determined. Allowing the SA to optimise the signal power lead, to a threshold value of 42 mW with all high reflectors. The retrieved phase co-efficients were $a^2 = -0.780\,ps^2$, $a^3 = -0.0376\,ps^3$, $a^4 = 0.1357\,ps^4$ and correspond to the adaptively optimised phase profile shown later in figure 5.1.

It is expected that for this particular test the shortest pump pulse width will maximise the signal power output, and therefore achieve the lowest threshold. Since the spectrum and phase profile of the pump pulse is due to SPM, it is possible to determine both these parameters using a numerical model. The propagation of pulses through an optical fiber has been examined in great detail [1] and computer programs which model pulse propagation are available. A program called Propulse written by Dr Rüdiger Paschotta was used. By inputting typical parameters for our setup it was possible to display the correct spectral broadening and give a theoretical phase profile for the pulse (Figure 5.2a). Propulse was further able to compress the pulse to a minimum by compensating for up to fourth order dispersion (Figure5.2b). The phase coefficients from Propulse can be directly applied to the SLM to compress the pump pulse experimentally. By performing

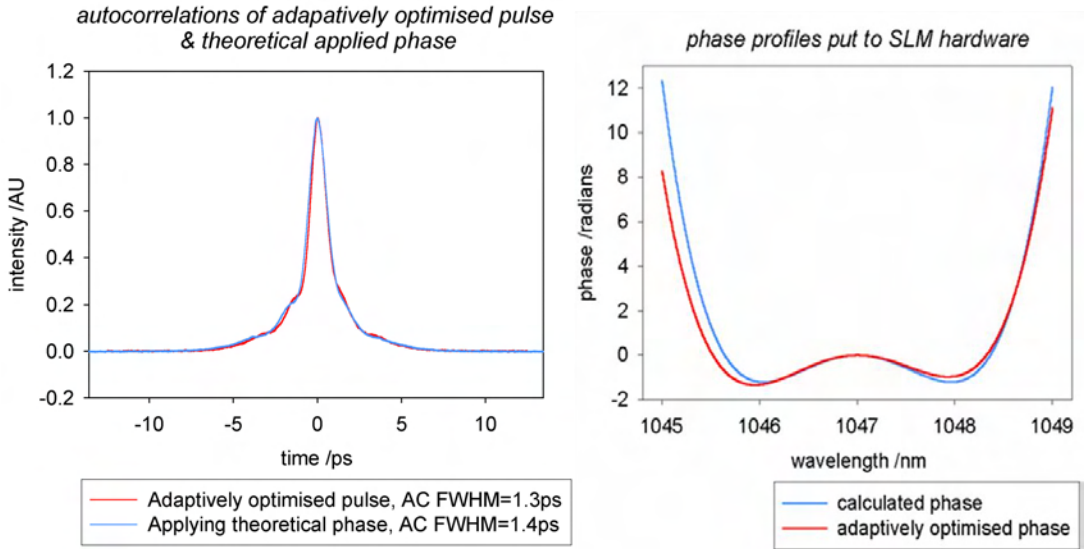

FIGURE 5.1: Graph on left showing the autocorrelation trace of the adaptively optimised pulse (red line) and pulse profile determined by applying a theoretical phase to the SLM (blue line). Figure on the right showing the phase profile put to the SLM hardware for the two pulses.

this, the threshold of the OPO was found to be 48 mW for high reflectors. It is clear that the theoretical phase profile has performed worse than the adaptively optimised pulse, which achieved a 42 mW threshold.

Figure 5.1 shows the experimental autocorrelations of the adaptively optimised pump pulse and that for the application of the theoretical phase profile. It can be seen that the pulse widths are very similar, but the theoretically optimum pulse is slightly wider. This could be caused by incorrect alignment of the shaper; or it could be caused by deviations from the fibre model. One such discrepancy can be seen by comparing the spectrum after the fibre (figure 4.3) to that produced by

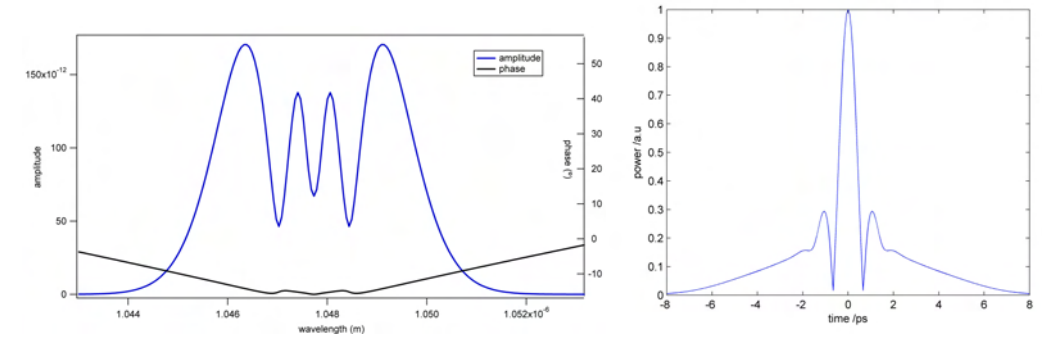

FIGURE 5.2: Image on the left shows the theoretical spectrum and phase after propagation through the fibre. Figure on the right shows an autocorrelation for a theoretical pulse which been compressed by compensating for up to 4th order dispersion.

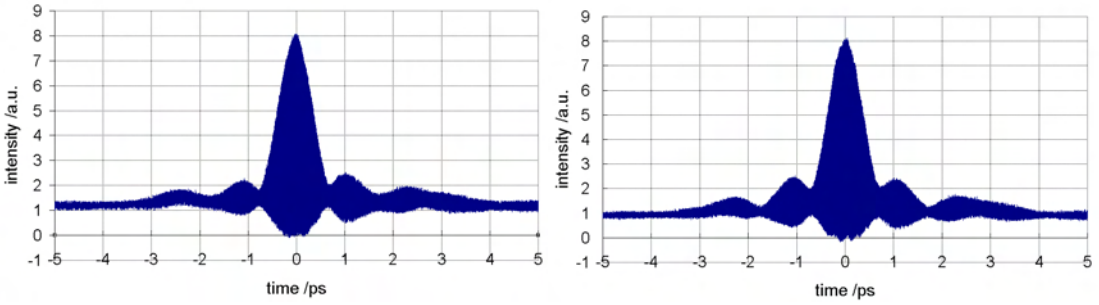

FIGURE 5.3: Left graph shows the adaptively optimised idler pulse IAC, right graph shows the IAC of the theoretically compressed idler pulse

Propulse (figure 5.2). In practise the spectrum generated from our fibre system is rarely symmetric, which indicates that the phase profile across it differ from the theoretical phase profile. The theoretical phase profile can also be affected by an incorrect transverse positioning of the SLM. This is because the theoretical phase model assumes that the central wavelength for the phase profile is 1047 nm; therefore the SLM has to be careful positioned so that the middle pixel corresponds to this wavelength. In order for the SLM to be position correctly requires it to be transversely translated to the incoming beam to within the width of one SLM pixel, which is 100 μm. A systematic error could cause the correlation of pixel to spectrum to be incorrect. But with the use of an adaptive feedback loop, this sort of error does not affect the operation of the experiment.

The mid-infrared idler autocorrelations for the two pulses are taken, these are shown in Figure 5.3. The lack of a distinguished pedestal underneath the pulses indicates that the idler pulses have little to no chirp. The pulses do however show

side-lobes on the main pulse. These are thought to reflect the real pulse shape of the idler and are quite possible for a bandwidth-limited pulse with a complex structured spectrum, as is the case here.

5.2 Control of Mid-Infrared Idler Pulse Shape via Two Photon Absorption

Adaptive control of mid-infrared pulse shapes is highly desirable for many possible future applications of this research. In this section, an adaptive learning experiment similar to the previous signal optimisation is described. In this experiment, two photon absorption within an extended InGaAs detector is optimised. The band-gap of the photodiode is greater than the energy supplied by one idler photon. However, if the energy of two idler photons is greater than the band-gap, then for a highly intense beam it is possible for an electron in the valence band to simultaneously absorb two photons and therefore have enough energy to reach the conduction band and register a current. Sharma et. al. [2] state that for an ideal photodiode the relationship between the current produced due to two-photon absorption I_{TPA} and the peak power of the laser pulse P is given by:

$$I_{TPA} = \xi P^2 \tag{5.1}$$

Where ξ defines the two-photon induced photo-current response in ampere/watt^2. Hence, for this particular test it is predicted that idler pulses with the highest peak powers will optimise the current produced by the diodes. Equation 5.1 ignores the spatial properties of the beam and care is taken to ensure that the spot-size of the beam on the photodiode is the same.

The experiment consisted of operating the OPO with a 65% reflective O/C. The higher O/C was chosen so that the OPO could be operated with more power, but with a larger loss for the signal beam. The larger signal loss reduces the number of times threshold the OPO is operating at, this makes back-conversion of the signal and idler back into a pump photon less likely. Therefore, more power from the idler can be generated. The idler from the OPO was focused into an extended InGaAs detector. In order to not saturate the photodiode a simple preliminary test was performed. It is expected that the TPA process is maximised when a pulse similar

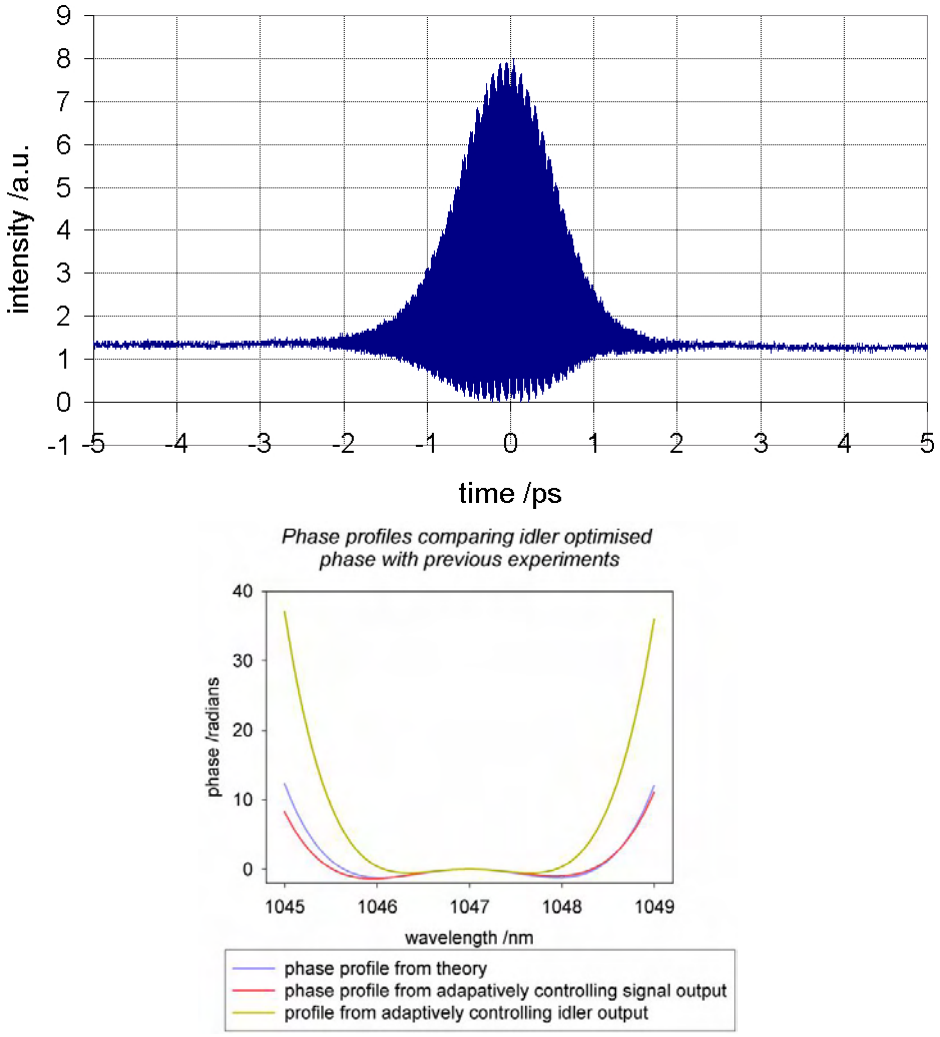

FIGURE 5.4: Left graph showing interferometric autocorrelation of the adaptively optimised TPA idler pulse. Right figure showing the phase profile of the TPA optimised pulse. For comparison the previous phase profiles are also displayed.

to the adaptively compressed pulse from the last experiment is introduced. This pulse was applied and the diode response measured. Filters were used to reduce the power into the diode to ensure that the device would not be saturated for the case of a compressed idler pulse. The compressed pulse phase was then removed from the SLM and the OPO operated at 50% above the threshold value with the 65% reflective O/C.

Figure 5.4 shows the idler IAC for the TPA optimised test after 500 iterations of the SA, which took just over two minutes to complete. Comparisons with the signal optimisation experiment show that the idler optimised pulse is much cleaner, it has no side lobes, but it is slightly wider. The TPA optimised pulse has

a high peak power and most of the energy in the main pulse, and this increases the probability of an electron absorbing two idler photons.

5.3 Adaptive Mid-IR Double Pulse Formation

Within this final mid-infrared adaptive experiment the formation of double idler pulses are shown. The setup utilises the idler autocorrelator setup described in section 4.2.2; the previous figure 4.5 shows the setup used in this experiment.

In the experiment the speaker is disabled and the "fixed mirror" (see figure 4.5) is adjusted so that the maximum voltage is recorded from the diode. From this position, the mirror is moved away by a few tens of microns, resulting in a decrease in the voltage. It is expected that the most likely way to increase the voltage on the photodiode is for the SA to produce an idler pulse which consists of two pulses separated in time by and an amount related to the distance the fixed mirror was moved by. The OPO was operated at four times threshold using a 65% reflective O/C and for the case of no phase profile on the SLM. The relatively high power into the OPO was required since it is likely that a double pulse has a higher threshold, the larger reflective O/C was again chosen for the same reasons given in previous section.

The voltage from the photodiode is passed through an amplifier and is used as the feedback for the SA, which is run for 500 iterations. Figure 5.5 shows the interferometric autocorrelation for the pulses that optimised this experiment. The graphs are for various displacements of the fixed mirror. It can be seen that a double pulse is formed, furthermore the double pulse shows no sign of chirp. This could be because the TPA process is dependent on peak power and an unchirped pulse will always have a higher peak power than a chirped pulse. This demonstration shows the feasibility of using adaptive control techniques in the formation of double pulses of arbitrary separation. In principle the time separation between the pulses can be increased further, but in practise this requires more power to be delivered to the OPO.

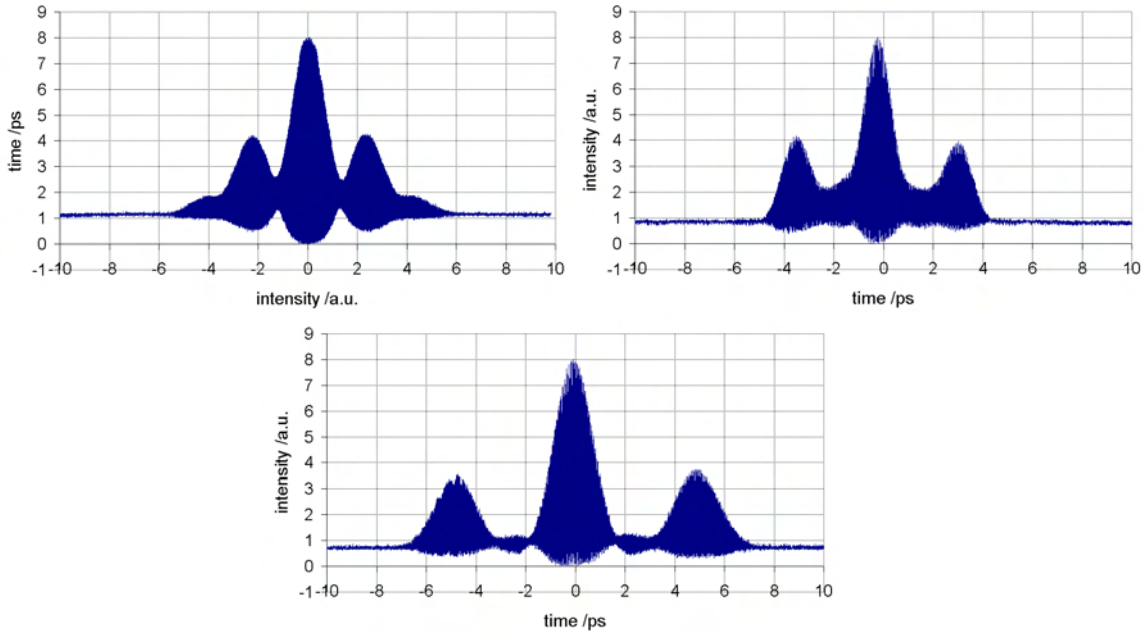

FIGURE 5.5: Experimental data for idler double pulse formation. From the top left going clockwise the displacement of the fixed mirror is increased.

5.4 Conclusion

This chapter has successfully demonstrated the adaptive control of an OPO via signal, and idler optimisation. These techniques can be extended for specific end applications. Only spectral phase modulation of the pump pulse has been used to demonstrate these results. In order to obtain more control in the mid-infrared amplitude modulation of the pump pulse is required. SLMs capable of phase and amplitude modulation are commercially available. However, simply controlling the phase and amplitude of the pump pulse is not enough to achieve complete control over the idler pulses. What is required, is control over the signal pulse in order to increase the fidelity of the transfer from the near- to mid-infrared. Control of the signal could extend the types of future adaptive applications and possibly increase the convergence of a feedback loop.

In the next section shaping of the signal is looked at with the aim of improving the fidelity of the spectral transfer from the pump to the idler.

5.5 References

[1] G. P. Agrawal, *Nonlinear fiber optics*, Optics and photonics, 3rd ed. (Academic Press, San Diego, 2001).

[2] A. K. Sharma, M. Raghuramaiah, P. A. Naik, and P. D. Gupta, "Use of commercial grade light emitting diode in auto-correlation measurements of femtosecond and picosecond laser pulses at 1054 nm," Opt. Commun. **246**(1-3), 195–204 (2005).

Chapter 6

Pulse Shape Transfer

It has been shown that adaptive control can result in optimisation of experiments in the mid-infrared. These included double-pulse formation, and optimisation of two photon absorption in a photodiode. However adaptive control over a standard OPO is not enough to guarantee the formation of arbitrary pulse shapes in the mid-infrared. This is because the OPO has characteristics that limit the type of pulses it can produce. These limitations can potentially result in a learning loop not being able to optimise a mid-IR experiment because the optimal pulse shape can not be generated by the OPO. Ideally, what is required for mid-IR light is the electrical equivalent of the arbitrary waveform generator (AWG). The AWG has proved itself to be of enormous flexibility and has found numerous uses in electrical and electronics studies. If it was possible to synthesis a similar device for the mid-IR then this could have a similar effect for mid-IR experimentation. With the flexibility of a mid-IR AWG, a learning loop would not be limited to finding solutions that the OPO can produce. The key to such a mid-IR AWG is high fidelity transfer of pulse shapes from the near-IR to the mid-IR.

It has been seen from the theory section that a temporally broad signal pulse and $\Delta k = 0$ are required for high fidelity transfer. Prawiharjo [1] has modelled the pulse transfer process in great detail using both numerical and analytical techniques. The analysis includes a time delay τ between the pump and signal, and assumes no z dependence in the nonlinear coefficient, d, because of the use of

standard uniform poled grating. Therefore equation 2.18 can be shown to be:

$$A_i(L,\Omega_i) = -i\gamma_i d \int_0^L dz \int_{-\infty}^{\infty} d\Omega_s \hat{\mathbf{A}_\mathbf{s}}^*(\Omega_s)\hat{\mathbf{A}_\mathbf{p}}(\Omega_i+\Omega_s)\exp(i\tau\Omega_s)\exp[i\Delta k(\Omega_s,\Omega_i)z] \tag{6.1}$$

Prawiharjo et. al. [1] shows that the best pulse shaping fidelity is achieved when GVM between pump and idler, $\delta\nu_{pi}$, is zero. In this situation equation 6.1 becomes a convolution between the pump and what is known as the effective signal $\hat{\mathbf{A}_\mathbf{e}}(\Omega_s)$:

$$A_i(L,\Omega_i) = \int_{-\infty}^{\infty} d\Omega_s \hat{\mathbf{A}_\mathbf{e}}(\Omega_s)\hat{\mathbf{A}_\mathbf{p}}(\Omega_i+\Omega_s) \tag{6.2}$$

where the effective signal is defined as:

$$\hat{\mathbf{A}_\mathbf{e}}(\Omega_s) = i\gamma_i sinc\left[\delta\nu_{ps}\Omega_s\frac{L}{2}\right]\hat{\mathbf{A}_\mathbf{e}}^*(\Omega_s)\exp\left[i\left(\tau+\frac{\delta\nu_{ps}L}{2}\right)\Omega_s\right] \tag{6.3}$$

It can be seen that the effective signal consists of the signal spectrum multiplied by a sinc function and an imaginary exponential. The effect of the sinc function is actually advantageous for pulse transfer since its effect is to narrow the spectrum of the signal. For our setup, the situation for $\delta\nu_{pi} \simeq 0$ occurs when the signal wavelength is at $1.5\,\mu m$ and this gives a group velocity mismatch between the pump and signal of $\delta\nu_{ps} = 100\,fs/mm$. Using these numbers and a crystal length of $10.7\,mm$ it can be found that the FWHM bandwidth of the sinc function is about $2\,THz$, which corresponds to $15\,nm$ at the wavelength of the signal. Furthermore, the time delay, τ, can be used to compensate for the GVM between pump and signal.

The fidelity of the transfer at a signal wavelength of $1.5\,\mu m$ is examined. It is shown that for $\delta\nu_{pi} \simeq 0$ the signal pulse is bandwidth limited and shows no sign of the pump spectral shape, whereas for a non zero GVM the signal spectrum begins to obtain some of the pump shape and the idler spectrum becomes less like the pump. It is shown by Prawiharjo et. al. [1] that for the parameters used here, there is an idler range of $1\,\mu m$ where good spectral transfer can be achieved. Within this range lies a number of organic vibrational bonds. If wavelengths beyond the good spectral transfer regime are required, then the wavelength of the pump laser can be changed in order to adjust the idler wavelength such that $\delta\nu_{pi} = 0$ is still the case, therefore different idler wavelengths are obtainable. Alternatively aperiodically poled material (QPM engineering) [2] could be used, or a critical phase-matching

scheme involving spatial walk-off with pulse-front tilt [3], both of these techniques are mentioned in reference [1].

6.1 Standard SPOPO at 1.5 μm and Cavity Length Tuning

As stated earlier for good transfer the signal spectral bandwidth must be less than the pump. Therefore, spectrally narrowing optics such as etalons and a birefringent filter were investigated inside the SPOPO cavity. Furthermore, the signal should be spectrally symmetric so as to not affect the idler spectrum due to the interaction of the signal and pump spectra. The signal pulse should also be free of any chirp so as to preserve the transfer of the chirp from the pump to the idler pulse. It was experimentally found that these last two requirements were easily fulfilled by operating the OPO with a signal wavelength of 1.5 μm (i.e. in the $\delta\nu_{pi} \backsimeq 0$ regime). At this wavelength the signal time-bandwidth product did not change with variation of power into the OPO, and variations in the cavity length of the OPO. These two points are elaborated in the next paragraphs.

Figure 6.1 shows characteristics of the signal versus the number of times threshold at which the OPO was operated. The signal light was extracted using an 85% output coupler. The signal spectral bandwidth was recorded from an optical spectrum analyser, OSA (HP 86140B) and autocorrelation traces of the signal were collected. The pulse duration is calculated from the autocorrelation trace and a Gaussian pulse shape assumed. The spectrum of the signal was Gaussian-like irrespective of the number of times threshold the OPO was operated at. This fulfils one of the previous criteria for the signal. It can further be seen that the time-bandwidth product of the pulse is $\sim$0.5 and remains constant with increasing power into the OPO. The results of this test show that when the signal wavelength is 1.5 μm we can be confident of varying the power into the OPO and not worry about causing a non-symmetric or chirped signal pulse.

As mentioned before, cavity tuning may be required to achieve optimum transfer fidelity and so it is important to observe any changes in the signal characteristics with cavity length. An estimation of the required cavity length detuning can be made using equation 6.1 and some simplifications, such as ignoring terms higher than GVD, and assuming that the bandwidth of the pump, signal, and idler are

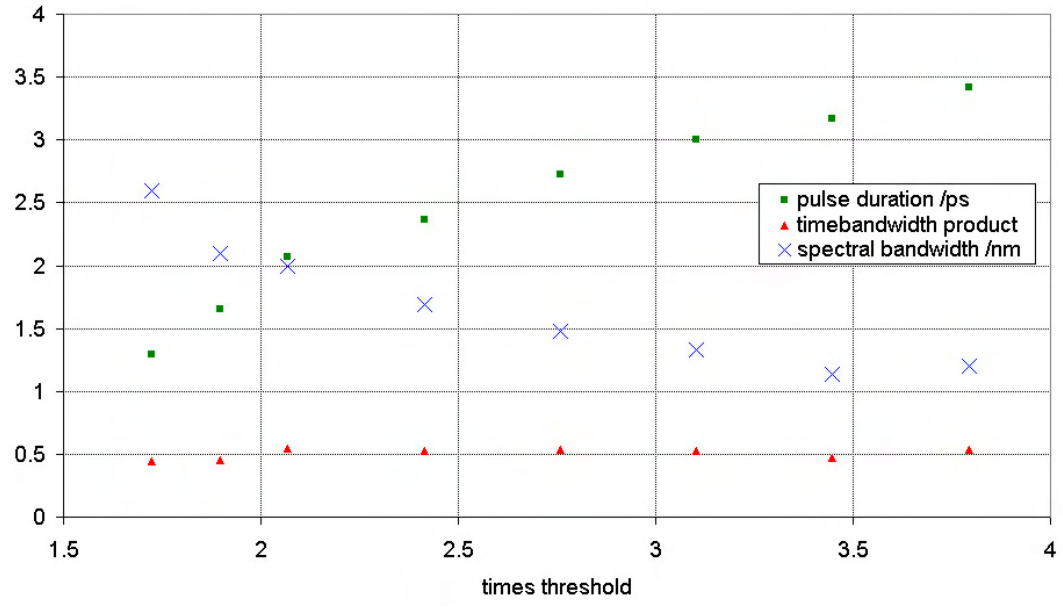

FIGURE 6.1: Signal characteristic with number of times threshold. The pulses entering the SPOPO are ~4ps in duration and chirped. An 85% output coupler is used to extract the signal.

the same. In practise, this last point is not necessarily true and depends on a number of factors, including the number of times threshold the OPO is operating [4], and whether there are any spectrally restrictive optics within the OPO. The assumption is generally accurate to within an order of magnitude, and for the purposes of this exercise only order of magnitude estimates are required. Therefore the requirement that equation 6.1 approaches a convolution between pump and signal requires that:

$$\tau \approx (\delta\nu_{ps} + \delta\nu_{pi})L \tag{6.4}$$

where L is the length of the crystal. The estimated value of τ is of a few picoseconds, which in terms of cavity length changes represents a few hundreds of micrometers. This distance can be easily adjusted by placing one of the flat mirrors in the OPO on a translation stage, and adjusting the stage using a micrometer screw-gauge. However, it is experimentally difficult to know where the signal pulse is in relation to the pump. In principle, using a fast photodiode, this could be directly measured using signal leakage at the curved mirror where the pump is transmitted. But fast enough photodiode were not available. This limitation makes a comparison of the pump-signal delay between theory and practise impractical. For this reason the analysis is restricted to qualitative agreements.

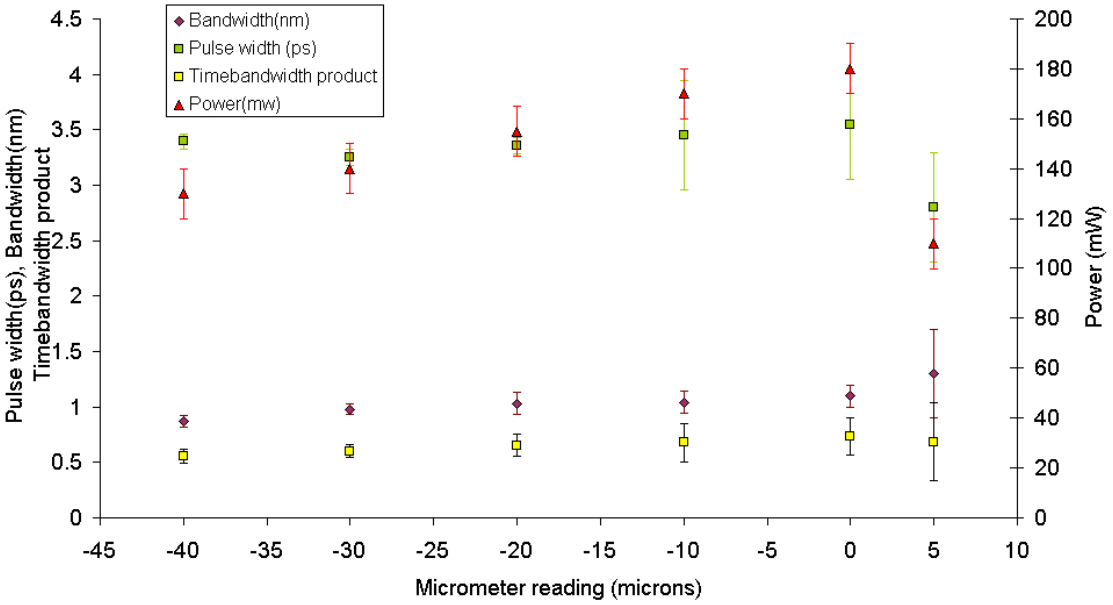

FIGURE 6.2: Experimental data showing variation in the signal parameters with relative changes in the length of the cavity. The OPO had an 85% reflective O/C for the signal and was operated 3.6 times this threshold value. The zero micrometre value corresponds to the case of minimum threshold (highest output power). A Gaussian shape for the signal pulse shape is assumed.

Figure 6.2 shows characteristics of the signal at $1510\,nm$ and how it varies with relative changes in the cavity length. The OPO had an 85% reflective output coupler and the OPO was pumped at a fixed power during the whole of the operation. With the output coupler, this pump power corresponds to 3.6 times the minimum threshold of the OPO. The zero distance on the graph corresponds to the case of lowest OPO threshold, and negative values indicate a reduced cavity length from this position. It can be seen that the time-bandwidth product does not change significantly with cavity length, again showing that with confidence the cavity length can be varied, and still ensure that the signal spectral shape and chirp are not drastically affected. It can be further noted that increasing the cavity length results in more signal spectral bandwidth being generated, with an associated shorter signal pulse.

It was not possible to increase the cavity length beyond $20\,\mu m$ since the signal power dropped below that required for stable operation of the OPO. However the effects of increasing the cavity length are well known and result in signal pulse-compression [5], this phenomenon is not restricted to PPLN, and has been observed in OPOs with different nonlinear materials [6]. Pulse-compression is

most pronounced for the case where group-velocity mismatch between the pump and signal are greatest. From figure 2.3 it is clear that our experiment could be effected by this phenomenon. Pulse-compression is not desirable for pulse transfer as it results in a larger spectral bandwidth for the signal, and this reduces the fidelity of the transfer process. Furthermore, operating the OPO at many times threshold, coupled with pulse-compression can result in the signal pulse breaking up into multiple pulses (fortunately the power entering the OPO is insufficient to cause this effect). Because of these negative qualities, care is taken to avoid pulse-compression. The easiest method to avoid pulse compression is to avoid increasing the cavity length from the position of minimal threshold, but in some situations this may not be desirable. Lefort et. al. show that pulse-compression is best observed when using highly transmissive output couplers and for the OPO operating between 2.5 and 3 times threshold [5]. In order to reduce this effect attempts are made to use highly reflective output couplers and operating the OPO at about four times threshold. Finally, the use of spectrally narrowing optics such as etalons and birefringent filters can be used to eliminate pulse-compression.

Figure 6.2 shows that the signal is reasonably unaffected by changes in the cavity length. However, the effects of cavity detuning are noticed on the idler autocorrelation. Figure 6.3 shows the idler IAC for three cavity lengths. The three traces were chosen at the extreme ends of the cavity detuning so as to show the extreme cases. It can be seen that even small changes in the cavity length can have large effects on the idler interferometric autocorrelation. It is even possible to produce a chirp-free idler pulse via cavity tuning.

The conclusions drawn from these tests is that for a central wavelength of $1510\,nm$ the signal pulse remains close to time-bandwidth limited for changes of the cavity length in the range of tens of microns and for changes in the threshold of the OPO of a few times threshold. This is despite the pump pulse having a time-bandwidth product of approximately 4.5. Furthermore the signal spectrum remains Gaussian-like for the duration of the testing. These conditions indicate that the signal pulse does not drastically affect the pulse transfer from the pump to the idler.

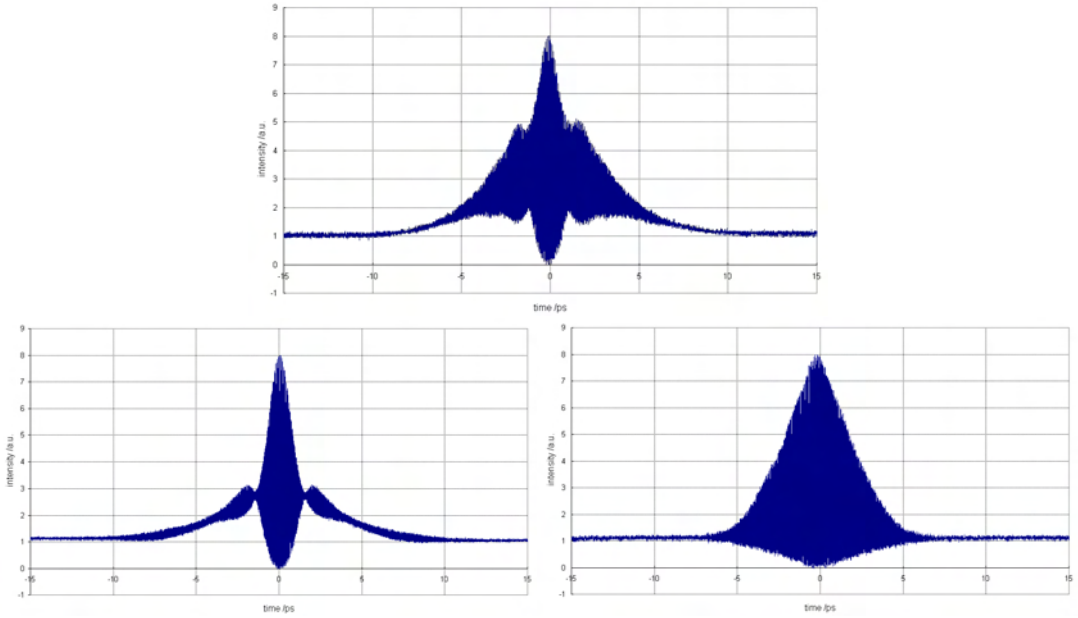

FIGURE 6.3: idler pulse shape with cavity length, OPO operating 3.8 times minimum threshold and with a 65% reflective O/C. The top picture shows the idler interferometric autocorrelation for the case of the OPO cavity being adjusted for minimum threshold (i.e. the case of "zero microns" as shown in the previous figures). The bottom left figure represents a $20\mu m$ cavity length adjustment and the bottom right figure shows a $290\mu m$ decrease in the cavity length.

6.2 Spectral Narrowing

With the preliminary experiments performed, the spectral bandwidth of the signal pulse was restricted. There are several possibilities for controlling the signal bandwidth. These include gratings [7], birefringent filters [8] and etalons [9]. The latter has been used for their simplicity in these experiments.

The etalon was used inside a standing-wave SPOPO and therefore the signal made two passes through the etalon per round trip. The reflectivity of the etalon is dependent on the polarisation of light and the axis of rotation [10]. The polarisation of the signal beam produced by the OPO was perpendicular to the optics bench and the etalon was rotated about the plane perpendicular to the optics bench. In most situations the etalon was used with the incoming beam close to perpendicular to the surface of the etalon.

With a near bandwidth-limited pump pulse the signal spectral bandwidth was found to be $3\,nm$ with the OPO operating at 2.2 times threshold. Figure 6.4 shows the spectral profile of the spectrum when a $\sim 1\,mm$ thick uncoated glass

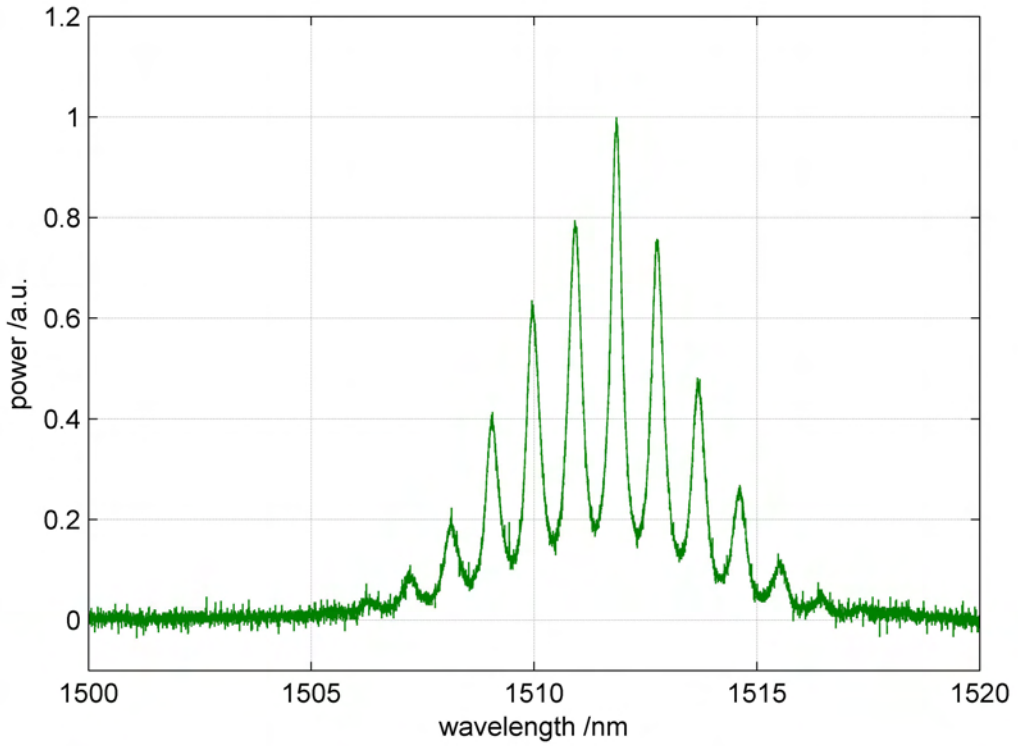

FIGURE 6.4: Signal spectrum with a 1mm uncoated glass etalon within the SPOPO. The spectral bandwidth without the etalon is 3.1nm (and operating 2.2 times threshold), this is approximately the same value when measuring across the central 5 peaks.

etalon was inserted inside this OPO. The OPO was again operated at about 2.2 times threshold with the etalon. The spectral bandwidth of the individual peaks was $0.3\,nm$, and the observed free spectral range of the etalon was $0.9\,nm$, which is in good agreement with theory. This small demonstration shows that for small pump depletion an uncoated glass etalon is capable of significantly restricting the signal bandwidth. By itself this particular etalon is not suitable for pulse transfer since its free-spectral range is too small, but it demonstrates the principle.

It can also be noted that the transmission of the etalon with wavelength is not a top-hat function; it resembles a sinusoidal profile. Hence, if significant losses for the spectral bandwidth are not required, then the spectral bandwidth for the filter must be increased. Further experiments with $150\,\mu m$ and $570\,\mu m$ glass etalons were used, these etalons have nominal spectral bandwidths of $2.5\,nm$ and $0.59\,nm$ respectively.

6.3 Spectral Transfer

The experiment consisted of inserting a $150\,\mu m$ glass etalon inside the OPO and using a 95% reflective O/C to extract some of the signal light for measurement purposes. The threshold for each cavity length was determined and the OPO operated three times this value. At this level of operation the idler and signal spectra were recorded. It was found that the best pulse transfer occurs when the cavity length of the OPO was decreased by $20\,\mu m$ from the minimum threshold value. Figure 6.5 shows the idler spectral profile corresponding to our best case spectral transfer, as recorded on the monochromator, and the pump bandwidth was measured using an OSA (Ando AQ-6310C).

The decrease in cavity detuning required for good transfer can be explained if we first understand why the lowest threshold occurs for a given cavity length. This is most likely due to achieving good a temporal overlap between the signal and pump. The signal has a higher group-velocity than the pump, so for a good overlap, and low threshold, the signal pulse must enter the OPO crystal after the pump pulse. Then the signal "walks through" the pump pulse and interacts with it. However, the crystal has a finite length; therefore in order to minimise threshold the most intense part of the signal pulse should interact with the most intense part of the pump pulse. For most pulses the highest peak power is located at the centre of the pulse. Hence, the signal pulse should be delayed by half the length of the crystal times the group velocity mismatch between the pump and signal ($\delta\nu_{ps}L/2$). Fortunately, in order to achieve high fidelity transfer in a single-pass DFG process for the case of negligible $\delta\nu_{pi}$ and no pump-depletion, the signal pulse should be delayed relative to the pump by this exact amount [1]. This value corresponds to $0.5\,ps$ in the time domain and about $150\,\mu m$ spatially. In the experiments $\delta\nu_{pi}$ was very close to zero, therefore it is unsurprising that the cavity length required to achieve good fidelity in the experiments is so similar to the minimal threshold length. It is important to stress that this is only the case for $\delta\nu_{pi} \backsimeq 0$. Prawiharjo shows that the effects of pump depletion, and arbitrary group-velocity mismatch between the various pulses results in no analytical expression to predict the required cavity detuning.

Using a more restrictive etalon inside the OPO should result in better pulse transfer in terms of resolution. To demonstrate this a $570\,\mu m$ uncoated glass etalon was used. Figure 6.6 shows the spectrum of the idler for varying cavity length, as well

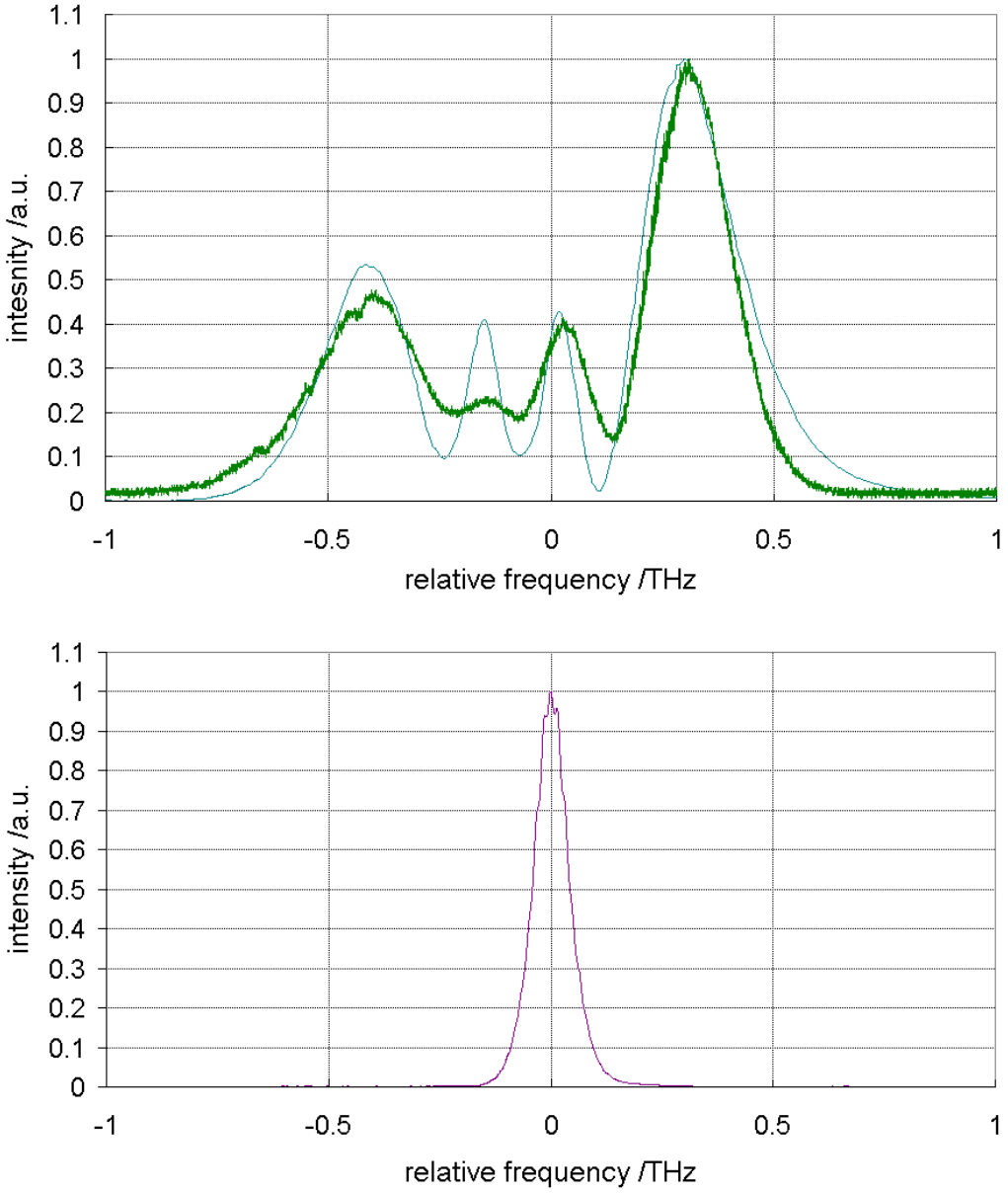

FIGURE 6.5: Both figures correspond to the same experiments in which a 150 μm etalon was placed inside the SPOPO and the cavity length changed. The pump entering the OPO was unmodified by the SLM. The top figure shows the idler spectrum (green) and pump spectra (blue). Bottom figure corresponds to the signal spectrum inside the SPOPO.

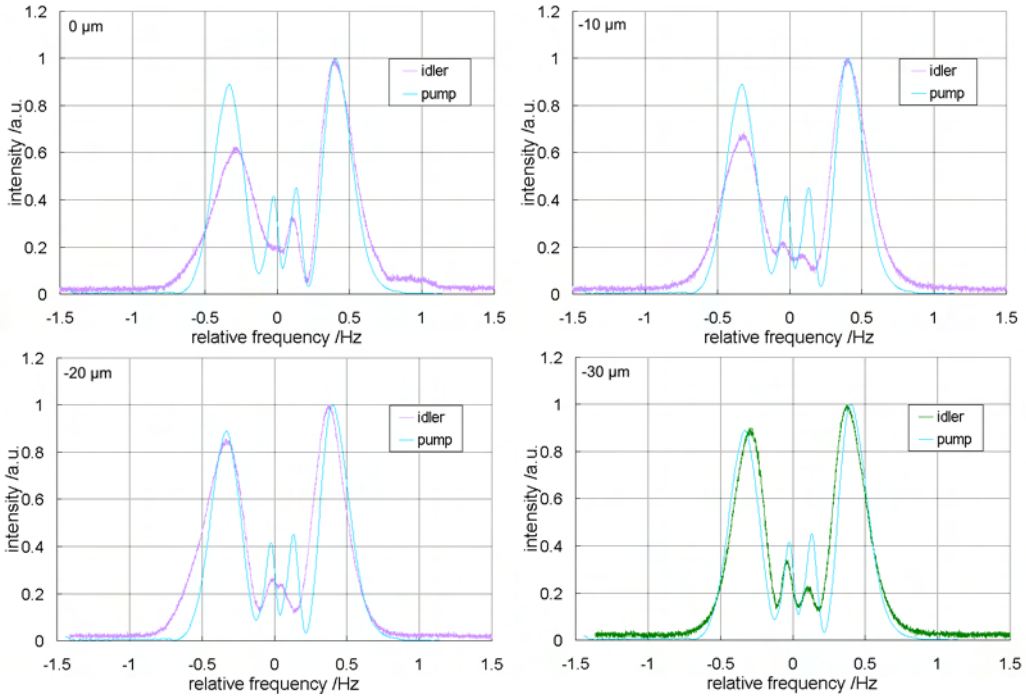

FIGURE 6.6: Graphs showing idler spectra with variation of cavity length. For comparison the pump spectrum has been included. The number in the top left-hand corner of each graph corresponds to the cavity length detuning of the OPO. The optimal transfer occurred with a -30μm detuning of the OPO cavity. The graphs have been independently normalised.

as the best transfer, which occurred at $-30\,\mu m$ detuning away from the cavity length that achieved minimum threshold. The more restrictive etalon results in a higher operating threshold for the OPO, as a result it was not possible to achieve stable signal spectra for a cavity length detuning greater than $-30\ \mu m$. It can be seen that the more restrictive etalon result in a better pulse transfer fidelity. It can be noted from figure 6.6 that a change in cavity length results in different parts of the idler spectrum being amplified. This can be attributed to group-velocity mismatch between the pump and signal that causes the signal pulse to walk-through the pump pulse. The pump pulse entering the OPO is linearly chirped due to SPM from the fibre. Therefore, the spectral frequencies within the pump pulse are not uniformly spaced in time. For a positively chirped pulse, such as ours, the longer frequency components are more dominant at the front than the back. Therefore by changing the cavity length it is possible to overlap different frequency components within the pulse. More specifically with shorter cavity lengths the longer frequency components see a better temporal overlap, and therefore experience more gain. This can be readily seen in figure 6.6.

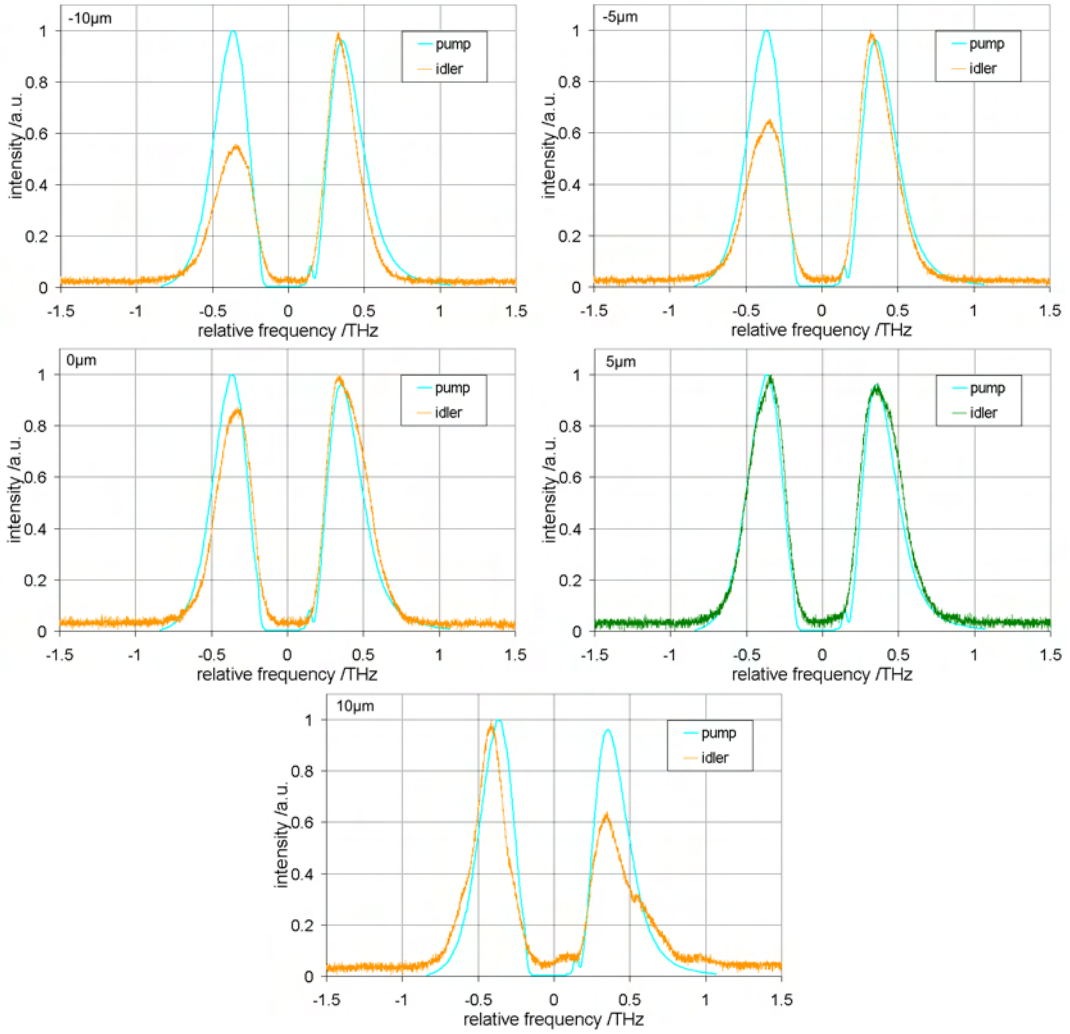

FIGURE 6.7: Graph showing amplitude transfer of the pump spectrum to the idler with variations in cavity length. In the top left hand corner of each graph is the cavity length detuning away from minimum threshold.

6.4 Pump Cut-out Transfer

The theory presented at the beginning of this chapter does not place any limitations on the shape of the pump spectrum that can be transferred over to the idler. So far the only transfers from the pump to idler have been SPM generated spectra. It would be interesting to see if other pump spectra could be equally transferred to the idler but unfortunately the SLM available is not capable ofamplitude modulation. However amplitude modulation can be crudely demonstrated by blocking out the central part of the pump spectrum by placing an object at the Fourier plane of the pulse-shaper. Figure 6.7 shows experimental results of amplitude modulation, the setup used is the same as the setup for the 150 μm

etalon experiments previous described. It can be seen that changing the cavity length has the same effect seen with the SPM spectrum, namely it can compensate for a non-zero $\delta\nu_{ps}$ and improve the spectral transfer from the pump to idler. The cavity length needed to achieve good spectral transfer is slightly different from that seen in section 6.3. This is most likely because the chirp on the pulse has changed due to blocking out part of the spectrum. As a result, a slightly different cavity length is required.

The amplitude modulation experiment conducted in this section is limited in its scope, but it agrees with our statement on pulse transfer being possible for other shapes.

6.5 Group Velocity Mismatch

For this final experiment the effects of group velocity mismatch between the pump and idler, $\delta\nu_{pi}$ are shown. This is achieved by changing the carrier wavelength of the idler pulse. Prawiharjo [1] shows that a GVM between the pump and idler can reduce the pulse transfer fidelity, and for arbitrary GVM between the various pulses there is no simple analytical expression that can be used to deduce the effect on the idler, and numerical methods must be employed.

This effect was experimentally verified by changing the carrier wavelength of the signal pulse to $1702\,nm$ by using a different crystal poling period. The OPO was operated using a 95% reflective O/C at a pump power of about three times threshold. Figure 6.8 shows the signal spectrum for this experiment for no detuning of the OPO cavity from minimal threshold. The spectral bandwidth of the signal is $12.5\,nm$. For comparison when the signal wavelength was $1510\,nm$ the signal spectral width was typically about 1nm (see figure 6.2 and 6.1). Furthermore, it is clear that the signal spectrum is no longer Gaussian, but resembles the pump spectrum.

An explanation for these effects can be explained by considering the effects of small changes in the pump frequency on the k-vector mismatch. This analysis begins with the equations that describe energy and momentum conservation of

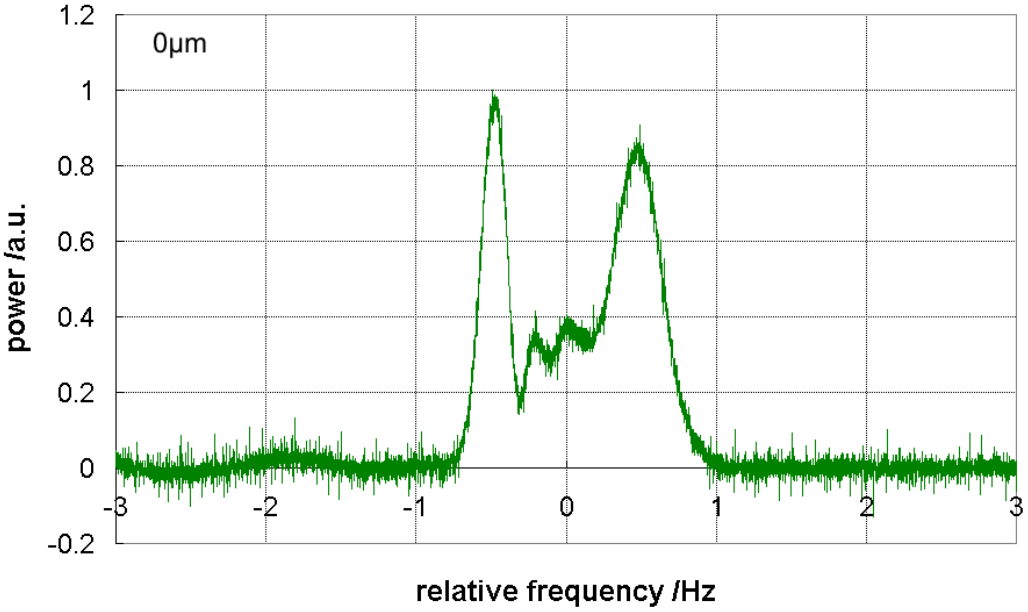

FIGURE 6.8: Signal spectrum for a central wavelength of 1702nm and the cavity length of the OPO at minimum threshold. Data recorded from OSA (Ando AQ-6310C)

the various pulses (as seen in section 2.2):

$$\omega_p = \omega_s + \omega_i \tag{6.5}$$

$$k_p = k_s + k_i + k_G \tag{6.6}$$

Where k_G is the wavevector corresponding to the grating period. A small perturbation in the angular frequency of the pump $\delta\omega_p$ requires a small change in the idler $\delta\omega_i$ and signal $\delta\omega_s$ frequencies. Such that $\omega_{p,s,i} \rightarrow \omega_{p,s,i} + \delta\omega_{p,s,i}$, where for brevity the subscript p, s, i refer to either the pump, signal, and idler respectively. Therefore equation 6.5 can be written as:

$$\delta\omega_p = \delta\omega_s + \delta\omega_i \tag{6.7}$$

By turning our attention to the wavevector, it can be noted that the wavevector can be expanded using a Taylor series. For small changes to the carrier frequency, only the first two terms in the expansion need be considered:

$$k_{p,s,i} \rightarrow k_{p,s,i} + \frac{1}{u_{p,s,i}}\delta\omega_{p,s,i} \tag{6.8}$$

Where the variable $u_{p,s,i}$ corresponds to the group velocity for either the pump,

signal, or idler. By substituting equation 6.8 into the definition of the k-vector mismatch given by equation 6.6 and using 6.7 the following equation is derived:

$$\frac{\delta\omega_s}{\delta\omega_p} = \left(\frac{u_i - u_p}{u_i - u_s}\right)\left(\frac{u_s}{u_p}\right) \tag{6.9}$$

An equivalent relationship can be derived to relate small changes in the pump frequency to the idler frequency. However, the analysis is very similar and so only the above equation is discussed. The equation shows that the group velocity of the various beams can affect the spectral bandwidth of the signal. It can be see that in the limiting case of $u_s \rightarrow u_p$, $\delta\omega_s = \delta\omega_p$. Physically this would correspond to the case of the pump spectrum being transferred over to the signal. Figure 6.8 shows this effect. Furthermore it can be noted that in the limiting condition of $u_i \rightarrow u_p$ equation 6.9 shows that $\delta\omega_s \rightarrow 0$. This was seen for experiments conducted for the signal wavelength at $1.5\,\mu m$. In those experiments that signal bandwidth was observed to be $\sim 1\,nm$. By comparison if the spectral bandwidth of the pump was transferred over to the signal then this would corresponded to a signal bandwidth of $7.3\,nm$. The self-narrowing of the signal spectrum is highly desirable since it results in no increase in the OPO threshold and can result in a better pulse transfer between the pump and idler. It can also be noted that the shaping of the signal pulse can not be explained by Imeshev's theory since this theory strictly corresponds to the case of a single-shot DFG interaction between a pump and signal pulse, whereas within an OPO the signal pulse is generated via parametric noise. This signal pulse adapts itself to meet the conditions the OPO is operated with.

It is of course possible to restrict the signal pulse for the case of $\delta\nu_{pi} \neq 0$, these experiments were conducted using a three plate birefringent filter with the plate thickness ratio of 1:2:15, and the thickest plate having a width of $9\,mm$. The birefringent filter had a calculated spectral bandwidth of approximately $1\,nm$. By using this filter it was possible to restrict the signal spectrum to 1nm. However, the resulting increase in threshold made it impractical to retrieve a spectrum of the idler.

6.6 Conclusion and Discussion

This chapter has demonstrated that pulse transfer from the pump spectrum to the idler can be achieved using an OPO and an intra-cavity etalon. It was found experimentally that this process is most efficient when the group velocity mismatch between the pump and idler is negligible and that cavity detuning is required to achieve optimal transfer. It has been shown that etalons with more restrictive bandwidths result in better transfer fidelity. Our results are in excellent agreement with numerical and theoretical studies conducted by Prawiharjo et. al.

One effect not mentioned so far is pump depletion. Experimentally pump depletion was measured to be between 50 and 70%. This is non-negligible and will alter equation 6.1 since in deriving this equation it was assumed that pump depletion can be neglected.

Infact the numerical work of Prawiharjo et. al. [1] show that high pump depletion improves transfer fidelity up to the point where back conversion becomes significant. Equation 6.1 also assumes negligible signal amplification and Prawiharjo et. al. [1] show that strong amplification does harm the transfer. However, as this research is only interested in the idler pulse, signal amplification could be minimised in future by using a low loss cavity with no signal output coupling.

6.7 References

[1] J. Prawiharjo, H. S. S. Hung, D. C. Hanna, and D. P. Shepherd, "Theoretical and numerical investigations of parametric transfer via difference-frequency generation for indirect mid-infrared pulse shaping," J. Opt. Soc. Am. B: Opt. Phys. **24**(4), 895–905 (2007).

[2] G. Imeshev, M. A. Arbore, M. M. Fejer, A. Galvanauskas, M. Fermann, and D. Harter, "Ultrashort-pulse second-harmonic generation with longitudinally nonuniform quasi-phase-matching gratings: pulse compression and shaping," J. Opt. Soc. Am. B: Opt. Phys. **17**(2), 304–318 (2000).

[3] A. M. Schober, M. Charbonneau-Lefort, and M. M. Fejer, "Broadband quasi-phase-matched second-harmonic generation of ultrashort optical pulses with spectral angular dispersion," Journal of the Optical Society of America B-Optical Physics **22**(8), 1699–1713 (2005).

[4] M. F. Becker, D. J. Kuizenga, D. W. Phillion, and A. E. Siegman, "Analytic Expressions for Ultrashort Pulse Generation in Mode-Locked Optical Parametric Oscillators," J. Appl. Phys. **45**(9), 3996–4005 (1974).

[5] L. Lefort, K. Puech, S. D. Butterworth, Y. P. Svirko, and D. C. Hanna, "Generation of femtosecond pulses from order-of-magnitude pulse compression in a synchronously pumped optical parametric oscillator based on periodically poled lithium niobate," Opt. Lett. **24**(1), 28–30 (1999).

[6] R. S. Kurti and K. D. Singer, "Pulse compression in a silver gallium sulfide, midinfrared, synchronously pumped optical parametric oscillator," J. Opt. Soc. Am. B: Opt. Phys. **22**(10), 2157–2163 (2005).

[7] M. A. Watson, M. V. O'Connor, P. S. Lloyd, D. P. Shepherd, D. C. Hanna, C. B. E. Gawith, L. Ming, P. G. R. Smith, and O. Balachninaite, "Extended operation of synchronously pumped optical parametric oscillators to longer idler wavelengths," Opt. Lett. **27**(23), 2106–2108 (2002).

[8] M. V. O'Connor, M. A. Watson, D. P. Shepherd, and D. C. Hanna, "Use of a birefringent filter for tuning a synchronously pumped optical parametric oscillator," Appl. Phys. B **79**(1), 15–23 (2004).

[9] P. G. Harper, B. S. Wherrett, and N. A. S. Institute, *Nonlinear optics: proceedings of the Sixteenth Scottish Universities Summer School in Physics, 1975* (Academic Press, London; New York, 1977).

[10] E. Hecht, *Optics*, 4th ed. (Addison-Wesley, San Francisco, 2002).

Chapter 7

Conclusion and Discussion

The results demonstrate the feasibility of achieving good fidelity of spectral transfer from the near to mid-infrared by using an SPOPO. The ability to control mid-infrared pulses using an adaptive feedback loop and a simulated annealing search algorithm has also been demonstrated. The work lays down the foundations for more detailed experiments to be conducted. No immediate issues with using the method to achieve arbitrary mid-IR pulses are envisaged. The work here, to the best of our knowledge demonstrates the first use of an OPO to achieve these results.

The power available in our current setup is limited by the damage threshold of the SLM. This meant that the OPO could only be operated a few times threshold, and this restricted the scope of experiments that can be conducted in the mid-IR. There are two ways to overcome this limitation. Firstly, one can incorporate a laser amplifier soon after the shaper and before the OPO. Or alternatively, the current laser source used can be replaced with an ultra broadband source capable of producing pulse widths in the tens of femtosecond regime. With such a laser source the average power incident on the SLM can remain approximately the same, but the threshold of the OPO is significantly reduced. The use of broader bandwidth pulses is also advantageous to the resolution requirements for the pulse-shaper. Since it means that for an SLM with the same number of pixels, each pixel modulates a larger spectral bandwidth and this reduces the resolution tolerance for the whole setup. Femtosecond SPOPOs have been previously been demonstrated [1]. The use of a more powerful source will make it possible to restrict the signal

spectrum for the case of $\delta\nu_{pi} \neq 0$ and still be able to achieve enough power to produce intense idler pulses.

Our experiments show good agreement with the numerical and analytical studies performed by Prawiharjo et. al. Future research can involve investigations of the effects of pulse-front tilt on the pump pulse on the OPO. The diagnostic instruments available to us at the time are not sensitive to pulse-front tilt, and therefore it can not be experimentally verified if this was transferred over from the pump to the idler. However, it is clear from our results that pulse-front tilt does not appear to have an effect on the spectral transfer process.

Furthermore, the effects of large pump depletion have not affected the spectral transfer process. Therefore allowing the use of an OPO to achieve intense idler pulses, which can be used for coherent control.

It is natural to compare our technique with existing methods. For comparison Tan et. al. [2, 3] have used a pulse shaper with an AOM as the modulating element and an OPA in order to achieve mid-IR pulse transfer using an OPA. Their laser source produced pump pulses with $0.5mJ$ of energy, and the shaped idler pulses produced had energies of 1-2μJ. In comparison, with our system it is estimated that about 11% of the laser power out of the fibre is converted over to the idler pulses, which is approximately a 100 times improvement in energy transfer from the OPA. OPAs have many advantages in pulse-shaping, however this research has demonstrated that OPOs can also be used to produce similar results.

Our system shows that it is possible to achieve control of mid-IR pulses using modest components. It is hoped that this research will allow other to follow suit and could help further interest in mid-IR control.

In conclusion, this research has demonstrated the feasibility of an OPO to be a good basis for research into producing an adaptively controllable AWG in the mid-IR.

7.1 References

[1] M. V. O'Connor, M. A. Watson, D. P. Shepherd, D. C. Hanna, J. H. V. Price, A. Malinowski, J. Nilsson, N. G. R. Broderick, and D. J. Richardson, "Synchronously pumped optical parametric oscillator driven by a femtosecond mode-locked fiber laser," Opt. Lett. **27**(12), 1052–1054 (2002).

[2] H. S. Tan, E. Schreiber, and W. S. Warren, "High-resolution indirect pulse shaping by parametric transfer," Opt. Lett. **27**(6), 439–441 (2002).

[3] H. S. Tan and W. S. Warren, "Mid infrared pulse shaping by optical parametric amplification and its application to optical free induction decay measurement," Opt. Express **11**(9), 1021–1028 (2003).

Chapter 8

List of Publications and Conferences

- H. S. S. Hung, N. A. Naz, J. Prawiharjo, D. C. Hanna, and D. P. Shepherd, Parametric transfer in a synchronously pumped optical parametric oscillator, published at CLEO/QELS 2006.
- N. A. Naz, H. S. S. Hung, M. V. O'Connor, D. P. Shepherd, and D. C. Hanna, Adaptively shaped mid-infrared pulses from a synchronously pumped optical para- metric oscillator, Optics Express 13(21), p. 8400, 2005.
- N. A. Naz, H. S. S. Hung, M. V. O'Connor, D. P. Shepherd, and D. C. Hanna, An intelligent, synchronously pumped optical parametric oscillator using adaptive pulse-shaping techniques, in CLEO, paper CThQ6, 2005.